



**HAL**  
open science

## Using zircons to disentangle back-veining and hybridization of diorite dykes : an example from the Gangdese Arc, Tibet

Roberto Weinberg, Jean-François Moyen, Jian-Kang Yi, Di-Cheng Zhu, Oliver Nebel, Shaorong Chen, Qiang Wang

### ► To cite this version:

Roberto Weinberg, Jean-François Moyen, Jian-Kang Yi, Di-Cheng Zhu, Oliver Nebel, et al.. Using zircons to disentangle back-veining and hybridization of diorite dykes : an example from the Gangdese Arc, Tibet. *Journal of Petrology*, 2023, pp.egad010. 10.1093/petrology/egad010 . hal-03986303

**HAL Id: hal-03986303**

**<https://uca.hal.science/hal-03986303>**

Submitted on 13 Feb 2023

**HAL** is a multi-disciplinary open access archive for the deposit and dissemination of scientific research documents, whether they are published or not. The documents may come from teaching and research institutions in France or abroad, or from public or private research centers.

L'archive ouverte pluridisciplinaire **HAL**, est destinée au dépôt et à la diffusion de documents scientifiques de niveau recherche, publiés ou non, émanant des établissements d'enseignement et de recherche français ou étrangers, des laboratoires publics ou privés.



Draft Manuscript for Review

### Using zircons to disentangle back-veining and hybridization of diorite dykes: an example from the Gangdese Arc, Tibet

Journal:	<i>Journal of Petrology</i>
Manuscript ID	JPET-Jan-22-0002.R2
Manuscript Type:	Original Manuscript
Date Submitted by the Author:	n/a
Complete List of Authors:	Weinberg, Roberto; Monash University, School of Earth, Atmosphere and Environment Moyen, Jean-Francois; Laboratoire Magmas et Volcans; OPGC, CNRS, Université Jean Monnet, Yi, Jian-Kang; China University of Geosciences, Beijing Zhu, Dicheng; China University of Geosciences, Beijing, Nebel, Oliver; Monash University, School of Earth, Atmosphere and Environment Chen, Shaorong; China University of Geosciences, Beijing Wang, Qing; China University of Geosciences Beijing, ;
Keyword:	zircon, zircon saturation temperature, magma hybridization, magma mingling, geothermometry
Journal of Petrology now offers Virtual Collections of published papers. You may choose up to three collections from the list below. Virtual collections will increase the visibility of your work.:	Continental Collision Zones < Province Themes, Continental Crustal Genesis and Evolution < Process Themes, Partial Melting < Process Themes

SCHOLARONE™  
Manuscripts

1 **Using zircons to disentangle back-veining and hybridization of**  
2 **diorite dykes : an example from the Gangdese Arc, Tibet**

3 Roberto F. Weinberg<sup>1\*</sup>, Jean-François Moyen<sup>2</sup>, Jian-Kang Yi<sup>3</sup>, Di-Cheng Zhu<sup>3</sup>,  
4 Oliver Nebel<sup>1</sup>, Shaorong Chen<sup>3</sup>, Qiang Wang<sup>3</sup>

5 <sup>1</sup>School of Earth, Atmosphere and Environment, Monash University, Clayton, VIC, 3800,  
6 Australia.

7 <sup>2</sup> Université de Lyon, Laboratoire Magmas et Volcans, UJM-UCA-CNRS-IRD,  
8 23 rue Dr. Paul Michelon, 42023 Saint Etienne, France

9 <sup>3</sup> State Key Laboratory of Geological Processes and Mineral Resources, China University of  
10 Geosciences, Beijing 100083, China

11 \*Corresponding author Telephone: +61 3 9905 4902. Fax: +61 3 9905 4903. E-mail:  
12 Roberto.weinberg@monash.edu

13

14

15 **ABSTRACT**

16 Thermo-chemical modelling and chemical data suggest that the genesis of arc melts commonly  
17 involves re-melting of older intrusions, triggered by the injection of mantle-derived melts,  
18 followed by magma mixing. Remelting and mixing may lead to complex zircon populations,  
19 which can be used to gain insights into the conditions of mixing. This paper investigates a case  
20 where such processes can be studied through the compositional and thermal record provided by  
21 zircons preserved in a diorite dyke swarm that remelted host rock tonalites in the Gangdese  
22 Batholith in Tibet. Autocrystic zircons from the diorite yield consistent ages of 46-47 Ma even  
23 though they can be altered, having highly enriched trace elements, reaching ~1 wt% in Fe, Ca,  
24 Y, U, Th, and anomalously high values of LREE and Ti. Granitic magmas derived from the  
25 tonalite, back-veined the dykes and mixed with the dioritic mush, transferring small quantities of  
26 77-79 Ma zircon xenocrysts. The xenocrysts are euhedral with little evidence for resorption,  
27 indicating they were apparently stable during the process of tonalite anatexis and transfer to the  
28 diorite magma. This requires that: (i) tonalite melting occurred at low temperatures with  
29 minimal zircon dissolution, and (ii) the diorite either cooled rapidly before significant resorption  
30 of the grains or was already saturated in zircon when mixing occurred. Zircon saturation  
31 temperatures of the diorite are relatively low, indicating that xenocrystic zircons were  
32 transferred to a highly crystalline dioritic mush. This requires either liquefaction by injection of  
33 the back-veining felsic magma to allow for mixing or pervasive throughflow of the diorite mush  
34 by the felsic magma leaving behind zircon xenocrysts. The findings suggest that the dykes  
35 triggered low-T, water-fluxed melting of the host tonalite, and that these anatectic melts invaded  
36 the diorite mush initially through the interstices leading to mixing and this may have caused the  
37 breakdown of the crystalline framework leading to liquefaction and renewed magma flow.  
38 Dyking and assimilation of wall-rock through back-veining as recorded in these rocks could be  
39 common in transcrustal arcs. However, this process could be hidden due to a combination of the



40 similarity in the isotopic and chemical nature of arc rocks, and resorption of zircon xenocrysts  
41 during mixing. This process may explain some complex chemistry of arc magmatic rocks and  
42 their minerals that are not easily explained by endmember models, such as pure re-melting of  
43 older arc rocks or fractional crystallization of mantle-derived melts.

44 **Key words:** geothermometry; magma hybridization; magma mingling; zircon; zircon saturation  
45 temperature

## 46 INTRODUCTION

47 The origin of granitic magmas in arcs is at the center of a long-standing debate focused on  
48 whether they are derived from the fractionation of basaltic magmas (Jagoutz & Klein, 2018,  
49 Müntener & Ulmer, 2018), or the remelting of older arc intrusions (Collins *et al.*, 2020, Moyer  
50 *et al.*, 2021, Symington *et al.*, 2014, Weinberg & Dunlap, 2000b) or magma mixing (Reubi &  
51 Blundy, 2009). In this regard, evidence for zircon recycling through the system as xenocrysts  
52 and antecrysts, combined with Ti-in-zircon thermometry and zircon saturation temperatures, can  
53 be used to explore and constrain the processes controlling arc magma evolution, such as whether  
54 mixing or assimilation processes were involved and when and how they occurred. The term  
55 xenocryst refers here to zircon incorporated from the surrounding host rocks during magma  
56 transit and emplacement, whereas the term antecrysts refers to zircon formed in an earlier pulse  
57 of magma and that was transferred to the current host. The term autocryst refers to zircon  
58 crystallized from the host magma (Miller *et al.*, 2007).

59 Zircon has a number of properties that makes it useful in constraining magmatic processes. It is  
60 an excellent marker of the time of magma crystallization, and its trace elements indicate  
61 contemporaneous crystallization or dissolution of other minerals (Rubatto & Hermann, 2007).  
62 Its Hf isotopic composition is a sensitive indicator of melt sources and mixing between magmas  
63 from different sources (Kemp *et al.*, 2007), and in the case of xenocrystic zircon, Hf isotopic

64 ratio can be used to determine its source. Further to that, Ti-in-zircon thermometry (Watson *et*  
65 *al.*, 2006), in combination with zircon saturation temperatures of magma (Boehnke *et al.*, 2013,  
66 Watson & Harrison, 1983), constrain magma crystallization histories (Schiller & Finger, 2019)  
67 and the conditions prevalent during fractionation and mixing (Barnes *et al.*, 2019, Harrison *et*  
68 *al.*, 2007, Miller *et al.*, 2003, Miller *et al.*, 2007, Siégel *et al.*, 2018). These data can then be  
69 linked to modeling of the chemical evolution of melt and crystals during crystallization to define  
70 zircon saturation temperature and the expected Ti-content of zircons (Barnes *et al.*, 2019, Lee &  
71 Bachmann, 2014).

72 There is often a mismatch between temperatures derived from Ti-in-zircon and from zircon  
73 saturation. In samples with many zircon xenocrysts, this mismatch can be caused by the added  
74 Zr. In samples with few or no xenocrysts, the mismatch can be caused either by fractional  
75 crystallization that changes the Zr content and composition of the interstitial melt, or by changes  
76 in the total Zr content through accumulation of zircons and other minerals, or through loss of Zr-  
77 rich interstitial melt (Barnes *et al.*, 2019). Zircon saturation temperatures unaccompanied by  
78 modeling of fractional crystallization have been used to suggest that arc granites typically record  
79 relatively low zircon saturation temperatures, and to postulate that granitic arc magmas are  
80 typically cold (<800 °C), derived from water-fluxed re-melting of older arc rocks (Collins *et al.*,  
81 2016, Collins *et al.*, 2020). However, zircon saturation temperature is strongly dependent on the  
82 initial Zr content of the magma and the evolution of the residual melt composition during  
83 crystallization (Miller *et al.*, 2003).

84 In this paper, we explore the nature of zircon autocrysts in diorite dykes and the fate of zircon  
85 xenocrysts transferred from the host rock as a result of anatexis of the host rock, back-veining  
86 and mixing, in an outcrop in the Gangdese Batholith in Tibet (Zhu *et al.*, 2015). We use zircon  
87 U-Pb ages and grain morphology, combined with zircon saturation temperatures and Ti-in-  
88 zircon thermometry to constrain the thermal conditions and magma crystallinity during mixing.

89 The discussion is underpinned by compositional modelling of a crystallizing melt and the trace  
90 element composition of zircons in the evolving melt.

91 The paper starts with a brief description of the Gangdese Batholith and field relationships  
92 between the diorite dykes and host rocks investigated here, including the back-veining and  
93 hybridization of the dykes caused by melting of the host. The methodology is then described,  
94 followed by characterization of the tonalite and diorite samples and their zircons, including U-  
95 Pb dating, Hf-isotope and trace element composition. Whole-rock chemistry is used as the basis  
96 for modeling diorite magma crystallization and determining zircon saturation temperatures, as  
97 well as to model tonalite melting occurring as the diorite cooled. Modelled zircon saturation  
98 temperatures and zircon trace element compositions are also derived from these models and  
99 form the basis for discussion of the timing of magma mixing and xenocryst transfer, and the  
100 validity of Ti-in-zircon thermometry for these zircons. Results show how these approaches  
101 combined can be used to cast light on both the physical details of hybridization, and to  
102 exemplify some of the pitfalls associated with interpreting the data.

## 103 **GANGDESE BATHOLITH AND DABU GEOLOGY**

104 The Gangdese Batholith (Fig. 1) and its western continuation in NW India and Pakistan, the  
105 Ladakh and Kohistan Batholiths, is a 2500 km-long calc-alkaline magmatic arc that extends  
106 across the southern Tibetan Plateau. It is an Andean-type continental arc formed as a result of  
107 oceanic subduction of the Neo-Tethys oceanic lithosphere under the Lhasa Terrane at the Asian  
108 continental margin until collision with India at  $55 \pm 5$  Ma shut down the arc (Ji *et al.*, 2009, Yin  
109 & Harrison, 2000, Zhu *et al.*, 2019). Magmatism started at  $\sim 210$  Ma and continued  
110 intermittently until collision ended typical subduction-related magmatism and initiated post-  
111 collisional magmatism. Subduction-related magmatism is marked by two intense pulses of  
112 magmatic activity, one at  $90 \pm 5$  Ma and the other at 55-50 Ma (Zhu *et al.*, 2019). The  $90 \pm 5$

113 Ma event is linked with ridge subduction (Zhang *et al.*, 2010) or slab rollback (Ma *et al.*, 2013)  
114 of the Neo-Tethyan oceanic lithosphere, whereas the 55-50 Ma event is attributed to collision  
115 followed by slab breakoff (Zhu *et al.*, 2019) or lithosphere removal (Kapp & DeCelles, 2019).  
116 The dykes investigated here belong to the syn-collisional event, which was the most intensive  
117 magmatic pulse in the Gangdese belt (Zhu *et al.*, 2019), and includes the voluminous Linzizong  
118 volcanic successions (Zhu *et al.*, 2015). Oligocene-Miocene post-collisional magmatism was  
119 dominated by silicic rocks resulting from the remelting of arc magmatic rocks and their  
120 hybridization with metasomatized lithospheric mantle-derived ultrapotassic melts (e.g. Wang *et*  
121 *al.*, 2018).

122 Magmatic rocks from the  $90 \pm 5$  Ma events show coherent “depleted mantle-like” zircon  $\epsilon_{\text{Hf}}(t)$   
123 (+15 to +10) and positive whole-rock  $\epsilon_{\text{Nd}}(t)$  (around +3.0) with a few outliers (Ji *et al.*, 2009,  
124 Ma *et al.*, 2013, Zhang *et al.*, 2020, Zhu *et al.*, 2011) that may reflect varying degrees of  
125 incorporation of ancient crustal components from the Gangdese basement into the juvenile  
126 magmas. Rocks related to the  $55 \pm 5$  Ma event are characterized by a wide range in zircon  $\epsilon_{\text{Hf}}(t)$   
127 (between -6 and +15)(Zhu *et al.*, 2022) and whole-rock  $\epsilon_{\text{Nd}}$  (mostly from +5.0 to -3.0). This  
128 more evolved isotopic signature has generally been attributed to the involvement of Indian  
129 continent-derived materials (Chu *et al.*, 2011, Wang *et al.*, 2015).

130 Rocks of the Gangdese arc only rarely have zircon xenocrysts (Zhu *et al.*, 2015). To our  
131 knowledge no xenocrysts have been reported in syn-collisional plutonic rocks in this arc and  
132 only a few have been reported for the Linzizong volcanic rocks (a few xenocrysts formed at ~90  
133 Ma and older, Zhu *et al.*, 2015). This contrasts with rocks from the Ladakh Batholith, the  
134 western continuation of the Gangdese Batholith, which show migmatization and where zircons  
135 define a ca. 20 Ma age range (Weinberg & Dunlap, 2000a, White *et al.*, 2011) including  
136 recycling of 68 Ma zircons in a 49 Ma magma. Despite this exception, the general rarity of  
137 zircon xenocrysts could indicate that: a) remelting of older arc intrusions is a minor process

138 (Jagoutz & Klein, 2018), b) because zircons are rare in mafic arc rocks, few or no zircons are  
139 passed on to the felsic magmas they produce upon remelting, or c) zircon xenocrysts are  
140 resorbed during relatively high-temperature melting (Miller *et al.*, 2003).

141 This paper focuses on an outcrop of the Gangdese Batholith along the road from Zedong to  
142 Nyingchi (Fig. 1a) at N29.2625° and E92.4119° close to Dabu village. Here, a diorite dike  
143 swarm (Fig. 2a, b) intrudes a homogeneous leucocratic tonalite and is back-veined by magmas  
144 resulting from the melting of the tonalite host. The dykes are typically 1-3 m wide and are  
145 continuous for more than 100 m. In detail, the dyke contacts are irregular at the dm-cm scale,  
146 and back-veined (Fig. 2c, d) and dyke tips narrow considerably over a few metres. At the  
147 contact, the tonalite has a centimetric layer of more felsic and finer-grained granitic rock that is  
148 continuous with dykelets intruding the diorite (Fig. 2c). These dykelets are irregular and intrude  
149 and gradually vanish into a heterogeneous diorite (Fig. 2e, f). We have determined whole-rock  
150 chemistry and investigated zircons from three samples of diorite and three samples of tonalite  
151 host rock, all homogeneous at hand-specimen scale.

## 152 **METHODOLOGY**

### 153 **Whole-rock geochemical analysis**

154 Fresh rocks samples were crushed, hand-picked, and then powdered using an agate mill to  
155 a grain size < 200 mesh at the Yuneng Mineral Separation Service Company at Langfang, Hebei  
156 Province, China. Major element analyses of whole rock were conducted on Agilent 7700e ICP-  
157 MS at the Wuhan SampleSolution Analytical Technology Co., Ltd., Wuhan, China. The sample  
158 pre-treatment of whole rock major element analysis was made by melting method. The detailed  
159 sample-digesting procedure was as follows: (1) Sample powder (200 mesh) was placed in an  
160 oven at 105 °C for drying of 12 hours; (2) ~1.0g dried sample was accurately weighed and  
161 placed in the ceramic crucible and then heated in a muffle furnace at 1000°C for 2 hours. After

162 cooling to 400°C, this sample was placed in the drying vessel and weighted again in order to  
163 calculate the loss-on-ignition (LOI); (3) 0.6 g sample powder was mixed with 6.0 g flux and 0.3  
164 g oxidant (NH<sub>4</sub>NO<sub>3</sub>) in a Pt crucible, which was placed in the furnace at 1050°C for 15 minutes.  
165 The flux is a mixture of lithium tetraborate, lithium metaborate and lithium fluoride (45:10:5).  
166 Then, this molten sample was quenched in air for 1 minute to produce flat discs on the fire brick  
167 for the XRF analyses.

168 Zsx Primus II wavelength dispersive X-ray fluorescence spectrometer (XRF) produced by  
169 RIGAKU, Japan, was used for the analysis of major elements in the whole rock, The X-ray tube  
170 is a 4.0Kw end window Rh target. The analytical conditions were voltage: 50kV, current:  
171 60mA. All major element analysis lines are K $\alpha$ . The standard curve uses the national standard  
172 material of China, rock standard sample: GBW07101-14. The data were corrected by the  
173 theoretical  $\alpha$  coefficient method. The relative standard deviation (RSD) is less than 2% and the  
174 average bias of the measurements was of -0.1% for SiO<sub>2</sub> and has its highest values of + 1.3% for  
175 MgO and -1.6% for P<sub>2</sub>O<sub>5</sub>.

176 Trace element analyses of whole rock were conducted on Agilent 7700e ICP-MS at the Wuhan  
177 SampleSolution Analytical Technology Co., Ltd., Wuhan, China. Four rock reference materials  
178 (AGV-2, BHVO-2, BCR-2, and RGM-2) were used to calibrate the contents of trace elements of  
179 analytical samples. The detailed sample-digesting procedure was as follows: (1) Sample powder  
180 (200 mesh) was placed in an oven at 105 °C for drying of 12 hours; (2) 50 mg sample powder  
181 was accurately weighed and placed in a Teflon bomb; (3) 1 ml HNO<sub>3</sub> and 1 ml HF were slowly  
182 added into the Teflon bomb; (4) Teflon bomb was placed in a stainless steel pressure jacket and  
183 heated to 190 °C in an oven for >24 hours; (5) after cooling, the Teflon bomb was opened and  
184 placed on a hotplate at 140 °C and evaporated to incipient dryness, and then 1 ml HNO<sub>3</sub> was  
185 added and evaporated to dryness again; (6) 1 ml of HNO<sub>3</sub>, 1 ml of MQ water and 1 ml internal  
186 standard solution of 1ppm In were added, and the Teflon bomb was resealed and placed in the

187 oven at 190 °C for >12 hours; (7) the final solution was transferred to a polyethylene bottle and  
188 diluted to 100 g by the addition of 2% HNO<sub>3</sub>.

### 189 **LA-ICP-MS zircon U-Pb dating and trace element analysis**

190 Zircons were separated using conventional and magnetic techniques at the Yuneng Mineral  
191 Separation Service Company at Langfang, Hebei Province, China. Cathodoluminescence (CL)  
192 images, obtained at the Institute of Geology, Chinese Academy of Geological Sciences  
193 (Beijing), were used to check the internal textures of single zircons and to select suitable  
194 positions for U-Pb dating and Hf isotope analysis. The zircon U–Pb isotope and trace element  
195 analyses were carried out using LA-ICP-MS at the Mineral Laser Microprobe Analysis  
196 Laboratory (Milma Lab), China University of Geosciences (Beijing). Detailed analytical  
197 procedure was described by Zhang et al. (2019) and provided in Supplementary Data Electronic  
198 Appendix 1 (all the Electronic Appendices may be downloaded from  
199 <http://www.petrology.oupjournals.org/>). A beam diameter of 35 µm was used for the first round  
200 of analyses, whereas for the second round 35 µm was only used for sample 17DB01-2 used and  
201 25 µm for the remainder, which was also used for the third round. Zircon 91500 was used as an  
202 external standard for correcting U–Pb dating, and glass NIST 610 was used as an external  
203 standard for trace element calibration. Off-line analyses were performed using an Excel-based  
204 software ICPMSDataCal (Liu *et al.*, 2008, Liu *et al.*, 2010). Uncertainties in trace element  
205 measurements are between 5 and 10%. Common Pb correction was calculated using the  
206 program ComPbCorr#3.17 (Andersen, 2002). Concordia diagrams and mean calculations were  
207 made using ISOPLOT (v. 3.0) (Ludwig, 2003). Samples were analysed during three sessions,  
208 but they gave similar results (Supplementary Data Electronic Appendix 2) and so we present  
209 merged results.

## 210 **Zircon Hf isotopic analysis**

211 Zircon Hf isotopic analyses were conducted in the same domain of the grain as for U-Pb  
212 analyses, as defined by CL images. Analyses used a Neptune Plus MC-ICP-MS (Thermo Fisher  
213 Scientific, Germany), coupled to a New Wave 193 excimer ArF laser-ablation system at the  
214 Milma Lab, China University of Geosciences (Beijing) with a beam size of 35  $\mu\text{m}$ , laser pulse  
215 frequency of 8 Hz and energy density of 3.7 J/cm<sup>2</sup>. Makeup gas of argon and carrier gas of  
216 helium with the addition of nitrogen mixed in a T-branch pipe prior to introduction into the  
217 MC-ICP-MS. In the experiment, L4 to H3 Faraday cups were used to collect <sup>171</sup>Yb, <sup>173</sup>Yb,  
218 <sup>175</sup>Lu, <sup>176</sup>Hf, <sup>177</sup>Hf, <sup>178</sup>Hf, <sup>179</sup>Hf, and <sup>180</sup>Hf, respectively with the integration time of 0.131 s. The  
219 carrier and makeup gas flows were optimized by a line scan (spot size of 35  $\mu\text{m}$  and scan speed  
220 of 5  $\mu\text{m/s}$ ) ablating NIST SRM 610 to obtain maximum signal intensity for <sup>232</sup>Th, while  
221 minimizing <sup>232</sup>Th<sup>16</sup>O/<sup>232</sup>Th ratio. For each analysis, 50 s integration for gas blank and 50 s  
222 integration for signal collection were set up with a total of 800 cycles of raw data. Zircon 91500  
223 (Blichert-Toft, 2008) was used as an external standard for correcting mass discrimination.  
224 Zircon standard Plešovice (Sláma *et al.*, 2008) and GJ-1 (Morel *et al.*, 2008) were analyzed as  
225 unknown sample that were inserted between zircon 91500 and the samples. Raw data was  
226 converted by Neptune Plus software and then processed using Iolite software (Paton *et al.*,  
227 2011).

228 The initial <sup>176</sup>Hf/<sup>177</sup>Hf ratios and  $\epsilon_{\text{Hf}}(t)$  values were calculated with reference to the chondritic  
229 reservoir (CHUR) at the time of zircon growth from the magmas. The decay constant for <sup>176</sup>Lu  
230 of  $1.867 \times 10^{-11} \text{ year}^{-1}$  (Söderlund *et al.*, 2004), the chondritic <sup>176</sup>Hf/<sup>177</sup>Hf ratio of 0.282785  
231 and <sup>176</sup>Lu/<sup>177</sup>Hf ratio of 0.0336 (Bouvier *et al.*, 2008) were adopted. Depleted mantle model ages  
232 ( $T_{\text{DM}}$ ) were calculated with reference to the depleted mantle at a present-day <sup>176</sup>Hf/<sup>177</sup>Hf ratio of  
233 0.28325, and <sup>176</sup>Lu/<sup>177</sup>Hf = 0.0384 (Griffin *et al.*, 2000). The Hf isotope crustal model age  
234 ( $T_{\text{DM}}^{\text{C}}$ ) was calculated by assuming that its parental magma was derived from an average



235 continental crust, with  $^{176}\text{Lu}/^{177}\text{Hf} = 0.015$ , that originated from the depleted mantle source  
236 (Griffin *et al.*, 2002).

## 237 **SAMPLES: GEOCHEMISTRY AND PETROGRAPHY**

238 Six samples were investigated: three diorites and three tonalites (see Supplementary Data  
239 Electronic Appendix 3 for photographs of the sampling location; coordinates N29.263 and  
240 E92.4112). All diorite samples are homogeneous dark grey, and tonalite samples are white to  
241 light grey. Whole-rock chemistry in Table 1 shows that the diorites are of intermediate  
242 composition ( $53 < \text{SiO}_2 < 58$  wt.%) and the tonalites felsic ( $\text{SiO}_2 = 68\text{-}69$  wt.%). The rocks have  
243  $\text{K}_2\text{O}/\text{Na}_2\text{O} < 1$ , and both rock types are magnesian and calc-alkalic, based on Frost *et al.* (2001)  
244 descriptors (Fig. 3). The diorites are metaluminous, and the tonalites weakly peraluminous (ASI  
245 1.00 to 1.05) (Fig. 3). Trace elements for both rock types are similar, with negative anomalies of  
246 Nb and positive anomalies of Pb and Sr in MORB-normalized diagrams (Fig. 4, Ta also defines  
247 a negative anomaly, not shown). HREE exhibit low values of 0.1 – 1 times MORB values, and  
248 are lower in the tonalites than in the diorites. All samples have Zr/Hf between 35.6 and 40.7, and  
249 La/Yb (not normalized) between 7 and 31 for the tonalite and 6 to 13 for the diorite. Although  
250 the two rock types were emplaced some 30 Myr apart (see section 7 below), they display very  
251 similar geochemical properties, consistent with their arc setting.

252 The diorite dykes are fine-grained and massive, and are composed of plagioclase (~70%-75%),  
253 biotite (~15%-20%), amphibole (~10%-15%) and quartz (~5%-10%). Plagioclase is zoned with  
254 lamellar twinning and the grains are subhedral to euhedral, 100 to 400  $\mu\text{m}$  long, some reaching 1  
255 mm in length, tending towards subequant grains, with crystal faces in some places forming  
256 mosaics with  $120^\circ$  intersection between grains. Amphibole is twinned, anhedral to subhedral,  
257 with green to brown pleochroism and 50-1500  $\mu\text{m}$  long (generally 100-200  $\mu\text{m}$ ). In sample  
258 18DB01-4, the longer Hbl grains include biotite grains. Biotite is subhedral to euhedral, with

259 light-brown to dark-brown pleochroism, forming isolated grains with rectangular sections 100-  
260 1000  $\mu\text{m}$  long (generally 300-400  $\mu\text{m}$ ), or forming aggregates with hornblende. The accessory  
261 minerals are apatite, zircon, epidote and opaque minerals, and sample 17DB01-2 has titanite.  
262 Diorite zircon grains have inclusions and cavities and typically appear in the felsic matrix rather  
263 than as inclusions in the mafic minerals, which lack pleochroic haloes. The nature of the zircon  
264 grains is described in the next subsection. Apatite forms needles reaching 300-400  $\mu\text{m}$ ,  
265 occasionally 600  $\mu\text{m}$ , mostly in the felsic matrix, but can be found included in hornblende and  
266 biotite. Epidote grains can be either included in biotite as subhedral grains, possibly primary, or  
267 in the felsic matrix where it could be a result of alteration of plagioclase. The tonalite is medium  
268 grained (grain-size: 1 to 2 mm), lacking a foliation and is composed of plagioclase (~60%-70%),  
269 quartz (~20%-30%), biotite (~5%-8%), minor K-feldspar, and with apatite, zircon in among the  
270 felsic minerals, and Fe-Ti oxides as accessory phases. Samples 18DB01-3 and 18DB01-1 also  
271 have titanite. Plagioclase occurs mainly as subhedral to euhedral laths. Biotite is anhedral to  
272 subhedral and displays yellowish to dark-brown pleochroism.

### 273 **ZIRCON CATHODOLUMINESCENCE**

274 Zircons from the tonalite typically vary in size from 150 to 250  $\mu\text{m}$  (ranging from 100 to 400  
275  $\mu\text{m}$ ) and are bipyramidal prismatic with well-developed, fine oscillatory zoning (Fig. 6), or  
276 common sector zoning, with some internal truncation of early zonation. Zircons from the diorite  
277 vary in size from 100 to 400  $\mu\text{m}$  and the majority of grains have roughly rectangular shapes  
278 defined by two parallel rationale faces, forming the longer sides of the rectangle, and two  
279 shorter, irregular sides. Some grains have a pyramidal ending. Samples 18DB01-4 and 18DB01-  
280 2 have a second morphological type of zircon comprising euhedral grains, with well-developed,  
281 fine prismatic oscillatory and sector zoning, similar to zircons from the tonalites (compare  
282 grains in Fig. 6c and xenocrysts in Fig. 6d). The latter are considered xenocrysts and comprise  
283 7% of the population (11 grains out a total 162 in the mount for sample 18DB01-4). From this

284 we estimate that they add only ~ 5 ppm Zr to the 74 ppm content of the whole rock for this  
285 sample. Sample 18DB01-2 has an even smaller proportion of these xenocrystic zircons. We  
286 neglect this added amount when considering zircon saturation temperatures below.

287 CL images of zircons from the diorite define three distinct zircon groups (excluding the  
288 xenocrysts in samples 18DB01-4 and 18DB01-2): a) clean and grey grains; b) grains with  
289 considerable clean, grey parts and with metamict domains with cauliflower-like pattern and  
290 partly quenched to black CL; and c) fully metamict grains with or without very thin grey rims  
291 (Fig. 6) that are either entirely or mostly quenched, preserving weak cauliflower-like patterns in  
292 very dark regions. Based on these distinctions, the spots were divided into 4 types depending on  
293 their position: Type 1 are from clean and grey areas in grains from group (a); Type 2 are spots  
294 from the clean, grey part of grains from group (b), and Type 3 are from the metamict part of the  
295 same grains; and Type 4 are spots from fully metamict, quenched grains of group (c). Types 3  
296 and 4 are commonly associated with anomalous zircon trace element compositions as we will  
297 see in the next subsection.

## 298 **ZIRCON GEOCHEMISTRY**

299 Zircons from the tonalite host rock and xenocrysts from diorites have similar trace element  
300 composition, with U and Th contents below 2100 and 1800 ppm, respectively, similar REE  
301 patterns (Fig. 7, Supplementary Data Electronic Appendix 2), and Ti contents between 1 and 10  
302 ppm (Supplementary Data Electronic Appendix 2). These values contrast starkly with the  
303 autocrysts from the diorite that show higher abundances of REE (Fig. 7) and anomalously high  
304 values of U-Th-Ca-Fe-Y, each with values approaching or surpassing 1 wt.% (Fig. 8) (for more  
305 zircons with high trace element contents see Gagnevin *et al.*, 2010). Their Ti contents are  
306 between 1 and >500 ppm (15 out 260 analyses yielded Ti > 30 ppm) (Fig. 8d).

307 Hafnium is an incompatible element during crystallization of felsic magmas (Claiborne *et al.*,  
308 2010), with a bulk partition coefficient remaining below one even during zircon crystallization,  
309 despite zircon's high Hf uptake. Conversely, titanium, is a compatible element that enters mafic  
310 silicates and common accessories, such as Fe-Ti oxides and titanite. Thus, during magma  
311 crystallization, Hf increases while Ti decreases in the melt leading to the negative trend of Hf  
312 against Ti in Fig. 9. The same is not true for U, Th and Yb, which show unexpected positive  
313 trends against Ti, for diorite zircons, indicative of an apparently compatible behaviour of these  
314 elements during crystallization (Fig. 9), contrasting with the incompatible trends in Claiborne *et*  
315 *al.* (2010).

### 316 **ZIRCON U-Pb AGES AND Hf ISOTOPES**

317 The three tonalite and three diorite rock samples in Table 1 were dated. The diorite samples  
318 yielded ages of 46-47 Ma and the tonalite samples yielded ages of 77-79 Ma and (Figs. 10 and  
319 11). Given the close mean ages for the diorite samples and their relatively large spread,  
320 indicated by high MSWDs (>4), we consider that the dykes were essentially contemporaneous.  
321 Zircons with CL types 3 and 4 with quenched, metamictic CL features, tend to be richer in U,  
322 Th and other trace elements compared to types 1 and 2 (Fig. 8). In order to determine if types 3  
323 and 4 have been affected by Pb-loss, U-Pb dates were compared with those for CL types 1 and 2  
324 (Figs. 10d and 12). Results show no significant differences and dates vary from ~44 to 51 Ma  
325 independently of CL type. We have therefore considered all concordant U-Pb analyses.

326 Two tonalite samples have ages that overlap within error at ~79 Ma and have small MSWD  
327 (Fig. 11a,c). The third sample, however, has a slightly younger mean age at  $77.2 \pm 0.5$  Ma and a  
328 high MSWD=4.8 (Fig. 11b). This sample has three times more analyses than the other two,  
329 suggesting that the tonalites may have a large true spread in dates. Two of the three diorite  
330 samples (Fig. 11d-e) have xenocrysts with the same range of dates and same trace element

331 chemistry as the tonalite zircons (Fig. 7) confirming the interpretation based on CL images (Fig.  
332 6). Analyses with >10% discordancy as well as a small number of outliers were not considered  
333 here.

334 Hafnium isotopes for subpopulations of the dated zircons from all 6 samples were obtained.  
335 They are typical of those of the Gangdese arc yielding  $\epsilon_{\text{Hf}(t)}$  between +4 and +13 (Fig. 13;  
336 *Supplementary Data Electronic Appendix 2*). The values for the tonalites are similar to those of  
337 the diorite with the exception that the latter have a wider variation (+4 to +13 compared to +6 to  
338 +10). Xenocrysts of diorite sample 18DB01-4 plot together with the tonalite zircons.

## 339 **CHEMICAL MODELLING OF MELT EVOLUTION AND ZIRCON** 340 **CRYSTALLIZATION**

### 341 **Methods**

342 The crystallization of zircons during cooling of magmas has been modelled using a procedure  
343 similar to the ones described by Schiller and Finger (2019) (see also Harrison *et al.*, 2007,  
344 Kirkland *et al.*, 2021). In a cooling closed system, magma crystallizes and the residual melt  
345 evolves chemically. Zr is initially incompatible and its content increases until zircon becomes  
346 saturated at which point it becomes compatible and starts decreasing in the melt upon further  
347 fractionation. Thus, zircon crystallizes out of this residual melt, whose composition evolves and  
348 differs from the composition of the bulk rock. In a closed-system, the melting process upon  
349 heating follows the opposite direction to the one described above.

350 In our models, we first calculate the closed-system evolution of the rock using phase equilibria,  
351 and in particular the amount and composition of the residual melt at a given temperature. Zr is  
352 partitioned between melt and solids using known partition coefficients, and the Zr content in the  
353 melt is compared with the zircon saturation value; any Zr above the saturation value at this point

354 is then used to form zircon. Other trace elements are then partitioned between liquid and all  
355 solids, zircon included. The most important assumptions in this process are that the composition  
356 of the diorite and tonalite correspond to melt compositions, and that this is a closed system  
357 behaviour, i.e. we assume batch rather than fractional crystallization (or indeed batch melting, as  
358 both are exactly similar in a closed system): neither melt nor crystals are removed from the  
359 system, and the system properties are calculated independently for each point.

360 The details of the procedure are given in Supplementary Data Electronic Appendix 5. Phase  
361 equilibrium is modelled using PerpleX version 6.9.0 (Connolly, 2005, Connolly & Pettrini,  
362 2002) and the minerals and melt models by Holland et al. (2018), that allow incorporation of  
363 Fe<sup>3+</sup> and Ti, using one-dimensional T profiles at a fixed P of 5 kbar. Zircon saturation values are  
364 based on the saturation model of Boehnke et al. (2013) and results for the model of Watson and  
365 Harrison (1983) are also shown for comparison. These models include a dependence on the melt  
366 composition expressed as the parameter M, the cation ratio (Na + K + 2Ca)/(Al x Si), which is  
367 obtained from the phase equilibrium model. Partition coefficient values for trace elements vary  
368 considerably in the literature. We use those compiled by Laurent (2012), using values for felsic  
369 rocks (SiO<sub>2</sub> > 63 %), which are appropriate for both rock types since the residual melt, even in  
370 the diorite, is almost always at these values. For Th, U, HFSE and REE, the zircon-melt  
371 partition coefficients are modified using the temperature parametrization of Claiborne et al.  
372 (2018). Temperature-dependent coefficients for other minerals are unavailable and have the  
373 potential to modify our results. Finally, we calculated Ti contents in zircon as a function of  
374 temperature using the model of Ferry and Watson (2007). As their equation relies on the activity  
375 of Si and Ti, both were calculated from the phase equilibrium model (following Schiller &  
376 Finger, 2019). PerpleX outputs chemical potentials that must be converted into activities.

377 Given the pressure dependence of ~5 °C/kb for the Ti-in-zircon thermometer determined by  
378 Ferry and Watson (2007), our calculated temperatures could be overestimates for the lower

379 pressure used here (5 kb) compared to the 10 kb used in Ferry and Watson's calibration. All  
380 parameters are calculated along the 1D temperature profile used for phase equilibrium,  
381 simulating closed-system cooling (or heating) of the magma or the rock. After the phase  
382 equilibrium modelling, all steps are performed using a homemade R script (available from J-F  
383 Moyen on request).

#### 384 **Evolution of melt and zircon**

385 Crystallization of a melt in a closed system is modelled using diorite sample 18DB01-4, the  
386 most mafic of the diorites with 54% SiO<sub>2</sub> and 73 ppm Zr. We carried out two calculations, with  
387 3 and 6 % H<sub>2</sub>O. A value close to the average of the tonalite samples was used with SiO<sub>2</sub> =  
388 68.3 % and 140 ppm Zr (Table 1). A low H<sub>2</sub>O content of 2 wt.% was assumed for modelling the  
389 tonalite in order to investigate its remelting triggered by limited quantities of H<sub>2</sub>O delivered  
390 from the diorite intrusion.

391 In the model, the diorite crystallizes Amp-Pl-Cpx accompanied later by Bt that increases in  
392 proportion towards the end of the crystallization history, with quartz appearing close to the  
393 solidus temperature ( $T_{\text{sol}}=677$  °C; Fig. 14a). Water saturation is reached at 687 °C, close to the  
394 solidus for the case with 3 wt.% H<sub>2</sub>O, and at 754 °C for 6 wt.% H<sub>2</sub>O, nearly 80 °C above the  
395 solidus. The tonalite crystallizes Pl+Opx at high temperature and at ~800 °C, Opx reacts to Bt.  
396 Kfs appears relatively late in the history and H<sub>2</sub>O becomes saturated a few degrees above the  
397 solidus ( $T_{\text{sol}}= 650$  °C). The evolution of the melt fraction for all calculations is depicted in Fig.  
398 14b.

399 The Zr content in the melt increases with crystallization until the melt reaches zircon saturation  
400 (Fig. 14c). After this point the melt follows the zircon saturation curve controlled primarily by  
401 temperature and secondarily by melt composition, expressed by its M-value that evolves as

402 crystallization proceeds (Fig. 14d). The temperature of zircon saturation for the diorite with 73  
403 ppm Zr in the melt at the start is 714 or 711 °C using Boehnke et al.'s (2013) calibration, and is  
404 only weakly sensitive to the H<sub>2</sub>O content, corresponding to melt fractions of 23 to 26 %,  
405 respectively. The saturation temperature is ~ 30 - 40 °C higher when using the calibration of  
406 Watson and Harrison (1983) corresponding to melt fractions of 26 to 35 wt.%. For the case with  
407 6 wt.% H<sub>2</sub>O, zircon saturation is reached at temperatures lower than H<sub>2</sub>O saturation. The tonalite  
408 initially with 140 ppm Zr and 2 wt.% H<sub>2</sub>O reaches zircon saturation at 805 °C and 41% melt  
409 (Boehnke *et al.*, 2013), while H<sub>2</sub>O becomes saturated a few degrees before the solidus at 650 °C.  
410 Thus, zircon saturation temperature of the tonalite is ~ 150 °C above the solidus and 100 °C  
411 higher than that of the diorite due to its lower M-values and higher Zr content (140 ppm vs 73  
412 ppm).

413 For the diorite models, crystallization leads to a gradual decrease in the M value of the melt  
414 fraction from close to 2.2 at the liquidus, to a minimum of 1.4 at the solidus (Fig. 14d). The  
415 tonalite is different. M values vary only weakly, first decreasing from M=1.45 at the liquidus  
416 (not shown) to 1.32 at the start of crystallization of quartz and biotite at which point M increases  
417 gently reaching 1.40 at the solidus, similar to the residual melt in the diorite close to its solidus.  
418 The  $a(\text{SiO}_2)$  and  $a(\text{TiO}_2)$  in Fig. 14e were used to calculate the expected value of Ti-in-zircon.  
419 Despite considerable variation in activities during crystallization, the calculated Ti-in-zircon  
420 curves are similar to those calculated using fixed value of  $a(\text{SiO}_2) = 1$  and  $a(\text{TiO}_2) = 0.7$  (compare  
421 continuous and dashed lines in Fig. 14f). Thus, these values are a good approximation of the  
422 behaviour of the metaluminous magmas (see discussion in Schiller & Finger, 2019).



423 Modelling results indicate that prior to zircon saturation in the dioritic magma, most Zr is hosted  
424 in the melt with some going initially into hornblende and biotite as magma cools. At zircon  
425 saturation, nearly half the Zr is hosted by these other minerals (Fig. 14g) but as the proportion of  
426 zircon increases, these non-zircon minerals record a decrease in the total Zr content that they  
427 host. At the solidus, a little over 20 ppm is hosted by non-zircon minerals, and the remaining  
428 ~50 ppm is hosted by zircon, corresponding to a (modal) proportion of just under 0.01 % zircon.  
429 During tonalite crystallization, few minerals take in Zr, so nearly all of the ~140 ppm is hosted  
430 in zircon, corresponding to about 0.03 modal % in the rock.

431 The decrease in Zr content hosted by non-zircon minerals is a result of the modeling calculations  
432 considering the whole-rock chemical composition and distributing the available elements  
433 according to the mineral proportions stable at the new temperature. This means that minerals  
434 and melt are in equilibrium at all times during cooling. After zircon becomes saturated, the Zr  
435 content in the melt decreases as temperature decreases so that the amount of Zr that goes into the  
436 non-zircon minerals decreases according to the partition coefficient, kept constant. In a real  
437 system, complete equilibrium at all times during cooling may not occur. In this case, some Zr  
438 may be trapped in early-formed minerals, in disequilibrium with the cooling melt. The net effect  
439 would be slightly less zircon being formed than in the calculations presented.

## 440 **DISCUSSION**

### 441 **Ages and source of xenocrysts**

442 Field evidence in Fig. 2 indicates that tonalite remelted at the contact with the diorite and back-  
443 veined the dykes, causing hybridization that is recorded by felsic dykelets and irregular diffuse  
444 leucocratic patches in the diorite. Melting of the tonalite is inferred to be at relatively low  
445 temperatures in the presence of aqueous fluids because of the leucocratic nature of the tonalites

446 with little biotite available and no anhydrous peritectic phase such as garnet or orthopyroxene  
447 associated with anatexis.

448 The 46-47 Ma age of the diorite dykes places them amongst the syn-collisional, compositionally  
449 diverse magmatic flare-up recorded in the southern Lhasa terrane centred around  $\sim 50 \pm 5$  Ma  
450 (Zhu *et al.*, 2019). These rocks typically have a wide range of  $\epsilon_{\text{Hf}(t)}$  varying between -6 and +15  
451 (Fig. 4 in Zhu *et al.*, 2022). The tonalite age of 77-79 Ma with  $\epsilon_{\text{Hf}(t)} = +9 \pm 1$  makes it part of  
452 the pre-collisional magmatism that had  $\epsilon_{\text{Hf}(t)}$  values between +4 and +15.

453 Two out of three diorite samples have older zircon xenocrysts (sample 18DB01-4 and 18DB01-  
454 2) that comprise  $\leq 7\%$  of the grains imaged for each diorite sample. These xenocrysts are likely  
455 derived from the tonalite host rock as they have the same distinctive euhedral prismatic shape  
456 and internal CL zonation (Fig. 6), similar  $\epsilon_{\text{Hf}(t)}$  values (Fig. 13), the same range of U-Pb dates  
457 from  $\sim 80$  Ma to 69 Ma (Fig. 11) and similar trace element composition (Fig. 7).

#### 458 **Anomalous zircon composition**

459 Figures 8 and 9 indicate that the diorite zircons have anomalous trace element composition.  
460 They have very high trace elements contents, such as U-Th-HREE-Y-Ti, and low values of  
461 LREE index (LREE-I, Bell *et al.*, 2016). The elements U, Th and Y define positive trends with  
462 Ti. Given that Ti is expected to decrease in zircon during cooling and melt fractionation, the  
463 trends suggest that these elements behave compatibly during crystallization, contrary to  
464 expectations (Claiborne *et al.*, 2010). Hf is incompatible in the melt defining a negative trend  
465 against Ti, as expected, but unexpectedly it also defines a negative trend against U due to its  
466 compatible behaviour. The high contents of trace elements indicate the that self-irradiated,  
467 damaged diorite zircons may have been altered as a result of reaction with melts or fluids

468 (Geisler *et al.*, 2007, Hoskin, 2005, Hoskin & Schaltegger, 2003). For example, the values of Ti  
469 in some analyses are above 30 ppm, reaching up to a few hundred ppm, and these are generally  
470 accompanied by high concentration of other trace elements (Fig. 8).

471 Metamict and quenched zircon types 3 and 4 (Fig. 6) tend to have high concentration of trace  
472 elements (Ca, Fe, REE, U and Th) in contrast to zircon types 1 and 2 (Fig. 8). Despite these  
473 differences, they all yield similar U-Pb dates with no systematic change that could be ascribed to  
474 Pb-loss (Figs. 10d and 12). In order to determine the extent of alteration, we investigated the  
475 relationships between CL types (Fig. 6) and trace element chemistry for each analytical spot,  
476 considering signal counts of each analysis during data acquisition using the ICPMSDataCal  
477 software. The main findings are that spots with anomalously high trace element abundances  
478 typically have one or more of these features:

- 479 a) high Th+U contents (>3000 ppm) commonly but not always located in zones of  
480 quenched CL. We note however, that there are quenched areas with low Th+U contents  
481 (<1000 ppm) indicating that quenching may be related to other factors;
- 482 b) anomalous values of LREE, expressed by low values of LREE-I (Fig. 8a,b);
- 483 c) anomalous signal plateaus of Fe in CL quenched areas, commonly accompanied by other  
484 anomalous signal plateaus for Ca, Ti, LREE, Th and Y (Fig. 15), probably a result of  
485 inclusions or domains affected by self-irradiation damage and reaction between zircon  
486 and fluid or melt (Geisler *et al.*, 2007);
- 487 d) located in zircon sectors characterized by CL types 3 and 4.

488 We found that taking any of these indicators separately is an insufficient predictor of the spot  
489 having a number of chemical anomalies. The strongest predictor of zircons having several such  
490 anomalies is having anomalous peaks or plateaus in the count curves, in particular for Fe and  
491 Ca. Therefore, we used anomalous peaks or plateaus of Fe and Ca as key indicators of

492 metamictization and re-equilibration (Geisler *et al.*, 2007) and exclude these analyses from  
493 consideration in Ti-in-zircon thermometry. While in most cases, analyses with anomalies of Fe  
494 and Ca generally have at least one other feature in the list above, there is a very small number of  
495 analyses that have no other indicator of alteration. These were also removed. We have checked  
496 the remainder of the data for Ti count anomalies, and found only four analyses with minor Ti  
497 anomalous peaks or plateaus. These lacked Fe or Ca anomaly and were therefore evaluated with  
498 the rest of the results in the next section.

499 Uranium, Th and HREE normally behave incompatibly during crystallization and are expected  
500 to define a negative trend when plotted against Ti contents (Claiborne *et al.*, 2010). However,  
501 these elements in diorite zircons behave compatibly defining a positive trend instead (Fig. 9). In  
502 order to further evaluate this behaviour, we have compared the observed data with modelled  
503 zircon composition. For both tonalite and diorite, zircon composition is scattered, and modelled  
504 composition evolution reproduces them poorly (Fig. 16). The analytical results define a  
505 positively correlated array, at high angle to the negative trend of the model calculations or the  
506 trend defined by the zircons of Claiborne *et al.* (2010) (grey field in Fig. 16). This means that the  
507 processes controlling zircon trace element intake in the diorite is unaccounted for by our  
508 calculations and used assumptions.

### 509 **Ti-in-zircon thermometry**

510 In this section, only zircons that passed the culling described above, deemed as potentially  
511 unaltered, were considered. As we have seen in section 8, converting Ti contents to temperatures  
512 requires assumptions regarding  $\text{TiO}_2$  and  $\text{SiO}_2$  activities. Figure 14f compares two results, one  
513 using “conventional” estimates of  $a(\text{SiO}_2) = 1$  and  $a(\text{TiO}_2) = 0.7$ , and the other using the  
514 calculated activities at each point during crystallization (Fig. 14e). The difference between the  
515 two is small.

516 *Zircons from tonalites*

517 Analyses of 122 spots from the three tonalite samples and xenocrysts from the diorite, yielded a  
518 range in Ti contents from 1.2 to 9.2 ppm (1.2 to 8.5 ppm for the xenocrysts), with a very similar  
519 mean (3.3 ppm for the tonalites, 4.0 ppm for the xenocrysts). These values yield temperatures  
520 (using ideal activities) from 577 to 786 °C. Uncertainties for Ti values between 1-2 ppm are  
521 between 20-30%, decreasing to below 10% for values >5 ppm, with a detection limit of ~0.5  
522 ppm. While the low-T end of the range likely reflects sub-solidus resetting, the high-T end is  
523 lower than but comparable to the zircon saturation temperatures estimated at between 800 and  
524 820 °C (depending on the model used, Fig. 14c).

525 *Zircons from diorites*

526 The Ti-in-zircon values of diorite autocrysts are less well-behaved. Zircons from  
527 sample 18DB01-4 have Ti contents between 1.4 and 17.7 ppm, which translates to temperatures  
528 between 613 and 895 °C (using  $a(\text{SiO}_2) = 1$ ,  $a(\text{TiO}_2) = 0.7$ ), or 614 and 842 °C (using activities  
529 from our model). Since our models also predict the onset of zircon crystallization at low  
530 temperatures (710 - 750 °C depending on the model chosen, Fig. 14c), this is a significant  
531 mismatch, and these “hot” zircons cannot be simply related to zircon saturation temperature  
532 estimates.

533 Similarly, for sample 17DB01-2, Ti ranges between 1.3 and 16.3 ppm (equivalent to a  
534 maximum T of 832 °C), with a mean of 7.9 ppm. Sample 18DB01-2 (with higher Zr = 102 ppm  
535 and hence a higher value of the zircon saturation temperature) has Ti contents between 1.5 and

536 23.3 ppm (equivalent to a maximum T of 915 °C), and a mean of 7.1 ppm. Thus, in all cases the  
537 maximum Ti-in-zircon temperatures are more than 100 °C above the estimated zircon saturation  
538 temperature, when the diorite still had ~40-55% melt fraction depending on the H<sub>2</sub>O content. In  
539 all cases, the calculated temperatures for the lowest Ti grains are up to 50 °C below the solidus.  
540 As our model relies on zircon saturation in melt, we cannot model subsolidus resetting of Ti  
541 composition (discussed in Fu *et al.*, 2008).

#### 542 *Modelling zircon crystallization*

543 While the tonalite zircons yield Ti-in-zircon temperatures that cover the expected range derived  
544 from the calculations, the diorite zircons do not. For these, the maximum Ti-in-zircon  
545 temperatures surpass substantially the modelled zircon saturation temperature in common with  
546 findings elsewhere (Barnes *et al.*, 2019, Claiborne *et al.*, 2006, Harrison *et al.*, 2007).

547 There are two ways of calculating the zircon saturation temperatures. One approach uses the  
548 whole-rock composition as an estimate of the magma composition. It assumes that zircon would  
549 crystallize from a liquid whose composition equates that of the rock, for which a high M value  
550 results in unrealistically high Zr solubility and low saturation temperatures (see Harrison *et al.*,  
551 2007). In this case, diorite sample 18DB01-4, with M=2.4, would yield a saturation temperature  
552 of 575 °C, which should preclude it from crystallizing zircon. This mismatch with reality is

553 because the approach does not include the evolution of the residual melt with crystallization,  
554 which would cause the Zr content to increase and the melt composition to evolve to lower M  
555 values, with lower Zr solubility.

556 The second approach, the one taken here, considers the evolving composition of the melt during  
557 crystallization and determines when zircon crystallizes from this residual liquid, whose  
558 composition departs from the bulk composition, becoming enriched in Zr and increasingly more  
559 felsic (lower M) (Harrison *et al.*, 2007, Lee & Bachmann, 2014). This approach leads to higher  
560 and more realistic zircon saturation temperatures than the first approach (Harrison *et al.*, 2007).

561 Here, using this approach and including Zr uptake by other minerals such as Hbl, Bt and Pl, we  
562 found zircon saturation occurs just above 700 °C for the diorite models, some 100 °C lower than  
563 the maximum values derived from Ti-in-zircon, as seen in the previous subsection. This  
564 discrepancy implies that some other processes must be at play.

#### 565 *Significance of high-Ti zircons*

566 A population of zircons from the diorites show Ti contents > 7 ppm, corresponding to > ~730  
567 °C, higher than the zircon saturation temperature derived from our models. These same diorite  
568 zircons have high contents of U, Th, HREE that define apparently compatible trends (Figs. 9  
569 and 16). Several explanations, not necessarily mutually exclusive, could account for these  
570 observations:

- 571 a) High-T zircons are xenocrysts or antecrysts. This is unlikely because the high-T zircons have  
572 the same internal texture,  $\epsilon_{\text{Hf}(t)}$  and U-Pb ages as low-T grains.
- 573 b) Presence of inclusions or “non-formula” impurities in zircons. The diorite zircons do have  
574 inclusions and cavities and are also partly metamictic with quenched CL images. The high-Ti  
575 values, coupled with high Th and REE values, could be due to inclusions of Ti-rich phases, such  
576 as titanite or allanite, where the trends with Ti would represent mixing lines. We have excluded  
577 analyses with anomalous peaks or plateaus of trace elements in the count curves (section 9.2),  
578 and modelling results show that inclusions of titanite would cause a much more rapid increase in  
579 Ti contents compared to Nd (Fig. 16a). However, it is possible that metamictization and reaction  
580 with fluids and subsequent recrystallization (Geisler *et al.*, 2007) gave rise to micrometer-scale  
581 inclusions of assorted Ti-U-Th-REE rich minerals in the zircon matrix. Alternatively, self-  
582 irradiation damage gave rise to pore space that hosts “non-formula” impurities (Geisler *et al.*,  
583 2007). At present, either alternative is valid and we conclude that despite exclusion of  
584 anomalous analyses, the Ti contents of the remaining zircons may also have been affected,  
585 explaining the high-Ti contents and positive trend between Ti and U-Th-Yb (Fig. 9). If this is  
586 the case, the Ti-in-zircon values of the diorite zircons do not reflect temperature of  
587 crystallization (Fu *et al.*, 2008).
- 588 c) Loss of Zr during diorite crystallization (Barnes *et al.*, 2019). In this case, the original melt  
589 had higher Zr content than the bulk rock has now, because some of the high-Zr melt was  
590 extracted leaving behind a poorer cumulate. If the diorite melt had initially higher Zr than the  
591 final rock, it would have reached zircon saturation at higher temperatures than the ones



592 calculated in Fig. 14. The interstitial melt of a crystallizing dioritic magma becomes increasingly  
593 enriched in Zr until zircon saturation, at which point the melt starts to lose Zr due to zircon  
594 precipitation (Barnes *et al.*, 2019, Harrison *et al.*, 2007, Lee & Bachmann, 2014). If part of this  
595 Zr-rich interstitial melt is extracted, the remaining mush or magma will be impoverished in Zr,  
596 while retaining some of the early-formed high-T zircons. Any remaining interstitial melt  
597 continues to crystallize zircon as the magma continues to cool. Thus, despite relatively low final  
598 Zr content, this rock will have early-formed hot zircons that mark the true, high-saturation  
599 temperature of the original magma (see Barnes *et al.*, 2019). This alternative is problematic for  
600 the Dabu rocks because to reach zircon saturation at ~830-840 °C (the upper temperatures  
601 obtained by Ti-in-zircon thermometry for our samples), the dioritic melt would need to have had  
602 an unrealistically high Zr content of >300 ppm. Therefore, while this process may have  
603 contributed to decreasing the Zr content of the evolving magma, and therefore the inferred  
604 zircon saturation temperature, it is unlikely to be the main reason for the high Ti-values of some  
605 zircons.

606 On balance, it is likely that the trace element trends in Fig. 9 and the Ti-content of diorite  
607 zircons reflect zircon alteration during metamictization, where high contents of trace elements  
608 are hosted either in pore space in amorphous remnants inside the grains or in inclusions resulting  
609 from recrystallization of the amorphous, damaged zones (Geisler *et al.*, 2007). Consequently, the  
610 Ti content in the diorite zircons is not a reliable measure of crystallization temperature.

### 611 **Preservation of euhedral zircon xenocrysts**

612 Euhedral zircon xenocrysts from the tonalite preserved in two diorite samples (18DB01-4 and  
613 18BD01-2) show negligible dissolution. This is inferred from the similarity between CL images  
614 of xenocrysts and tonalite zircons: they are euhedral with well-developed oscillatory zoning,

615 lacking obvious truncation of the oscillatory zoning in the outer part of the zircons. It is possible  
616 that a thin rim may have been dissolved or grown during final crystallization of the diorite, but  
617 they have not been recognized. In this section, we explore how these euhedral xenocrysts may  
618 have been preserved during the melting of the tonalite and mixing with the diorite, two steps  
619 where they could have been resorbed.

620 We envisage three possible processes that would prevent significant zircon resorption during  
621 melting of tonalite: small melt fraction during anatexis, zircon grains protected as inclusions in  
622 biotite, or rapid melting and transfer to the diorite with little time for resorption. All alternatives  
623 remain open. Once transferred to the dioritic magma, zircon xenocrysts would be partly or  
624 completely resorbed if the diorite was undersaturated. The fact that they are well preserved, and  
625 that corroded oval zircons or zircon cores have not been found, can be interpreted in several  
626 ways (see discussion in Barnes *et al.*, 2019, Miller *et al.*, 2007):

627 1. A zircon-undersaturated diorite magma crystallized rapidly after receiving the  
628 xenocrysts preventing their dissolution. While we cannot entirely dismiss this possibility,  
629 we note that: the diorite is fine-grained but not aphanitic or glassy, and lacks chilled  
630 margins against the host rock; granitic magma mixed with the mafic magma, suggesting  
631 that there was enough time for interaction and widespread transfer of zircons; and the  
632 diorite magma produced zircon autocrysts up to 0.4 mm long with rational crystal faces  
633 after it became zircon-saturated at low T. Combined, these features suggest that if the  
634 diorite magma was undersaturated, there would have been enough time for the xenocrysts

635 to be partly consumed before the magma becoming saturated and crystallizing its own  
636 zircon autocrysts.

637 2. Zircons could have been transferred as inclusions in residual biotite from the  
638 tonalite in the granitic melt (e.g. Clemens, 2003). However, we found no pleochroic haloes  
639 in biotite in the diorite (Fig. 5) and biotite would have been unstable in the dioritic magma  
640 at  $T > 810$  °C (for the diorite with 3 wt.%  $H_2O$ ), or  $> 750$  °C (for 6 wt.%  $H_2O$ ) (Fig. 14a). In  
641 this case, biotite would have reacted out and zircons exposed to the melt. Thus, armouring  
642 would have been possible only if biotite transfer occurred at relatively low temperatures,  
643 for which the diorite would have been a mush with  $< 40\%$  melt (Fig. 14b). While we cannot  
644 discount this possibility, we do not find support for it.

645 3. If we reject the results from Ti-in-zircon thermometry considering that it could  
646 have been affected by alteration, and consider instead that the zircon saturation  
647 temperatures in Fig. 14 approach the true value, then the Dabu diorite would have reached  
648 zircon saturation between 700 to 750 °C. At these conditions, the diorite would have been a  
649 crystalline mush with only between  $\sim 23\%$  and  $\sim 26\%$  interstitial melt. In this case, the  
650 extensive magma mixing observed within the dyke would require either pervasive flow of  
651 the granitic melt through the mush, or liquefaction of the mushy diorite possibly caused by  
652 the addition of melt derived from tonalite anatexis.

653 Bringing together the field evidence, the data and the considerations regarding zircon saturation  
654 temperature (point 3 above), we propose the following sequence of events (Fig. 17): the dykes  
655 were paths of H<sub>2</sub>O-rich dioritic magmas that released heat and H<sub>2</sub>O to the surroundings as the  
656 magma became a crystalline mush. This triggered water-fluxed melting of the tonalite that  
657 released zircon grains into an anatectic granitic melt. This melt back-veined and mixed with the  
658 diorite transferring tonalite zircons to the dioritic magma, where they remained stable (or nearly  
659 so), explaining their well-preserved euhedral shapes and internal zonation. Preservation of the  
660 xenocrysts could have been either through armouring, for which we find no evidence, or through  
661 transfer to a zircon-saturated dioritic medium. Even assuming large uncertainties in the Zr  
662 content of the original melt caused by melt gain or loss during crystallization, zircon saturation  
663 temperature would have been reached when the diorite was a crystalline mush. Therefore,  
664 zircons were likely transferred to a dioritic mush through mixing. How did this occur? Mushes  
665 are permeable solids, open to invasion of foreign magmas (Xu *et al.*, 2021) and prone to  
666 liquefaction (Weinberg *et al.*, 2021). The granitic magma may have exploited permeable porous  
667 pathways through the mush leading to hybridization and influx of zircon xenocrysts into the  
668 matrix of the mush. This same ingress of granitic magma may have caused liquefaction and  
669 remobilization of the mush favouring further mixing. Both these processes could give rise to the  
670 variety of mingling features in Fig. 2c,d, including the irregular, infolded felsic dykes commonly

671 with gradational contacts with the mafic rocks, and blocks of better-preserved diorites in a  
672 hybrid rock. A detailed textural investigation of the different steps in the hybridization process  
673 in Fig. 2, with particular focus on disequilibrium textures and mineral zonation, might better  
674 reveal the nature of these processes. Determining the existence of narrow, younger rims around  
675 the xenocrysts, and with that better visualizing the shape of the xenocrystic grains, might help  
676 support this interpretation.

## 677 CONCLUSIONS

678 The intrusion of the Dabu diorite dyke swarm at 46-47 Ma is part of the waning stages of the  
679 syn-collisional magmatic flare-up of the Gangdese belt. The outcrops in Dabu record how these  
680 dykes assimilated the 77-79 Ma host tonalite by remelting it and then mixing with the newly  
681 formed melt. The tonalite melted at low temperatures fluxed by water likely released with heat  
682 by the dykes. The transfer of tonalite zircons to and their preservation in the diorite dykes  
683 provides an opportunity to explore the conditions of magma hybridization and the limits of  
684 zircon-based thermometry. Given the importance of dykes as feeders of large magma bodies,  
685 and the high H<sub>2</sub>O contents and temperatures prevalent in active magmatic arcs, the Dabu dykes  
686 could represent a common process of hybridization in magmatic arcs, akin to the mixing-  
687 assimilation-storage-homogenization, MASH, hypothesis (Hildreth & Moorbath, 1988).

688 We found that the Ti-in-zircon temperature estimations for the tonalite matched well the range  
689 defined by zircon saturation temperature predicted by modelling of crystallization/melting of the  
690 tonalite. However, the same is not true for dioritic zircon autocrysts. These yield Ti-in-zircon  
691 temperatures ranging from below the solidus to >100 °C above the zircon saturation  
692 temperatures. This discrepancy could be related either to loss of Zr during diorite crystallization  
693 (Barnes *et al.*, 2019) or to alteration and recrystallization of the zircons (Geisler *et al.*, 2007),  
694 indicated by quenched CL and high Ti contents, as well as U, Th, Ca, Fe, Y, REE (or low

695 LREE-I; Fig. 8). Either way, the results show how even through exclusion of zircons with  
696 obvious indicators of alteration, they may still have unreliable Ti values, defining unexpected  
697 trends against other trace elements (Fig. 16).

698 Interestingly, but not surprisingly, the tonalite with ~140 ppm Zr has a zircon saturation  
699 temperature close to 100 °C higher than the diorite with half the amount of Zr, indicating yet  
700 again that this temperature does not constrain the temperature of magma formation. However,  
701 for the Dabu rocks, zircon saturation temperature is useful in constraining the crystallinity of the  
702 diorite intrusion at the time of hybridization. This is because a striking feature of these rocks is  
703 that the zircon xenocrysts from the tonalite record little resorption, requiring that the xenocrysts  
704 be either armoured in biotite during mixing, or that they be exposed to a low-temperature  
705 granitic melt first, and then transferred to a zircon-saturated diorite. The absence of pleochroic  
706 haloes in biotite in the diorite and the instability of biotite in hot dioritic magmas suggest that  
707 armouring is unlikely. The low-temperature zircon saturation of ~715 °C ensures that the diorite  
708 would have been a high crystallinity mush with only ~25 wt.% melt at the time of zircon  
709 saturation. Even if the Zr content were doubled or trebled, zircon saturation in the diorite would  
710 still have occurred in a mush. Thus, we conclude that hybridization occurred in a zircon  
711 saturated mush through melt leak-off from invading granitic veins into the pore-space of the  
712 mush, possibly accompanied by liquefaction (Weinberg *et al.*, 2021). We argue that pore-  
713 invasion combined with the liquefaction of mushes is a powerful mixing process. Because of its  
714 stealthy nature, this process of magma mixing in dykes could be important during the build-up  
715 of arcs feeding large magma reservoirs with hybrid magmas.

716 The Dabu dyke swarm represents one end-member of zircon behavior during hybridization  
717 where xenocrysts are preserved with minimal resorption. This behavior helped us constrain the  
718 nature and conditions of zircon transfer and magma hybridization. However, the general rarity  
719 of zircon xenocrysts in magmatic rocks of the Gangdese arc (e.g. Zhu *et al.*, 2015) suggests that

720 complete zircon resorption could be common, leaving few tools to recognize the remelting of  
721 older arc rocks and magma hybridization. This is especially true when the arc has a narrow  
722 range of radioactive isotope ratios. Thus, assimilation through remelting of older arc rocks,  
723 followed by hybridization and homogenization (MASH, Hildreth & Moorbath, 1988) could be  
724 widespread with little evidence preserved. In such cases, disentangling magma evolution and the  
725 nature of magma hybridization require detailed field documentation accompanied by  
726 investigation of fine chemical and isotopic zonation of a range of accessories and rock-forming  
727 minerals (e.g. Barnes *et al.*, 2021, Chambers *et al.*, 2020).

## 728 **FUNDING**

729 This research was financially co-supported by the National Natural Science Foundation of China  
730 (42121002 and 91755207), the Second Tibetan Plateau Scientific Expedition and Research  
731 Program (STEP) (2019QZKK0702), and the 111 project (B18048).

## 732 **SUPPLEMENTARY DATA**

733 Supplementary data are available at Journal of Petrology online.

## 734 **Data Availability**

735 The data underlying this article are available in the article and in its online supplementary  
736 material.

## 737 **ACKNOWLEDGEMENTS**

738 We thank Vali Memeti, Calvin Miller and Bill Collins for careful and insightful reviews that  
739 much improved the original manuscript.

## 740 **REFERENCES**

741 Andersen, T. (2002). Correction of common lead in U–Pb analyses that do not report <sup>204</sup>Pb.  
742 *Chemical Geology* **192**, 59-79.

- 743 Barnes, C. G., Werts, K., Memeti, V. & Ardill, K. (2019). Most Granitoid Rocks are Cumulates:  
744 Deductions from Hornblende Compositions and Zircon Saturation. *Journal of Petrology* **60**,  
745 2227-2240.
- 746 Barnes, C. G., Werts, K., Memeti, V., Paterson, S. R. & Bremer, R. (2021). A tale of five enclaves:  
747 Mineral perspectives on origins of mafic enclaves in the Tuolumne Intrusive Complex.  
748 *Geosphere* **17**, 352-374.
- 749 Bell, E. A., Boehnke, P. & Harrison, T. M. (2016). Recovering the primary geochemistry of Jack  
750 Hills zircons through quantitative estimates of chemical alteration. *Geochimica et*  
751 *Cosmochimica Acta* **191**, 187-202.
- 752 Blichert-Toft, J. (2008). The Hf isotopic composition of zircon reference material 91500.  
753 *Chemical Geology* **253**, 252-257.
- 754 Boehnke, P., Watson, E. B., Trail, D., Harrison, T. M. & Schmitt, A. K. (2013). Zircon saturation  
755 re-revisited. *Chemical Geology* **351**, 324-334.
- 756 Bouvier, A., Vervoort, J. D. & Patchett, P. J. (2008). The Lu–Hf and Sm–Nd isotopic composition  
757 of CHUR: Constraints from unequilibrated chondrites and implications for the bulk composition  
758 of terrestrial planets. *Earth and Planetary Science Letters* **273**, 48-57.
- 759 Bruand, E., Fowler, M., Storey, C., Laurent, O., Antoine, C., Guitreau, M., Heilimo, E. & Nebel,  
760 O. (2020). Accessory mineral constraints on crustal evolution: elemental fingerprints for magma  
761 discrimination. *Geochemical Perspectives Letters* **13**, 7-12.
- 762 Chambers, M., Memeti, V., Eddy, M. P. & Schoene, B. (2020). Half a million years of magmatic  
763 history recorded in a K-feldspar megacryst of the Tuolumne Intrusive Complex, California,  
764 USA. *Geology* **48**, 400-404.
- 765 Chu, M.-F., Chung, S.-L., O'Reilly, S. Y., Pearson, N. J., Wu, F.-Y., Li, X.-H., Liu, D., Ji, J., Chu,  
766 C.-H. & Lee, H.-Y. (2011). India's hidden inputs to Tibetan orogeny revealed by Hf isotopes of  
767 Transhimalayan zircons and host rocks. *Earth and Planetary Science Letters* **307**, 479-486.
- 768 Claiborne, L. L., Miller, C. F., Gualda, G. A. R., Carley, T. L., Covey, A. K., Wooden, J. L. &  
769 Fleming, M. A. (2018). Zircon as Magma Monitor. *Microstructural Geochronology*, 1-33.
- 770 Claiborne, L. L., Miller, C. F., Walker, B. A., Wooden, J. L., Mazdab, F. K. & Bea, F. (2006).  
771 Tracking magmatic processes through Zr/Hf ratios in rocks and Hf and Ti zoning in zircons: An  
772 example from the Spirit Mountain batholith, Nevada. *Mineralogical Magazine* **70**, 517-543.
- 773 Claiborne, L. L., Miller, C. F. & Wooden, J. L. (2010). Trace element composition of igneous  
774 zircon: a thermal and compositional record of the accumulation and evolution of a large silicic  
775 batholith, Spirit Mountain, Nevada. *Contributions to Mineralogy and Petrology* **160**, 511-531.
- 776 Clemens, J. D. (2003). S-type granitic magmas—petrogenetic issues, models and evidence. *Earth-*  
777 *Science Reviews* **61**, 1-18.
- 778 Collins, W. J., Huang, H.-Q. & Jiang, X. (2016). Water-fluxed crustal melting produces  
779 Cordilleran batholiths. *Geology* **44**, 143-146.
- 780 Collins, W. J., Murphy, J. B., Johnson, T. E. & Huang, H.-Q. (2020). Critical role of water in the  
781 formation of continental crust. *Nature Geoscience* **13**, 331-338.
- 782 Connolly, J. A. D. (2005). Computation of phase equilibria by linear programming: A tool for  
783 geodynamic modeling and its application to subduction zone decarbonation. *Earth and*  
784 *Planetary Science Letters* **236**, 524-541.
- 785 Connolly, J. A. D. & Petrini, K. (2002). An automated strategy for calculation of phase diagram  
786 sections and retrieval of rock properties as a function of physical conditions. *Journal of*  
787 *Metamorphic Geology* **20**, 697-708.



- 788 Ferry, J. M. & Watson, E. B. (2007). New thermodynamic models and revised calibrations for the  
789 Ti-in-zircon and Zr-in-rutile thermometers. *Contributions to Mineralogy and Petrology* **154**,  
790 429-437.
- 791 Frost, B. R., Barnes, C. G., Collins, W. J., Arculus, R. J., Ellis, D. J. & Frost, C. D. (2001). A  
792 geochemical classification for granitic rocks. *Journal of Petrology* **42**, 2033-2048.
- 793 Fu, B., Page, F. Z., Cavosie, A. J., Fournelle, J., Kita, N. T., Lackey, J. S., Wilde, S. A. & Valley,  
794 J. W. (2008). Ti-in-zircon thermometry: applications and limitations. *Contributions to*  
795 *Mineralogy and Petrology* **156**, 197-215.
- 796 Gagnevin, D., Daly, J. S. & Kronz, A. (2010). Zircon texture and chemical composition as a guide  
797 to magmatic processes and mixing in a granitic environment and coeval volcanic system.  
798 *Contributions to Mineralogy and Petrology* **159**, 579-596.
- 799 Geisler, T., Schaltegger, U. & Tomaschek, F. (2007). Re-equilibration of zircon in aqueous fluids  
800 and melts. *Elements* **3**, 43-50.
- 801 Griffin, W. L., Pearson, N. J., Belousova, E., Jackson, S. E., van Achterbergh, E., O'Reilly, S. Y.  
802 & Shee, S. R. (2000). The Hf isotope composition of cratonic mantle: LAM-MC-ICPMS  
803 analysis of zircon megacrysts in kimberlites. *Geochimica et Cosmochimica Acta* **64**, 133-147.
- 804 Griffin, W. L., Wang, X., Jackson, S. E., Pearson, N. J., O'Reilly, S. Y., Xu, X. & Zhou, X. (2002).  
805 Zircon chemistry and magma mixing, SE China: In-situ analysis of Hf isotopes, Tonglu and  
806 Pingtan igneous complexes. *Lithos* **61**, 237-269.
- 807 Harrison, T. M., Watson, E. B. & Aikman, A. B. (2007). Temperature spectra of zircon  
808 crystallization in plutonic rocks. *Geology* **35**, 635-638.
- 809 Hildreth, W. & Moorbath, S. (1988). Crustal contributions to arc magmatism in the Andes of  
810 Central Chile. *Contributions to Mineralogy and Petrology* **98**, 455-489.
- 811 Holland, T. J. B., Green, E. C. R. & Powell, R. (2018). Melting of Peridotites through to Granites:  
812 A Simple Thermodynamic Model in the System KNCFMASHTOCr. *Journal of Petrology* **59**,  
813 881-900.
- 814 Hoskin, P. W. O. (2005). Trace-element composition of hydrothermal zircon and the alteration of  
815 Hadean zircon from the Jack Hills, Australia. *Geochimica et Cosmochimica Acta* **69**, 637-648.
- 816 Hoskin, P. W. O. & Schaltegger, U. (2003). The Composition of Zircon and Igneous and  
817 Metamorphic Petrogenesis. *Reviews in Mineralogy and Geochemistry* **53**, 27-62.
- 818 Jagoutz, O. & Klein, B. (2018). On the importance of crystallization-differentiation for the  
819 generation of SiO<sub>2</sub>-rich melts and the compositional build-up of arc (and  
820 continental) crust. *American Journal of Science* **318**, 29-63.
- 821 Ji, W.-Q., Wu, F.-Y., Chung, S.-L., Li, J.-X. & Liu, C.-Z. (2009). Zircon U–Pb geochronology and  
822 Hf isotopic constraints on petrogenesis of the Gangdese batholith, southern Tibet. *Chemical*  
823 *Geology* **262**, 229-245.
- 824 Kapp, P. & DeCelles, P. G. (2019). Mesozoic–Cenozoic geological evolution of the Himalayan–  
825 Tibetan orogen and working tectonic hypotheses. *American Journal of Science* **319**, 159-254.
- 826 Kemp, A. I. S., Hawkesworth, C. J., Foster, G. L., Paterson, B. A., Woodhead, J. D., Hergt, J. M.,  
827 Gray, C. M. & Whitehouse, M. J. (2007). Magmatic and Crustal Differentiation History of  
828 Granitic Rocks from Hf–O Isotopes in Zircon. *Science* **315**, 980-983.
- 829 Kirkland, C. L., Yakymchuk, C., Olierook, H. K. H., Hartnady, M. I. H., Gardiner, N. J., Moyen,  
830 J.-F., Hugh Smithies, R., Szilas, K. & Johnson, T. E. (2021). Theoretical versus empirical  
831 secular change in zircon composition. *Earth and Planetary Science Letters* **554**, 116660.
- 832 Laurent, O. (2012). Les changements géodynamiques à la transition Archéen-Protérozoïque : étude  
833 des granitoïdes de la marge Nord du craton du Kaapvaal (Afrique du Sud). PhD thesis  
834 Université Blaise Pascal, Clermont-Ferrand.

- 835 Lee, C.-T. A. & Bachmann, O. (2014). How important is the role of crystal fractionation in making  
836 intermediate magmas? Insights from Zr and P systematics. *Earth and Planetary Science Letters*  
837 **393**, 266-274.
- 838 Liu, Y., Hu, Z., Gao, S., Günther, D., Xu, J., Gao, C. & Chen, H. (2008). In situ analysis of major  
839 and trace elements of anhydrous minerals by LA-ICP-MS without applying an internal standard.  
840 *Chemical Geology* **257**, 34-43.
- 841 Liu, Y., Hu, Z., Zong, K., Gao, C., Gao, S., Xu, J. & Chen, H. (2010). Reappraisal and  
842 refinement of zircon U-Pb isotope and trace element analyses by LA-ICP-MS. *Chinese Science*  
843 *Bulletin* **55**, 1535-1546.
- 844 Ludwig, K. R. (2003). *User's manual for Isoplot 3.00: a geochronological toolkit for Microsoft*  
845 *Excel*. Berkeley.
- 846 Ma, L., Wang, Q., Li, Z.-X., Wyman, D. A., Jiang, Z.-Q., Yang, J.-H., Gou, G.-N. & Guo, H.-F.  
847 (2013). Early Late Cretaceous (ca. 93Ma) norites and hornblendites in the Milin area, eastern  
848 Gangdese: Lithosphere–asthenosphere interaction during slab roll-back and an insight into early  
849 Late Cretaceous (ca. 100–80Ma) magmatic “flare-up” in southern Lhasa (Tibet). *Lithos* **172-**  
850 **173**, 17-30.
- 851 Miller, C. F., McDowell, S. M. & Mapes, R. W. (2003). Hot and cold granites? Implications of  
852 zircon saturation temperatures and preservation of inheritance. *Geology* **31**, 529-532.
- 853 Miller, J. S., Matzel, J. E. P., Miller, C. F., Burgess, S. D. & Miller, R. B. (2007). Zircon growth  
854 and recycling during the assembly of large, composite arc plutons. *Journal of Volcanology and*  
855 *Geothermal Research* **167**, 282-299.
- 856 Morel, M. L. A., Nebel, O., Nebel-Jacobsen, Y. J., Miller, J. S. & Vroon, P. Z. (2008). Hafnium  
857 isotope characterization of the GJ-1 zircon reference material by solution and laser-ablation  
858 MC-ICPMS. *Chemical Geology* **255**, 231-235.
- 859 Moyen, J.-F., Janoušek, V., Laurent, O., Bachmann, O., Jacob, J.-B., Farina, F., Fiannacca, P. &  
860 Villaros, A. (2021). Crustal melting vs. fractionation of basaltic magmas: Part 1, The bipolar  
861 disorder of granite petrogenetic models. *Lithos*, 106291.
- 862 Müntener, O. & Ulmer, P. (2018). Arc crust formation and differentiation constrained by  
863 experimental petrology. *American Journal of Science* **318**, 64-89.
- 864 Paton, C., Hellstrom, J., Paul, B., Woodhead, J. & Hergt, J. (2011). Iolite: Freeware for the  
865 visualisation and processing of mass spectrometric data. *Journal of Analytical Atomic*  
866 *Spectrometry* **26**, 2508-2518.
- 867 Reubi, O. & Blundy, J. (2009). A dearth of intermediate melts at subduction zone volcanoes and  
868 the petrogenesis of arc andesites. *Nature* **461**, 1269-1273.
- 869 Rubatto, D. & Hermann, J. (2007). Experimental zircon/melt and zircon/garnet trace element  
870 partitioning and implications for the geochronology of crustal rocks. *Chemical Geology* **241**, 38-  
871 61.
- 872 Schiller, D. & Finger, F. (2019). Application of Ti-in-zircon thermometry to granite studies:  
873 problems and possible solutions. *Contributions to Mineralogy and Petrology* **174**, 51.
- 874 Shand, S. J. (1943). *Eruptive Rocks: Their Genesis, Composition, Classification, and Their*  
875 *Relation to Ore-Deposits with a Chapter on Meteorite*. New York: John Wiley & Sons.
- 876 Siégel, C., Bryan, S. E., Allen, C. M. & Gust, D. A. (2018). Use and abuse of zircon-based  
877 thermometers: A critical review and a recommended approach to identify antecrystic zircons.  
878 *Earth-Science Reviews* **176**, 87-116.
- 879 Sláma, J., Košler, J., Condon, D. J., Crowley, J. L., Gerdes, A., Hanchar, J. M., Horstwood, M. S.  
880 A., Morris, G. A., Nasdala, L., Norberg, N., Schaltegger, U., Schoene, B., Tubrett, M. N. &  
881 Whitehouse, M. J. (2008). Plešovice zircon — A new natural reference material for U–Pb and  
882 Hf isotopic microanalysis. *Chemical Geology* **249**, 1-35.

- 883 Söderlund, U., Patchett, P. J., Vervoort, J. D. & Isachsen, C. E. (2004). The  $^{176}\text{Lu}$  decay constant  
884 determined by Lu–Hf and U–Pb isotope systematics of Precambrian mafic intrusions. *Earth and*  
885 *Planetary Science Letters* **219**, 311-324.
- 886 Sun, S.-s. & McDonough, W. F. (1989). Chemical and isotopic systematics of oceanic basalts:  
887 implications for mantle composition and processes. *Geological Society, London, Special*  
888 *Publications* **42**, 313-345.
- 889 Symington, N. J., Weinberg, R. F., Hasalová, P., Wolfram, L. C., Raveggi, M. & Armstrong, R. A.  
890 (2014). Multiple intrusions and remelting-remobilization events in a magmatic arc: The St. Peter  
891 Suite, South Australia. *Bulletin of the Geological Society of America* **126**, 1200-1218.
- 892 Troch, J., Ellis, B. S., Schmitt, A. K., Bouvier, A.-S. & Bachmann, O. (2018). The dark side of  
893 zircon: textural, age, oxygen isotopic and trace element evidence of fluid saturation in the  
894 subvolcanic reservoir of the Island Park-Mount Jackson Rhyolite, Yellowstone (USA).  
895 *Contributions to Mineralogy and Petrology* **173**, 54.
- 896 Wang, R., Richards, J. P., Hou, Z.-q., An, F. & Creaser, R. A. (2015). Zircon U–Pb age and Sr–  
897 Nd–Hf–O isotope geochemistry of the Paleocene–Eocene igneous rocks in western Gangdese:  
898 Evidence for the timing of Neo-Tethyan slab breakoff. *Lithos* **224-225**, 179-194.
- 899 Wang, R., Weinberg, R. F., Collins, W. J., Richards, J. P. & Zhu, D.-c. (2018). Origin of  
900 postcollisional magmas and formation of porphyry Cu deposits in southern Tibet. *Earth-Science*  
901 *Reviews* **181**, 122-143.
- 902 Watson, E. B. & Harrison, T. M. (1983). Zircon saturation revisited: temperature and composition  
903 effects in a variety of crustal magma types. *Earth and Planetary Science Letters* **64**, 295-304.
- 904 Watson, E. B., Wark, D. A. & Thomas, J. B. (2006). Crystallization thermometers for zircon and  
905 rutile. *Contributions to Mineralogy and Petrology* **151**, 413.
- 906 Weinberg, R. F. & Dunlap, W. J. (2000a). Growth and deformation of the Ladakh batholith,  
907 northwest Himalayas: Implications for timing of continental collision and origin of calc-alkaline  
908 batholiths. *Journal of Geology* **108**, 303-320.
- 909 Weinberg, R. F. & Dunlap, W. J. (2000b). Growth and Deformation of the Ladakh Batholith,  
910 Northwest Himalayas: Implications for Timing of Continental Collision and Origin of  
911 Calc-Alkaline Batholiths. *Journal of Geology* **108**, 303-320.
- 912 Weinberg, R. F., Vernon, R. & Schmelling, H. (2021). Granitic mushes: their role in magma  
913 mixing and assimilation of solids with special focus on enclaves. *Earth-Science Reviews* **220**,  
914 103665.
- 915 White, L. T., Ahmad, T., Ireland, T. R., Lister, G. S. & Forster, M. A. (2011). Deconvolving  
916 episodic age spectra from zircons of the Ladakh Batholith, northwest Indian Himalaya.  
917 *Chemical Geology* **289**, 179-196.
- 918 Xu, W., Zhu, D.-C., Wang, Q., Weinberg, R. F., Wang, R., Li, S.-M., Zhang, L.-L. & Zhao, Z.-D.  
919 (2021). Cumulate mush hybridization by melt invasion: Evidence from compositionally-diverse  
920 amphiboles in ultramafic-mafic arc cumulates within the eastern Gangdese Batholith, southern  
921 Tibet. *Journal of Petrology* **61**, ega073.
- 922 Yin, A. & Harrison, T. M. (2000). Geologic evolution of the Himalayan-Tibetan orogen. *Annual*  
923 *Review of Earth and Planetary Sciences*, 211-280.
- 924 Zhang, L.-L., Zhu, D.-C., Wang, Q., Zhao, Z.-D., Liu, D. & Xie, J.-C. (2019). Late Cretaceous  
925 volcanic rocks in the Sangri area, southern Lhasa Terrane, Tibet: Evidence for oceanic ridge  
926 subduction. *Lithos* **326-327**, 144-157.
- 927 Zhang, Z., Ding, H., Palin, R. M., Dong, X., Tian, Z. & Chen, Y. (2020). The lower crust of the  
928 Gangdese magmatic arc, southern Tibet, implication for the growth of continental crust.  
929 *Gondwana Research* **77**, 136-146.

- 930 Zhang, Z., Zhao, G., Santosh, M., Wang, J., Dong, X. & Shen, K. (2010). Late Cretaceous  
931 charnockite with adakitic affinities from the Gangdese batholith, southeastern Tibet: Evidence  
932 for Neo-Tethyan mid-ocean ridge subduction? *Gondwana Research* **17**, 615-631.
- 933 Zhu, D.-C., Wang, Q., Chung, S.-L., Cawood, P. A. & Zhao, Z.-D. (2019). Gangdese magmatism  
934 in southern Tibet and India–Asia convergence since 120 Ma. *Geological Society, London,*  
935 *Special Publications* **483**, 583-604.
- 936 Zhu, D.-C., Wang, Q., Weinberg, R. F., Cawood, P. A., Chung, S.-L., Zheng, Y.-F., Zhao, Z.,  
937 Hou, Z.-Q. & Mo, X.-X. (2022). Interplay between oceanic subduction and continental collision  
938 in building continental crust. *Nature Communications* **13**, 7141.
- 939 Zhu, D.-C., Wang, Q., Zhao, Z.-D., Chung, S.-L., Cawood, P. A., Niu, Y., Liu, S.-A., Wu, F.-Y. &  
940 Mo, X.-X. (2015). Magmatic record of India-Asia collision. *Scientific Reports* **5**, 14289.
- 941 Zhu, D.-C., Zhao, Z.-D., Niu, Y., Mo, X.-X., Chung, S.-L., Hou, Z.-Q., Wang, L.-Q. & Wu, F.-Y.  
942 (2011). The Lhasa Terrane: Record of a microcontinent and its histories of drift and growth.  
943 *Earth and Planetary Science Letters* **301**, 241-255.
- 944

945 **Figure Captions**

946 Fig. 1. a) Geological map of the Gangdese Batholith linking to the Ladakh Batholith in the west.  
 947 Small rectangle in the east shows the location of (b). Inset shows the location of (a). b)  
 948 Geological map of the area surrounding the village of Dabu and the dykes investigated here.  
 949 BNSZ refers to the Bangong-Nujiang Suture Zone, SNMZ to the Shiquanhe–Nam Tso Mélange  
 950 Zone, LMF to Luobadui-Milashan Fault, IYZSZ to the Indus-Yarlung Tsangpo Suture Zone,  
 951 and MBT refers to the Main Boundary Thrust.

952 Fig. 2. Field relationships. a) Diorite dykes cutting through tonalite close to Dabu village. All  
 953 samples and photographs are from this location. Small black ellipse on lower left indicates a  
 954 small van for scale. Rectangle on right-hand side marks the position of (b). b) Tip of dykes with  
 955 variable width and orientation. Vertical scale is ~3m. (c) irregular boundary between dyke and  
 956 tonalite with back-veining of a finer granitic rock. d) Irregularities at the contact at cm-scale. e)  
 957 and f) Heterogeneous diorite with irregular veins with sharp to diffuse margins linked to  
 958 irregular patches with gradational contact with the diorite. These are interpreted to record the  
 959 nature of mingling and mixing of between granitic and dioritic magmas.

960 Fig. 3. Major element features of the studied samples (Frost *et al.*, 2001). a) FeO/(FeO+MgO) vs  
 961 SiO<sub>2</sub> showing the boundary between ferroan and magnesian plutonic rocks; b) SiO<sub>2</sub>–MALI  
 962 (wt.%) binary diagram (MALI = Modified alkali-lime index, Na<sub>2</sub>O+K<sub>2</sub>O–CaO) from Frost *et al.*  
 963 (2001); (c) ASI vs. A/NK diagram [atomic Al/(Ca+Na+K) vs. Al/(Na+K)] (Shand, 1943). Tonalites  
 964 and diorites are magnesian, calc-alkalic and metaluminous to weakly peraluminous.

965 Fig. 4. MORB-normalized (Sun & McDonough, 1989) trace element patterns for the studied  
 966 samples.

967 Fig. 5. Photomicrographs of diorite samples. a) Sample 18DB01-2 showing euhedral to  
 968 subhedral biotite in brown tones and hornblende in green tones. Notice apatite needles in  
 969 plagioclase dominated areas (transparent) (ppl); b) sample 8DB01-2 showing biotite in an  
 970 equant matrix of twinned plagioclase. Note labelled epidote inclusion in biotite (xpl); c) sample  
 971 17DB01-2 (ppl); d) sample 18DB01-4 showing anhedral hornblende and subhedral biotite  
 972 surrounding aggregates of plagioclase (transparent) (ppl). Apatite and epidote grains are  
 973 indicated. Note absence of pleochroic haloes in biotite in all photomicrographs.

974 Fig. 6. Zircon CL images. Diorite samples 17DB01-2 (a) and 18DB01-2 (b). Zircons have  
 975 roughly rectangular shapes with two parallel rational faces and two irregular sides. They are  
 976 generally dark, but some are grey or bright, with either no zoning, irregular zoning or wide

977 bands. The two samples have contrasting zircon sizes. c) Tonalite sample 18DB01-3 showing  
 978 representative grains similar to the other two tonalite samples. Zircons are euhedral, bright with  
 979 well-developed, continuous oscillatory zoning. Some rare grains show a quenched region  
 980 overprinting the early-formed zoning (left-side of bottom grain). d) Diorite sample 18DB01-4  
 981 with two distinct zircon morphological groups: a small group of euhedral zircons labelled  
 982 xenocrysts, similar to those from the tonalite in (c), and a larger group similar to those from the  
 983 diorites in (a) and (b). The xenocrysts have ages that coincide with those of the tonalite samples.  
 984 Green, red and black dashed circles indicate position of analytical spot and colour indicates  
 985 origin of the zircon: diorite, tonalite and xenocryst in diorite, respectively. Numbers indicate U-  
 986 Pb age obtained. The scale in (a) applies to all images.

987 Fig. 7. a) REE plot normalized to chondrite (Sun & McDonough, 1989). Zircons from the  
 988 tonalitic host define similar patterns to the xenocrysts in the diorite sample 18DB01-4, both  
 989 dated at between 70 and 80 Ma (see Fig. 11d). Diorite zircon autocrysts have higher values than  
 990 the tonalite zircons and show a wide variation in LREE values (six orders of magnitude for La)  
 991 reflecting alteration effects (e.g. Bell *et al.*, 2016). b) Yb/Dy vs Eu/Eu\* showing trace element  
 992 similarity between the xenocryst zircons in diorite and tonalite autocrysts.

993 Fig. 8. Zircon trace element versus the Light Rare Earth Element Index [ $LREE-I = (Dy/Nd +$   
 994  $Dy/Sm)$ ] (a proxy for zircon alteration Bell *et al.*, 2016) and U content. Diorite zircon analyses  
 995 are divided into two groups based on CL: types 1-2 clean grey sections of grains and types 3-4  
 996 regions dominated by metamictization and CL quenching; see Supplementary Data Electronic  
 997 Appendix 2). There is considerable overlap between the two groups but types 3-4 have  
 998 systematically lower LREE-1 and higher contents of all trace elements. In (a) and (b) Fe and Ti  
 999 define negative trends with LREE-1 (in these figures, types 3-4 symbols were placed in front of  
 1000 types 1-2 for better visualization of the link between zircons deemed altered and LREE-1 values.  
 1001 Types 3-4 zircon analyses concentrate, as expected, in the lower end of LREE-1, indicative of  
 1002 alteration, but reach values of 100, considerably higher than the cutoff value of 30 for alteration  
 1003 of Bell *et al.* (2016). Up to 100, types 3-4 overlap with types 1-2, and these can have very high  
 1004 contents of Ti. In (c) to (h), Fe, Ca, Th, Y reach values close to 10,000 ppm or 1 wt.%, defining  
 1005 positive trends with U, which reaches up to 9000 ppm. Titanium also defines a positive trend  
 1006 with U, with numerous analyses above 30 ppm, some reaching a few 100 ppm. The trend  
 1007 defined by Hf and Ti in diorite zircons are the opposite to those found for granitic rocks by  
 1008 Claiborne *et al.* (2010) shown by the grey fields, and similar to the high-U zircons in Fig. 6 in  
 1009 Troch *et al.* (2018). In (c) to (h), types 3-4 zircon symbols were placed behind types 1-2. For

1010 tonalite zircons, the trends are similar to those in Claiborne et al. (2010). Tonalite zircons and  
1011 xenocrysts in diorite sample 18DB01-4 are not differentiated and overlap in the plots. All plots  
1012 are log-log scale.

1013 Fig. 9. (a-d) Binary plots of typically incompatible elements versus Ti in zircon. For tonalite  
1014 samples Hf behaves incompatibly defining negative, but all other elements define a curved  
1015 shape changing from a positive (compatible) to a negative (incompatible) trend as Ti increases.  
1016 This is not the case for the diorite sample for which U, Th, and Yb, define only positive or  
1017 compatible trends with Ti, and only Hf defines a negative (incompatible) trend. The compatible  
1018 trends are surprising and contrast with the incompatible trends found by Claiborne et al (2010)  
1019 indicated by grey fields. Ti-values higher than 40 ppm were not plotted as they correspond to  
1020 unrealistically high T and therefore probably correspond to altered zircons. Grey empty symbols  
1021 indicate analyses with anomalous peaks or plateaus of Fe and Ca, key indicators of  
1022 metamictization and zircon re-equilibration (see section 9.2 for discussion). All plots are log-log  
1023 scale and symbols are as in legend for Fig. 8.

1024 Fig. 10. Concordia diagrams for zircon analyses from diorite samples. a-c) Diorite dyke  
1025 samples 17DB01-2, 18DB01-2 and 18DB01-4 with ages centred around 46 to 47 Ma. Samples  
1026 18DB01-2 and 18DB01-4 also contained 70-80 Ma xenocrysts shown in Fig. 11. d) Comparison  
1027 between ages of zircon analyses from diorite sample 18DB01-4 as a function of CL type shows  
1028 no systematic shift between CL types 1-2, and the quenched CL types 3-4 despite the  
1029 anomalously high values of Th+U and other trace elements in the latter (Fig. 8). All ellipses in  
1030 (a-c) and bars in (d) mark the  $2\sigma$  confidence level. A number of analyses have been excluded: 2  
1031 of 74 analyses for 17DB01-2 (1 with large error, 1 with fluctuating age signals), 18 out of 75 for  
1032 18DB01-2 (16 discordant and 2 outliers), 25 out of 111 for 18DB01-4 (23 discordant, 1 outlier  
1033 and 1 with large error). A small number of outlier dates were removed from the calculation of  
1034 the mean age by Isoplot: 2 out of 72 for sample 17DB01-2, 2 out of 57 for sample 18DB01-2, 4  
1035 out of 86 for sample 18DB01-4. In (d), analyses in light grey at the high-end of values, have  
1036 been dates removed from the calculation of the mean age.

1037 Fig. 11. Concordia diagrams for zircon analyses from tonalite samples and xenocrysts in diorite  
1038 samples. a-c) Tonalite samples 17DB01-1, 18DB01-1, 18DB01-3 showing ages centred between  
1039 77 and 79 Ma and lacking older xenocrysts. d) and e) Xenocrysts from diorite dyke sample  
1040 18DB01-4 and 18DB01-2. The spread of dates in (d) and (e) imply that the mean ages are not  
1041 meaningful with  $MSWD > 10$ . All ellipses mark the  $2\sigma$  confidence level. A small number of  
1042 analyses have been excluded from the diagrams: 1 of 18 analyses for sample 17DB01-1 ( $>10\%$

1043 discordant), 5 of 68 for 18DB01-1 (2 discordant and 3 outlier), and 3 of 19 for 18DB01-4 (2  
1044 with very large errors and 1 outlier). A small number of outliers were removed from the  
1045 calculation of the mean age by Isoplot: 4 out of 63 for sample 18DB01-1, and 2 out of 18 for  
1046 sample 18DB01-3.

1047 Fig. 12.  $^{206}\text{Pb}/^{238}\text{U}$  ages for zircons from diorites show no systematic trend with Th+U content.  
1048 Symbols as in legend for Fig. 8 where empty symbols are types 3-4.

1049 Fig. 13.  $\epsilon_{\text{Hf}(t)}$  values for all six samples plotted against zircon U-Pb age. The ~77-79 Ma tonalite  
1050 zircons have  $\epsilon_{\text{Hf}(t)}$  centred around  $+9 \pm 1$ , whereas the ~46-47 Ma diorite analyses are more  
1051 spread between +6 and +11. N=344 analyses, with 78 from tonalite zircons and 266 from  
1052 diorite.

1053 Fig. 14. Model of crystallization for a diorite melt with 73 ppm Zr and a tonalite melt with 144  
1054 ppm Zr. H<sub>2</sub>O contents for the diorite of 3 wt.% H<sub>2</sub>O (left column), and 6 wt.% H<sub>2</sub>O (middle  
1055 column) are shown. Tonalite melt contains 2 wt.% H<sub>2</sub>O. Low H<sub>2</sub>O content was assumed in order  
1056 to investigate its remelting by H<sub>2</sub>O derived from the diorite intrusion. a) Minerals and melt/H<sub>2</sub>O  
1057 proportions. Diorite solidus T ( $T_{\text{sol}}$ ) is 677 °C, and 650 °C for the tonalite. The two diorite  
1058 models show nearly 70 °C difference water saturation T. Sphene, spinel and ilmenite form in  
1059 diorite and tonalite not shown because of low proportions. b) Melt fraction. For all three cases  
1060 the last ~20% crystallizes within 10 °C of the solidus. c) Zr content in melt. Values increase  
1061 until the curve intersects the zircon saturation curves calculated using M-values in (d) and  
1062 calibrations in Boehnke et al. (2013) and Watson and Harrison (1983). Zircon saturation for the  
1063 diorites is reached at 714 and 711 °C, for 3 and 6 wt.% H<sub>2</sub>O, respectively, where ~23% melt (for  
1064 3% H<sub>2</sub>O) or ~ 26% melt (for 6% H<sub>2</sub>O) remain. Tonalite reaches ~ 20% melt at ~650 °C solidus,  
1065 where ~ 90% of the zircons are stable. d) M-value of residual melt used to determine the zircon  
1066 saturation curve in (c). M-value for diorites steadily decrease to reach a value of 1.4 close to the  
1067 solidus. For the tonalite M first decreases from a value of 1.45 at the liquidus (not shown) and  
1068 then increases to ~1.4 at the solidus, due to stabilization of Bt and Qtz. e)  $a(\text{SiO}_2)$  and  $a(\text{TiO}_2)$ . f)  
1069 Ti-in-zircon calculated using curves in (e) (solid lines) or assuming a fixed value of  $a(\text{SiO}_2)=1$   
1070 and  $a(\text{TiO}_2)=0.7$  (dashed lines; similar to Claiborne et al. (2010)). The differences between the  
1071 two curves are small. Calculations use Ferry and Watson (2007). g) Zr content in melt, non-  
1072 zircon phases and zircon as a function of temperature (note different scale in x-axis). Zircons are  
1073 saturated close to the solidus for diorite. Diorite composition is similar to the basalt modelled by



1074 Lee and Bachmann (2014) (their Fig. 2b), but despite higher Zr in our starting composition, melt  
1075 never reaches the > 300 ppm Zr in their model, peaking instead at ~ 150 ppm, due to significant  
1076 intake of Zr in non-zircon minerals excluded in their model.

1077 Fig. 15. Comparison of signal outputs from zircon analyses for sample 18DB01-4: a) spot 1-04  
1078 in a type 1 zircon, and b) spot 2-41 in a type 2 zircon. Data from (b) was excluded from  
1079 consideration because of anomalous plateaus of Fe, Ca, Ti, and a sudden drop in Th, U counts.

1080 Fig. 16. Zircon chemistry modelling. a) Modelled zircon Th vs Ti composition for the diorite  
1081 and tonalite (thick black lines) compared with data for zircons from diorite dykes, xenocrystic  
1082 zircons in diorite and tonalite host rock zircons; b) same for Nd vs Ti. Analysed zircon grains  
1083 are colour coded according to “reliability”: if the zircon analysis has anomalous Fe or Ca signal  
1084 it is deemed unreliable, if it has anomalous peaks or plateaus of Y, Th, Ti or HREE it is deemed  
1085 dubious, otherwise it is classified as magmatic. Models are calculated as discussed in the text  
1086 and uses Boehnke et al.’s (2013) model for saturation, but the results are very similar using  
1087 Watson & Harrison (1983). For comparison (a) shows the approximate slope of the trend (thick  
1088 grey arrow) defined by the data for granitic rocks in Claiborne et al. (2006), which is similar to  
1089 the modelled slope for the tonalite (thick dashed line). The yellow band in (b) defines the field  
1090 generated by mixing a zircon composition with 3 ppm Ti and 1 ppm Nd, with titanite with  
1091 24.4 % Ti and between 1000 and 10000 ppm Nd (Bruand *et al.*, 2020). The band indicates that  
1092 mixing with titanite is unlikely to explain the trend because it causes a stronger enrichment in Ti  
1093 compared to Nd.

1094 Fig. 17. Assimilation of host rock through anatexis, back-veining and mixing with zircon  
1095 transfer. a) Original dioritic magma intrusion at temperatures above zircon saturation. As  
1096 magma flows and cools, it heats-up the surrounding and releases H<sub>2</sub>O. b) The tonalite melts at  
1097 relatively low temperatures lacking anhydrous peritectic minerals. Granitic dykelets derived  
1098 from tonalite anatexis back-veins the diorite that is now a cool zircon-saturated mush. The mush  
1099 deforms in a ductile fashion and granitic melt flow through the pore space of the mush (inset)  
1100 transferring tonalite zircons and hybridizing the diorite. Zircon xenocrysts are preserved in the  
1101 zircon-saturated diorite. Size of zircons is exaggerated.

1 **Using zircons to disentangle back-veining and hybridization of**  
2 **diorite dykes : an example from the Gangdese Arc, Tibet**

3 Roberto F. Weinberg<sup>1\*</sup>, Jean-François Moyen<sup>2</sup>, Jian-Kang Yi<sup>3</sup>, Di-Cheng Zhu<sup>3</sup>,  
4 Oliver Nebel<sup>1</sup>, Shaorong Chen<sup>3</sup>, Qiang Wang<sup>3</sup>

5 <sup>1</sup>School of Earth, Atmosphere and Environment, Monash University, Clayton, VIC, 3800,  
6 Australia.

7 <sup>2</sup> Université de Lyon, Laboratoire Magmas et Volcans, UJM-UCA-CNRS-IRD,  
8 23 rue Dr. Paul Michelon, 42023 Saint Etienne, France

9 <sup>3</sup> State Key Laboratory of Geological Processes and Mineral Resources, China University of  
10 Geosciences, Beijing 100083, China

11 \*Corresponding author Telephone: +61 3 9905 4902. Fax: +61 3 9905 4903. E-mail:  
12 Roberto.weinberg@monash.edu

13

14

15 **ABSTRACT**

16 Thermo-chemical modelling and chemical data suggest that the genesis of arc melts commonly  
17 involves re-melting of older intrusions, triggered by the injection of mantle-derived melts,  
18 followed by magma mixing. Remelting and mixing may lead to complex zircon populations,  
19 which can be used to gain insights into the conditions of mixing. This paper investigates a case  
20 where such processes can be studied through the compositional and thermal record provided by  
21 zircons preserved in a diorite dyke swarm that remelted host rock tonalites in the Gangdese  
22 Batholith in Tibet. Autocrystic zircons from the diorite yield consistent ages of 46-47 Ma even  
23 though they can be altered, with having highly enriched ~~in~~-trace elements, reaching ~1 wt% in  
24 Fe, Ca, Y, U, Th, and anomalously high values of LREE and Ti. Granitic magmas derived from  
25 the tonalite, back-veined the dykes and mixed with the dioritic mush, transferring small  
26 quantities of 77-79 Ma zircon xenocrysts. The xenocrysts are euhedral with little evidence for  
27 resorption, indicating they were apparently stable during the process of tonalite anatexis and  
28 transfer to the diorite magma. This requires that: (i) tonalite melting occurred at low  
29 temperatures with minimal zircon dissolution, and (ii) the diorite either cooled rapidly before  
30 significant resorption of the grains or was already saturated in zircon when mixing occurred.  
31 Zircon saturation temperatures of the diorite are relatively low, indicating that xenocrystic  
32 zircons were transferred to a highly crystalline dioritic mush. This requires either liquefaction by  
33 injection of the back-veining felsic magma to allow for mixing or pervasive throughflow of the  
34 diorite mush by the felsic magma leaving behind zircon xenocrysts. The findings suggest that  
35 the dykes triggered low-T, water-fluxed melting of the host tonalite, and that these anatectic  
36 melts invaded the diorite mush initially through the interstices leading to mixing and this may  
37 have caused the breakdown of the crystalline framework leading to liquefaction and renewed  
38 magma flow. Dyking and assimilation of wall-rock through back-veining as recorded in these  
39 rocks could be common in transcrustal arcs. However, this process could be hidden due to a

40 combination of the similarity in the isotopic and chemical nature of arc rocks, and resorption of  
41 zircon xenocrysts during mixing. This process may explain some complex chemistry of arc  
42 magmatic rocks and their minerals that are not easily explained by endmember models, such as  
43 pure re-melting of older arc rocks or fractional crystallization of mantle-derived melts.

44 **Key words:** geothermometry; magma hybridization; magma mingling; zircon; zircon saturation  
45 temperature

## 46 INTRODUCTION

47 The origin of granitic magmas in arcs is at the center of a long-standing debate focused on  
48 whether they are derived from the fractionation of basaltic magmas (Jagoutz & Klein, 2018,  
49 Müntener & Ulmer, 2018), or the remelting of older arc intrusions (Collins *et al.*, 2020, Moyen  
50 *et al.*, 2021, Symington *et al.*, 2014, Weinberg & Dunlap, 2000b) or magma mixing (Reubi &  
51 Blundy, 2009). In this regard, evidence for zircon recycling through the system as xenocrysts  
52 and antecrysts, combined with Ti-in-zircon thermometry and zircon saturation temperatures, can  
53 be used to explore and constrain the processes controlling arc magma evolution, such as whether  
54 mixing or assimilation processes were involved and when and how they occurred. The term  
55 xenocryst refers here to zircon incorporated from the surrounding host rocks during magma  
56 transit and emplacement, whereas the term antecrysts refers to zircon formed in an earlier pulse  
57 of magma and that was transferred to the current host. The term autocryst refers to zircon  
58 crystallized from the host magma (Miller *et al.*, 2007).

59 Zircon has a number of properties that makes it useful in constraining magmatic processes. It is  
60 an excellent marker of the time of magma crystallization, and its trace elements indicate  
61 contemporaneous crystallization or dissolution of other minerals (Rubatto & Hermann, 2007).  
62 Its Hf isotopic composition is a sensitive indicator of melt sources and mixing between magmas  
63 from different sources (Kemp *et al.*, 2007), and in the case of xenocrystic zircon, Hf isotopic

64 ratio can be used to determine its source. Further to that, Ti-in-zircon thermometry (Watson *et*  
65 *al.*, 2006), in combination with zircon saturation temperatures of magma (Boehnke *et al.*, 2013,  
66 Watson & Harrison, 1983), constrain magma crystallization histories (Schiller & Finger, 2019)  
67 and the conditions prevalent during fractionation and mixing (Barnes *et al.*, 2019, Harrison *et*  
68 *al.*, 2007, Miller *et al.*, 2003, Miller *et al.*, 2007, Siégel *et al.*, 2018). These data can then be  
69 linked to modeling of the chemical evolution of melt and crystals during crystallization to define  
70 zircon saturation temperature and the expected Ti-content of zircons (Barnes *et al.*, 2019, Lee &  
71 Bachmann, 2014).

72 There is often a mismatch between temperatures derived from Ti-in-zircon and from zircon  
73 saturation. In samples with many zircon xenocrysts, this mismatch can be caused by the added  
74 Zr. In samples with few or no xenocrysts, the mismatch can be caused either by fractional  
75 crystallization that changes the Zr content and composition of the interstitial melt, or by changes  
76 in the total Zr content through accumulation of zircons and other minerals, or through loss of Zr-  
77 rich interstitial melt (Barnes *et al.*, 2019). Zircon saturation temperatures unaccompanied by  
78 modeling of fractional crystallization ~~has~~have been used to suggest that arc granites typically  
79 record relatively low zircon saturation temperatures, and to postulate that granitic arc magmas  
80 are typically cold (<800 °C), derived from water-fluxed re-melting of older arc rocks (Collins *et*  
81 *al.*, 2016, Collins *et al.*, 2020). However, zircon saturation temperature is strongly dependent on  
82 the initial Zr content of the magma and the evolution of the residual melt composition during  
83 crystallization (Miller *et al.*, 2003).

84 In this paper, we explore the nature of zircon autocrysts in diorite dykes and the fate of zircon  
85 xenocrysts transferred from the host rock as a result of anatexis of the host rock, back-veining  
86 and mixing, in an outcrop in the Gangdese Batholith in Tibet (Zhu *et al.*, 2015). We use zircon  
87 U-Pb ages and grain morphology, combined with zircon saturation temperatures and Ti-in-  
88 zircon thermometry to constrain the thermal conditions and magma crystallinity during mixing.

89 The discussion is underpinned by compositional modelling of a crystallizing melt and the trace  
90 element composition of zircons in the evolving melt.

91 The paper starts with a brief description of the Gangdese Batholith and field relationships  
92 between the diorite dykes and host rocks investigated here, including the back-veining and  
93 hybridization of the dykes caused by melting of the host. The methodology is then described,  
94 followed by characterization of the tonalite and diorite samples and their zircons, including U-  
95 Pb dating, Hf-isotope and trace element composition. Whole-rock chemistry is used as the basis  
96 for modeling diorite magma crystallization and determining zircon saturation temperatures, as  
97 well as to model tonalite melting occurring as the diorite cooled. Modelled zircon saturation  
98 temperatures and zircon trace element compositions are also derived from these models and  
99 form the basis for discussion of the timing of magma mixing and xenocryst transfer, and the  
100 validity of Ti-in-zircon thermometry for these zircons. Results show how these approaches  
101 combined can be used to cast light on both the physical details of hybridization, and to  
102 exemplify some of the pitfalls associated with interpreting the data.

## 103 **GANGDESE BATHOLITH AND DABU GEOLOGY**

104 The Gangdese Batholith (Fig. 1) and its western continuation in NW India and Pakistan, the  
105 Ladakh and Kohistan Batholiths, is a 2500 km-long calc-alkaline magmatic arc that extends  
106 across the southern Tibetan Plateau. It is an Andean-type continental arc formed as a result of  
107 oceanic subduction of the Neo-Tethys oceanic lithosphere under the Lhasa Terrane at the Asian  
108 continental margin until collision with India at  $55 \pm 5$  Ma shut down the arc (Ji *et al.*, 2009, Yin  
109 & Harrison, 2000, Zhu *et al.*, 2019). Magmatism started at  $\sim 210$  Ma and continued  
110 intermittently until collision ended typical subduction-related magmatism and initiated post-  
111 collisional magmatism. Subduction-related magmatism is marked by two intense pulses of  
112 magmatic activity, one at  $90 \pm 5$  Ma and the other at 55-50 Ma (Zhu *et al.*, 2019). The  $90 \pm 5$

113 Ma event is linked with ridge subduction (Zhang *et al.*, 2010) or slab rollback (Ma *et al.*, 2013)  
114 of the Neo-Tethyan oceanic lithosphere, whereas the 55-50 Ma event is attributed to collision  
115 followed by slab breakoff (Zhu *et al.*, 2019) or lithosphere removal (Kapp & DeCelles, 2019).  
116 The dykes investigated here belong to the syn-collisional event, which was the most intensive  
117 magmatic pulse in the Gangdese belt (Zhu *et al.*, 2019), and includes the voluminous Linzizong  
118 volcanic successions (Zhu *et al.*, 2015). Oligocene-Miocene post-collisional magmatism was  
119 dominated by silicic rocks resulting from the remelting of arc magmatic rocks and their  
120 hybridization with metasomatized lithospheric mantle-derived ultrapotassic melts (e.g. Wang *et*  
121 *al.*, 2018).

122 Magmatic rocks from the  $90 \pm 5$  Ma events show coherent “depleted mantle-like” zircon  $\epsilon_{\text{Hf}}(t)$   
123 (+15 to +10) and positive whole-rock  $\epsilon_{\text{Nd}}(t)$  (around +3.0) with a few outliers (Ji *et al.*, 2009,  
124 Ma *et al.*, 2013, Zhang *et al.*, 2020, Zhu *et al.*, 2011) that may reflect varying degrees of  
125 incorporation of ancient crustal components from the Gangdese basement into the juvenile  
126 magmas. Rocks related to the  $55 \pm 5$  Ma event are characterized by a wide range in zircon  $\epsilon_{\text{Hf}}(t)$   
127 (between -6 and +15)(Zhu *et al.*, 2022) and whole-rock  $\epsilon_{\text{Nd}}$  (mostly from +5.0 to -3.0). This  
128 more evolved isotopic signature has generally been attributed to the involvement of Indian  
129 continent-derived materials (Chu *et al.*, 2011, Wang *et al.*, 2015).

130 Rocks of the Gangdese arc only rarely have zircon xenocrysts (Zhu *et al.*, 2015). To our  
131 knowledge no xenocrysts have been reported in syn-collisional plutonic rocks in this arc and  
132 only a few have been reported for the Linzizong volcanic rocks (a few xenocrysts formed at ~90  
133 Ma and older, Zhu *et al.*, 2015). This contrasts with rocks from the Ladakh Batholith, the  
134 western continuation of the Gangdese Batholith, which show migmatization and where zircons  
135 define a ca. 20 Ma age range (Weinberg & Dunlap, 2000a, White *et al.*, 2011) including  
136 recycling of 68 Ma zircons in a 49 Ma magma. Despite this exception, the general rarity of  
137 zircon xenocrysts could indicate that: a) remelting of older arc intrusions is a minor process

138 (Jagoutz & Klein, 2018), b) because zircons are rare in mafic arc rocks, few or no zircons are  
139 passed on to the felsic magmas they produce upon remelting, or c) zircon xenocrysts are  
140 resorbed during relatively high-temperature melting (Miller *et al.*, 2003).

141 This paper focuses on an outcrop of the Gangdese Batholith along the road from Zedong to  
142 Nyingchi (Fig. 1a) at N29.2625° and E92.4119° close to Dabu village. Here, a diorite dike  
143 swarm (Fig. 2a, b) intrudes a homogeneous leucocratic tonalite and is back-veined by magmas  
144 resulting from the melting of the tonalite host. The dykes are typically 1-3 m wide and are  
145 continuous for more than 100 m. In detail, the dyke contacts are irregular at the dm-cm scale,  
146 and back-veined (Fig. 2c, d) and dyke tips narrow considerably over a few metres. At the  
147 contact, the tonalite has a centimetric layer of more felsic and finer-grained granitic rock that is  
148 continuous with dykelets intruding the diorite (Fig. 2c). These dykelets are irregular and intrude  
149 and gradually vanish into a heterogeneous diorite (Fig. 2e, f). We have determined whole-rock  
150 chemistry and investigated zircons from three samples of diorite and three samples of tonalite  
151 host rock, all homogeneous at hand-specimen scale.

## 152 **METHODOLOGY**

### 153 **Whole-rock geochemical analysis**

154 Fresh rocks samples were crushed, hand-picked, and then powdered using an agate mill to  
155 a grain size < 200 mesh at the Yuneng Mineral Separation Service Company at Langfang, Hebei  
156 Province, China. Major element analyses of whole rock were conducted on Agilent 7700e ICP-  
157 MS at the Wuhan SampleSolution Analytical Technology Co., Ltd., Wuhan, China. The sample  
158 pre-treatment of whole rock major element analysis was made by melting method. The detailed  
159 sample-digesting procedure was as follows: (1) Sample powder (200 mesh) ~~were was~~ placed in  
160 an oven at 105 °C for drying of 12 hours; (2) ~1.0g dried sample was accurately weighed and  
161 placed in the ceramic crucible and then heated in a muffle furnace at 1000°C for 2 hours. After



162 cooling to 400°C, this sample was placed in the drying vessel and weighted again in order to  
163 calculate the loss-on-ignition (LOI); (3) 0.6 g sample powder was mixed with 6.0 g flux and 0.3  
164 g oxidant (NH<sub>4</sub>NO<sub>3</sub>) in a Pt crucible, which was placed in the furnace at 1050°C for 15 minutes.  
165 The flux is a mixture of lithium tetraborate, lithium metaborate and lithium fluoride (45:10:5).  
166 Then, this ~~melting-molten~~ sample was quenched in air for 1 minute to produce flat discs on the  
167 fire brick for the XRF analyses.

168 Zsx Primus II wavelength dispersive X-ray fluorescence spectrometer (XRF) produced by  
169 RIGAKU, Japan, was used for the analysis of major elements in the whole rock, The X-ray tube  
170 is a 4.0Kw end window Rh target. The ~~analytical test~~ conditions ~~are-were~~ voltage: 50kV,  
171 current: 60mA. All major element analysis lines are ~~keKα~~. The standard curve uses the national  
172 standard material of China, rock standard sample: GBW07101-14. The data were corrected by  
173 ~~the~~ theoretical  $\alpha$  coefficient method. The relative standard deviation (RSD) is less than 2% ~~and~~  
174 ~~the average bias of the measurements was of -0.1% for SiO<sub>2</sub> and has its highest values of + 1.3%~~  
175 ~~for MgO and -1.6% for P<sub>2</sub>O<sub>5</sub>.~~

176 Trace element analyses of whole rock were conducted on Agilent 7700e ICP-MS at the Wuhan  
177 SampleSolution Analytical Technology Co., Ltd., Wuhan, China. Four rock reference materials  
178 (AGV-2, BHVO-2, BCR-2, and RGM-2) were used to calibrate the contents of trace elements of  
179 analytical samples. The detailed sample-digesting procedure was as follows: (1) Sample powder  
180 (200 mesh) was placed in an oven at 105 °C for drying of 12 hours; (2) 50 mg sample powder  
181 was accurately weighed and placed in a Teflon bomb; (3) 1 ml HNO<sub>3</sub> and 1 ml HF were slowly  
182 added into the Teflon bomb; (4) Teflon bomb was ~~putted~~ in a stainless steel pressure jacket and  
183 heated to 190 °C in an oven for >24 hours; (5) after cooling, the Teflon bomb was opened and  
184 placed on a hotplate at 140 °C and evaporated to incipient dryness, and then 1 ml HNO<sub>3</sub> was  
185 added and evaporated to dryness again; (6) 1 ml of HNO<sub>3</sub>, 1 ml of MQ water and 1 ml internal  
186 standard solution of 1ppm In were added, and the Teflon bomb was resealed and placed in the

187 oven at 190 °C for >12 hours; (7) the final solution was transferred to a polyethylene bottle and  
188 diluted to 100 g by the addition of 2% HNO<sub>3</sub>.

### 189 **LA-ICP-MS zircon U-Pb dating and trace element analysis**

190 Zircons were separated using conventional and magnetic techniques at the Yuneng Mineral  
191 Separation Service Company at Langfang, Hebei Province, China. Cathodoluminescence (CL)  
192 images, obtained at the Institute of Geology, Chinese Academy of Geological Sciences  
193 (Beijing), were used to check the internal textures of single zircons and to select suitable  
194 positions for U-Pb dating and Hf isotope analysis. The zircon U-Pb isotope and trace element  
195 analyses were carried out using LA-ICP-MS at the Mineral Laser Microprobe Analysis  
196 Laboratory (Milma Lab), China University of Geosciences (Beijing). Detailed analytical  
197 procedure was described by Zhang et al. (2019) and provided in Supplementary Data Electronic  
198 Appendix 1 (all the Electronic Appendices may be downloaded from  
199 <http://www.petrology.oupjournals.org/>). A beam diameter of 35 µm was used for the first round  
200 of analyses, whereas for the second round 35 µm was only used for sample 17DB01-2 used and  
201 25 µm for the remainder, which was also used for the third round. Zircon 91500 was used as an  
202 external standard for correcting U-Pb dating, and glass NIST 610 was used as an external  
203 standard for trace element calibration. Off-line analyses were performed using an Excel-based  
204 software ICPMSDataCal (Liu *et al.*, 2008, Liu *et al.*, 2010). Uncertainties in trace element  
205 measurements are between 5 and 10%. Common Pb correction was calculated using the  
206 program ComPbCorr#3.17 (Andersen, 2002). Concordia diagrams and mean calculations were  
207 made using ISOPLOT (v. 3.0) (Ludwig, 2003). Samples were analysed during three sessions,  
208 but they gave similar results (Supplementary Data Electronic Appendix 2) and so we present  
209 merged results.

## 210 Zircon Hf isotopic analysis

211 Zircon Hf isotopic analyses were conducted in the same domain of the grain as for U-Pb  
212 analyses, as defined by CL images. Analyses used a Neptune Plus MC-ICP-MS (~~Thermal~~  
213 Thermo Fisher Scientific, Germany), coupled to a New Wave 193 excimer ArF laser-ablation  
214 system at the Milma Lab, China University of Geosciences (Beijing) with a beam size of 35  $\mu\text{m}$ ,  
215 laser pulse frequency of 8 Hz and energy density of 3.7 J/cm<sup>2</sup>. Makeup gas of argon and carrier  
216 gas of helium with the addition of nitrogen mixed in a T-branch pipe prior to introduction into  
217 the MC-ICP-MS. In the experiment, L4 to H3 Faraday cups were used to collect <sup>171</sup>Yb, <sup>173</sup>Yb,  
218 <sup>175</sup>Lu, <sup>176</sup>Hf, <sup>177</sup>Hf, <sup>178</sup>Hf, <sup>179</sup>Hf, and <sup>180</sup>Hf, respectively with the integration time of 0.131 s. The  
219 carrier and makeup gas flows were optimized by a line scan (spot size of 35  $\mu\text{m}$  and scan speed  
220 of 5  $\mu\text{m/s}$ ) ablating NIST SRM 610 to obtain maximum signal intensity for <sup>232</sup>Th, while  
221 minimizing <sup>232</sup>Th<sup>16</sup>O/<sup>232</sup>Th ratio. For each analysis, 50 s integration for gas blank and 50 s  
222 integration for signal collection were set up with a total of 800 cycles of raw data. Zircon 91500  
223 (Blichert-Toft, 2008) was used as an external standard for correcting mass discrimination.  
224 Zircon standard Plešovice (Sláma *et al.*, 2008) and GJ-1 (Morel *et al.*, 2008) were analyzed as  
225 unknown sample that were inserted between zircon 91500 and the samples. Raw data was  
226 converted by Neptune Plus software and then processed using Iolite software (Paton *et al.*,  
227 2011).

228 The initial <sup>176</sup>Hf/<sup>177</sup>Hf ratios and  $\epsilon_{\text{Hf}}(t)$  values were calculated with ~~the~~ reference to the  
229 chondritic reservoir (CHUR) at the time of zircon growth from the magmas. The decay constant  
230 for <sup>176</sup>Lu of  $1.867 \times 10^{-11}$  year<sup>-1</sup> (Söderlund *et al.*, 2004), the chondritic <sup>176</sup>Hf/<sup>177</sup>Hf ratio of  
231 0.282785 and <sup>176</sup>Lu/<sup>177</sup>Hf ratio of 0.0336 (Bouvier *et al.*, 2008) were adopted. Depleted mantle  
232 model ages ( $T_{\text{DM}}$ ) were calculated with reference to the depleted mantle at a present-day  
233 <sup>176</sup>Hf/<sup>177</sup>Hf ratio of 0.28325, and <sup>176</sup>Lu/<sup>177</sup>Hf = 0.0384 (Griffin *et al.*, 2000). The Hf isotope  
234 crustal model age ( $T_{\text{DM}}^{\text{C}}$ ) was calculated by assuming that its parental magma was derived from

235 an average continental crust, with  $^{176}\text{Lu}/^{177}\text{Hf} = 0.015$ , that originated from the depleted mantle  
236 source (Griffin *et al.*, 2002).

## 237 **SAMPLES: GEOCHEMISTRY AND PETROGRAPHY**

238 Six samples were investigated: three diorites and three tonalites (see Supplementary Data  
239 Electronic Appendix 3 for photographs of the sampling location; coordinates N29.263 and  
240 E92.4112). All diorite samples are homogeneous dark grey, and tonalite samples are white to  
241 light grey. Whole-rock chemistry in Table 1 shows that the diorites are of intermediate  
242 composition ( $53 < \text{SiO}_2 < 58$  wt.%) and the tonalites felsic ( $\text{SiO}_2 = 68\text{-}69$  wt.%). The rocks have  
243  $\text{K}_2\text{O}/\text{Na}_2\text{O} < 1$ , and both rock types are magnesian and calc-alkalic, based on Frost *et al.* (2001)  
244 descriptors, ~~both rock types are magnesian and calc-alkalic~~ (Fig. 3). The diorites are  
245 metaluminous, and the tonalites weakly peraluminous (ASI 1.00 to 1.05) (Fig. 3). Trace  
246 elements for both rock types are similar, with negative anomalies ~~in-of~~ Nb ~~and Ta~~ and positive  
247 anomalies ~~in-of~~ Pb and Sr in MORB-normalized diagrams (Fig. 4, Ta also defines a negative  
248 anomaly, not shown). HREE exhibit low values of 0.1 – 1 times MORB values, and are lower in  
249 the tonalites than in the diorites. All samples have Zr/Hf between 35.6 and 40.7, and La/Yb (not  
250 normalized) between 7 and 31 for the tonalite and 6 to 13 for the diorite. Although the two rock  
251 types were emplaced some 30 Myr apart (see section 7 below), they display very similar  
252 geochemical properties, consistent with their arc setting.

253 The diorite dykes are fine-grained and massive, and are composed of plagioclase (~70%-75%),  
254 biotite (~15%-20%), amphibole (~10%-15%) and quartz (~5%-10%). Plagioclase is zoned with  
255 lamellar twinning and the grains are forming subhedral to euhedral ~~grains~~, 100 to 400  $\mu\text{m}$  long,  
256 some reaching 1 mm in length, tending towards subequant grains, with crystal faces in some  
257 places forming mosaics with  $120^\circ$  intersection between grains. Amphibole is twinned, anhedral  
258 to subhedral, with green to brown pleochroism and 50-1500  $\mu\text{m}$  long (generally 100-200  $\mu\text{m}$ ). In

259 sample 18DB01-4, the longer Hbl grains include biotite grains. Biotite is subhedral to euhedral,  
260 with light-brown to dark-brown pleochroism, forming isolated grains with rectangular sections  
261 100-1000  $\mu\text{m}$  long (generally 300-400  $\mu\text{m}$ ), or forming aggregates with hornblende. The  
262 accessory minerals are apatite, zircon, epidote and opaque minerals, and sample 17DB01-2 has  
263 titanite. Diorite zircon grains have inclusions and cavities and typically appear in the felsic  
264 matrix rather than as inclusions in the mafic minerals, which lack pleochroic haloes. The nature  
265 of the zircon grains is described in the next subsection. Apatite forms needles reaching 300-400  
266  $\mu\text{m}$ , occasionally 600  $\mu\text{m}$ , mostly in the felsic matrix, but can be found included in hornblende  
267 and biotite. Epidote grains can be either included in biotite as subhedral grains, possibly  
268 primary, or in the felsic matrix where it could be a result of alteration of plagioclase. The  
269 tonalite is medium grained (grain-size: 1 to 2 mm), lacking a foliation and is composed of  
270 plagioclase (~60%-70%), quartz (~20%-30%), biotite (~5%-8%), minor K-feldspar, and with  
271 apatite, zircon among the felsic minerals, and Fe-Ti oxides as accessory phases. Samples  
272 18DB01-3 and 18DB01-1 also have titanite. Plagioclase occurs mainly as subhedral to euhedral  
273 laths. Biotite is anhedral to subhedral and displays yellowish to dark-brown pleochroism.

## 274 **ZIRCON CATHODOLUMINESCENCE**

275 Zircons from the tonalite typically vary in size from 150 to 250  $\mu\text{m}$  (ranging from 100 to 400  
276  $\mu\text{m}$ ) and are bipyramidal prismatic with well-developed, fine oscillatory zoning (Fig. 6), or  
277 common sector zoning, with some internal truncation of early zonation. Zircons from the diorite  
278 vary in size from 100 to 400  $\mu\text{m}$  and the majority of grains have roughly rectangular shapes  
279 defined by two parallel rationale faces, forming the longer sides of the rectangle, and two  
280 shorter, irregular sides. Some grains have a pyramidal ending. Samples 18DB01-4 and 18DB01-  
281 2 have a second morphological type of zircon comprising euhedral grains, with well-developed,  
282 fine prismatic oscillatory and sector zoning, similar to zircons from the tonalites (compare  
283 grains in Fig. 6c and xenocrysts in Fig. 6d). The latter are considered xenocrysts and comprise

284 7% of the population (11 grains out a total 162 in the mount for sample 18DB01-4). From this  
285 we estimate that they add only ~ 5 ppm Zr to the 74 ppm content of the whole rock for this  
286 sample. Sample 18DB01-2 has an even smaller proportion of these xenocrystic zircons. We  
287 neglect this added amount when considering zircon saturation temperatures below.

288 CL images of zircons from the diorite define three distinct zircon groups (excluding the  
289 xenocrysts in samples 18DB01-4 and 18DB01-2): a) clean and grey grains; b) grains with  
290 considerable clean, grey parts and with metamict domains with cauliflower-like pattern and  
291 partly quenched to black CL; and c) fully metamict grains with or without very thin grey rims  
292 (Fig. 6) that are either entirely or mostly quenched, preserving weak cauliflower-like patterns in  
293 very dark regions. Based on these distinctions, the spots were divided into 4 types depending on  
294 their position: Type 1 are from clean and grey areas in grains from group (a); Type 2 are spots  
295 from the clean, grey part of grains from group (b), and Type 3 are from the metamict part of the  
296 same grains; and Type 4 are spots from fully metamict, quenched grains of group (c). Types 3  
297 and 4 are commonly associated with anomalous zircon trace element compositions as we will  
298 see in the next subsection.

## 299 **ZIRCON GEOCHEMISTRY**

300 Zircons from the tonalite host rock and xenocrysts from diorites have similar trace element  
301 composition, with U and Th contents below 2100 and 1800 ppm, respectively, similar REE  
302 patterns (Fig. 7, Supplementary Data Electronic Appendix 2), and Ti contents between 1 and 10  
303 ppm (Supplementary Data Electronic Appendix 2). These values contrast starkly with the  
304 autocrysts from the diorite that show higher abundances of REE (Fig. 7) and anomalously high  
305 values of U-Th-Ca-Fe-Y, each with values approaching or surpassing 1 wt.% (Fig. 8) (for more  
306 zircons with high trace element contents see Gagnevin *et al.*, 2010). Their Ti contents are  
307 between 1 and >500 ppm (15 out 260 analyses yielded Ti > 30 ppm) (Fig. 8d).

308 Hafnium is an incompatible element during crystallization of felsic magmas (Claiborne *et al.*,  
309 2010), with a bulk partition coefficient remaining below one even during zircon crystallization,  
310 despite zircon's high Hf uptake. Conversely, titanium, is a compatible element that enters mafic  
311 silicates and common accessories, such as Fe-Ti oxides and titanite. Thus, during magma  
312 crystallization, Hf increases while Ti decreases in the melt leading to the negative trend of Hf  
313 against Ti in Fig. 9. The same is not true for U, Th and Yb, which show unexpected positive  
314 trends against Ti, for diorite zircons, indicative of an apparently compatible behaviour of these  
315 elements during crystallization (Fig. 9), contrasting with the incompatible trends in Claiborne *et*  
316 *al.* (2010).

### 317 **ZIRCON U-Pb AGES AND Hf ISOTOPES**

318 The three tonalite and three diorite rock samples in Table 1 were dated. The diorite samples  
319 yielded ages of 46-47 Ma and the tonalite samples yielded ages of 77-79 Ma and (Figs. 10 and  
320 11). Given the close mean ages for the diorite samples and their relatively large spread,  
321 indicated by high MSWDs (>4), we consider that the dykes were essentially contemporaneous.  
322 Zircons with CL types 3 and 4 with quenched, metamictic CL features, tend to be richer in U,  
323 Th and other trace elements compared to types 1 and 2 (Fig. 8). In order to determine if types 3  
324 and 4 have been affected by Pb-loss, U-Pb dates were compared with those for CL types 1 and 2  
325 (Figs. 10d and 12). Results show no significant differences and dates vary from ~44 to 51 Ma  
326 independently of CL type. We have therefore considered all concordant U-Pb analyses.

327 Two tonalite samples have ages that overlap within error at ~79 Ma and have small MSWD  
328 (Fig. 11a,c). The third sample, however, has a slightly younger mean age at  $77.2 \pm 0.5$  Ma and a  
329 high MSWD=4.8 (Fig. 11b). This sample has three times more analyses than the other two,  
330 suggesting that the tonalites may have a large true spread in dates. Two of the three diorite  
331 samples (Fig. 11d-e) have xenocrysts with the same range of dates and same trace element

332 chemistry as the tonalite zircons (Fig. 7) confirming the interpretation based on CL images (Fig.  
333 6). Analyses with >10% discordancy as well as a small number of outliers were not considered  
334 here.

335 Hafnium isotopes for subpopulations of the dated zircons from all 6 samples were obtained.  
336 They are typical of those of the Gangdese arc yielding  $\epsilon_{\text{Hf}(t)}$  between +4 and +13 (Fig. 13;  
337 *Supplementary Data Electronic Appendix 2*). The values for the tonalites are similar to those of  
338 the diorite with the exception that the latter have a wider variation (+4 to +13 compared to +6 to  
339 +10). Xenocrysts of diorite sample 18DB01-4 plot together with the tonalite zircons.

## 340 **CHEMICAL MODELLING OF MELT EVOLUTION AND ZIRCON**

### 341 **CRYSTALLIZATION**

#### 342 **Methods**

343 The crystallization of zircons during cooling of magmas has been modelled using a procedure  
344 similar to the ones described by Schiller and Finger (2019) (see also Harrison *et al.*, 2007,  
345 Kirkland *et al.*, 2021). In a cooling closed system, magma crystallizes and the residual melt  
346 evolves chemically. Zr is initially incompatible and its content increases until zircon becomes  
347 saturated at which point it becomes compatible and starts decreasing in the melt upon further  
348 fractionation. Thus, zircon crystallizes out of this residual melt, whose composition evolves and  
349 differs from the composition of the bulk rock. In a closed-system, the melting process upon  
350 heating follows the opposite direction to the one described above.

351 In our models, we first calculate the closed-system evolution of the rock using phase equilibria,  
352 and in particular the amount and composition of the residual melt at a given temperature. Zr is  
353 partitioned between melt and solids using known partition coefficients, and the Zr content in the  
354 melt is compared with the zircon saturation value; any Zr above the saturation value at this point



355 is then used to form zircon. Other trace elements are then partitioned between liquid and all  
356 solids, zircon included. The most important assumptions in this process are that the composition  
357 of the diorite and tonalite correspond to melt compositions, and that this is a closed system  
358 behaviour, i.e. we assume batch rather than fractional crystallization (or indeed batch melting, as  
359 both are exactly similar in a closed system): neither melt nor crystals are removed from the  
360 system, and the system properties are calculated independently for each point.

361 The details of the procedure are given in Supplementary Data Electronic Appendix 5. Phase  
362 equilibrium is modelled using PerpleX version 6.9.0 (Connolly, 2005, Connolly & Pettrini,  
363 2002) and the minerals and melt models by Holland et al. (2018), that allow incorporation of  
364 Fe<sup>3+</sup> and Ti, using one-dimensional T profiles at a fixed P of 5 kbar. Zircon saturation values are  
365 based on the saturation model of Boehnke et al. (2013) and results for the model of Watson and  
366 Harrison (1983) are also shown for comparison. These models include a dependence on the melt  
367 composition expressed as the parameter M, the cation ratio (Na + K + 2Ca)/(Al x Si), which is  
368 obtained from the phase equilibrium model. Partition coefficient values for trace elements vary  
369 considerably in the literature. We use those compiled by Laurent (2012), using values for felsic  
370 rocks (SiO<sub>2</sub> > 63 %), which are appropriate for both rock types since the residual melt, even in  
371 the diorite, is almost always at these values. For Th, U, HFSE and REE, the zircon-melt  
372 partition coefficients are modified using the temperature parametrization of Claiborne et al.  
373 (2018). Temperature-dependent coefficients for other minerals are unavailable and have the  
374 potential to modify our results. Finally, we calculated Ti contents in zircon as a function of  
375 temperature using the model of Ferry and Watson (2007). As their equation relies on the activity  
376 of Si and Ti, both were calculated from the phase equilibrium model (following Schiller &  
377 Finger, 2019). PerpleX outputs chemical potentials that must be converted into activities.

378 Given the pressure dependence of ~5 °C/kb for the Ti-in-zircon thermometer determined by  
379 Ferry and Watson (2007), our calculated temperatures could be overestimates for the lower

380 pressure used here (5 kb) compared to the 10 kb used in Ferry and Watson's calibration. All  
381 parameters are calculated along the 1D temperature profile used for phase equilibrium,  
382 simulating closed-system cooling (or heating) of the magma or the rock. After the phase  
383 equilibrium modelling, all steps are performed using a homemade R script (available from J-F  
384 Moyen on request).

### 385 **Evolution of melt and zircon**

386 Crystallization of a melt in a closed system is modelled using diorite sample 18DB01-4, the  
387 most mafic of the diorites with 54% SiO<sub>2</sub> and 73 ppm Zr. We carried out two calculations, with  
388 3 and 6 % H<sub>2</sub>O. A value close to the average of the tonalite samples was used with SiO<sub>2</sub> =  
389 68.3 % and 140 ppm Zr (Table 1). A low H<sub>2</sub>O content of 2 wt.% was assumed for modelling the  
390 tonalite in order to investigate its remelting triggered by limited quantities of H<sub>2</sub>O delivered  
391 from the diorite intrusion.

392 In the model, the diorite crystallizes Amp-Pl-Cpx accompanied later by Bt that increases in  
393 proportion towards the end of the crystallization history, with quartz appearing close to the  
394 solidus temperature ( $T_{\text{sol}}=677$  °C; Fig. 14a). Water saturation is reached at 687 °C, close to the  
395 solidus for the case with 3 wt.% H<sub>2</sub>O, and at 754 °C for 6 wt.% H<sub>2</sub>O, nearly 80 °C above the  
396 solidus. The tonalite crystallizes Pl+Opx at high temperature and at ~800 °C, Opx reacts to Bt.  
397 Kfs appears relatively late in the history and H<sub>2</sub>O becomes saturated a few degrees above the  
398 solidus ( $T_{\text{sol}}= 650$  °C). The evolution of the melt fraction for all calculations is depicted in Fig.  
399 14b.

400 The Zr content in the melt increases with crystallization until the melt reaches zircon saturation  
401 (Fig. 14c). After this point the melt follows the zircon saturation curve controlled primarily by  
402 temperature and secondarily by melt composition, expressed by its M-value that evolves as

403 crystallization proceeds (Fig. 14d). The temperature of zircon saturation for the diorite with 73  
404 ppm Zr in the melt at the start is 714 or 711 °C using Boehnke et al.'s (2013) calibration, and is  
405 only weakly sensitive to the H<sub>2</sub>O content, corresponding to melt fractions of 23 to 26 %,  
406 respectively. The saturation temperature is ~ 30 - 40 °C higher when using the calibration of  
407 Watson and Harrison (1983) corresponding to melt fractions of 26 to 35 wt.%. For the case with  
408 6 wt.% H<sub>2</sub>O, zircon saturation is reached at temperatures lower than H<sub>2</sub>O saturation. The tonalite  
409 initially with 140 ppm Zr and 2 wt.% H<sub>2</sub>O reaches zircon saturation at 805 °C and 41% melt  
410 (Boehnke *et al.*, 2013), while H<sub>2</sub>O becomes saturated a few degrees before the solidus at 650 °C.  
411 Thus, zircon saturation temperature of the tonalite is ~ 150 °C above the solidus and 100 °C  
412 higher than that of the diorite due to its lower M-values and higher Zr content (140 ppm vs 73  
413 ppm).

414 For the diorite models, crystallization leads to a gradual decrease in the M value of the melt  
415 fraction from close to 2.2 at the liquidus, to a minimum of 1.4 at the solidus (Fig. 14d). The  
416 tonalite is different. M values vary only weakly, first decreasing from M=1.45 at the liquidus  
417 (not shown) to 1.32 at the start of crystallization of quartz and biotite at which point M increases  
418 gently reaching 1.40 at the solidus, similar to the residual melt in the diorite close to its solidus.  
419 The  $a(\text{SiO}_2)$  and  $a(\text{TiO}_2)$  in Fig. 14e were used to calculate the expected value of Ti-in-zircon.  
420 Despite considerable variation in activities during crystallization, the calculated Ti-in-zircon  
421 curves are similar to those calculated using fixed value of  $a(\text{SiO}_2) = 1$  and  $a(\text{TiO}_2) = 0.7$  (compare  
422 continuous and dashed lines in Fig. 14f). Thus, these values are a good approximation of the  
423 behaviour of the metaluminous magmas (see discussion in Schiller & Finger, 2019).

424 Modelling results indicate that prior to zircon saturation in the dioritic magma, most Zr is hosted  
425 in the melt with some going initially into hornblende and biotite as magma cools. At zircon  
426 saturation, nearly half the Zr is hosted by these other minerals (Fig. 14g) but as the proportion of  
427 zircon increases, ~~they~~ these non-zircon minerals lose Zr record a decrease in the total Zr content  
428 that they host. At the solidus, a little over 20 ppm is hosted by non-zircon minerals, and the  
429 remaining ~50 ppm is hosted by zircon, corresponding to a (modal) proportion of just under  
430 0.01 % zircon. During tonalite crystallization, few minerals take in Zr, so nearly all of the ~140  
431 ppm is hosted in zircon, corresponding to about 0.03 modal % in the rock.

432 The decrease in Zr content hosted by non-zircon minerals is a result of the modeling calculations  
433 considering the whole-rock chemical composition and distributing the available elements  
434 according to the mineral proportions stable at the new temperature. This means that minerals  
435 and melt are in equilibrium at all times during cooling. After zircon becomes saturated, the Zr  
436 content in the melt decreases as temperature decreases so that the amount of Zr that goes into the  
437 non-zircon minerals decreases according to the partition coefficient, kept constant. In a real  
438 system, complete equilibrium at all times during cooling may not occur. In this case, some Zr  
439 may be trapped in early-formed minerals, in disequilibrium with the cooling melt. The net effect  
440 would be slightly less zircon being formed than in the calculations presented.

## 441 **DISCUSSION**

### 442 **Ages and source of xenocrysts**

443 Field evidence in Fig. 2 indicates that tonalite remelted at the contact with the diorite and back-  
444 veined the dykes, causing hybridization that is recorded by felsic dykelets and irregular diffuse  
445 leucocratic patches in the diorite. Melting of the tonalite is inferred to be at relatively low  
446 temperatures in the presence of aqueous fluids because of the leucocratic nature of the tonalites

447 with little biotite available and no anhydrous peritectic phase such as garnet or orthopyroxene  
448 associated with anatexis.

449 The 46-47 Ma age of the diorite dykes places them amongst the syn-collisional, compositionally  
450 diverse magmatic flare-up recorded in the southern Lhasa terrane centred around  $\sim 50 \pm 5$  Ma  
451 (Zhu *et al.*, 2019). These rocks typically have a wide range of  $\epsilon_{\text{Hf}(t)}$  varying between -6 and +15  
452 (Fig. 4 in Zhu *et al.*, 2022). The tonalite age of 77-79 Ma with  $\epsilon_{\text{Hf}(t)} = +9 \pm 1$  makes it part of  
453 the pre-collisional magmatism that had  $\epsilon_{\text{Hf}(t)}$  values between +4 and +15.

454 Two out of three diorite samples have older zircon xenocrysts (sample 18DB01-4 and 18DB01-  
455 2) that comprise  $\leq 7\%$  of the grains imaged for each diorite sample. These xenocrysts are likely  
456 derived from the tonalite host rock as they have the same distinctive euhedral prismatic shape  
457 and internal CL zonation (Fig. 6), similar  $\epsilon_{\text{Hf}(t)}$  values (Fig. 13), the same range of U-Pb dates  
458 from  $\sim 80$  Ma to 69 Ma (Fig. 11) and similar trace element composition (Fig. 7).

#### 459 **Anomalous zircon composition**

460 Figures 8 and 9 indicate that the diorite zircons have anomalous trace element composition.  
461 They have very high trace elements contents, such as U-Th-HREE-Y-Ti, and low values of  
462 LREE index (LREE-I, Bell *et al.*, 2016). The elements U, Th and Y define positive trends with  
463 Ti. Given that Ti is expected to decrease in zircon during cooling and melt fractionation, the  
464 trends suggest that these elements behave compatibly during crystallization, contrary to  
465 expectations (Claiborne *et al.*, 2010). Hf is incompatible in the melt defining a negative trend  
466 against Ti, as expected, but unexpectedly it also defines a negative trend against U due to its  
467 compatible behaviour. The high contents of trace elements indicate that self-irradiated,  
468 damaged diorite zircons may have been altered as a result of reaction with melts or fluids

469 (Geisler *et al.*, 2007, Hoskin, 2005, Hoskin & Schaltegger, 2003). For example, the values of Ti  
470 in some analyses are above 30 ppm, reaching up to a few hundred ppm, and these are generally  
471 accompanied by high concentration of other trace elements (Fig. 8).

472 Metamict and quenched zircon types 3 and 4 (Fig. 6) tend to have high concentration of trace  
473 elements (Ca, Fe, REE, U and Th) in contrast to zircon types 1 and 2 (Fig. 8). Despite these  
474 differences, they all yield similar U-Pb dates with no systematic change that could be ascribed to  
475 Pb-loss (Figs. 10d and 12). In order to determine the extent of alteration, we investigated the  
476 relationships between CL types (Fig. 6) and trace element chemistry for each analytical spot,  
477 considering signal counts of each analysis during data acquisition using the ICPMSDataCal  
478 software. The main findings are that spots with anomalously high trace element abundances  
479 typically have one or more of these features:

- 480 a) high Th+U contents (>3000 ppm) commonly but not always located in zones of  
481 quenched CL. We note however, that there are quenched areas with low Th+U contents  
482 (<1000 ppm) indicating that quenching may be related to other factors;
- 483 b) anomalous values of LREE, expressed by low values of LREE-I (Fig. 8a,b);
- 484 c) anomalous signal plateaus of Fe in CL quenched areas, commonly accompanied by other  
485 anomalous signal plateaus for Ca, Ti, LREE, Th and Y (Fig. 15), probably a result of  
486 inclusions or domains affected by self-irradiation damage and reaction between zircon  
487 and fluid or melt (Geisler *et al.*, 2007);
- 488 d) located in zircon sectors characterized by CL types 3 and 4.

489 We found that taking any of these indicators separately is an insufficient predictor of the spot  
490 having a number of chemical anomalies. The strongest predictor of zircons having several such  
491 anomalies is having anomalous peaks or plateaus in the count curves, in particular for Fe and  
492 Ca. Therefore, we used anomalous peaks or plateaus of Fe and Ca as key indicators of

493 metamictization and re-equilibration (Geisler *et al.*, 2007) and exclude these analyses from  
494 consideration in Ti-in-zircon thermometry. While in most cases, analyses with anomalies of Fe  
495 and Ca generally have at least one other feature in the list above, there is a very small number of  
496 analyses that have no other indicator of alteration. These were also removed. We have checked  
497 the remainder of the data for Ti count anomalies, and found only four analyses with minor Ti  
498 anomalous peaks or plateaus. These lacked Fe or Ca anomaly and were therefore evaluated with  
499 the rest of the results in the next section.

500 Uranium, Th and HREE normally behave incompatibly during crystallization and are expected  
501 to define a negative trend when plotted against Ti contents (Claiborne *et al.*, 2010). However,  
502 these elements in diorite zircons behave compatibly defining a positive trend instead (Fig. 9). In  
503 order to further evaluate this behaviour, we have compared the observed data with modelled  
504 zircon composition. For both tonalite and diorite, zircon composition is scattered, and modelled  
505 composition evolution reproduces them poorly (Fig. 16). The analytical results define a  
506 positively correlated array, at high angle to the negative trend of the model calculations or the  
507 trend defined by the zircons of Claiborne *et al.* (2010) (grey field in Fig. 16). This means that the  
508 processes controlling zircon trace element intake in the diorite is unaccounted for by our  
509 calculations and used assumptions.

### 510 **Ti-in-zircon thermometry**

511 In this section, only zircons that passed the culling described above, deemed as potentially  
512 unaltered, were considered. As we have seen in section 8, converting Ti contents to temperatures  
513 requires assumptions regarding  $\text{TiO}_2$  and  $\text{SiO}_2$  activities. Figure 14f compares two results, one  
514 using “conventional” estimates of  $a(\text{SiO}_2) = 1$  and  $a(\text{TiO}_2) = 0.7$ , and the other using the  
515 calculated activities at each point during crystallization (Fig. 14e). The difference between the  
516 two is small.

517 *Zircons from tonalites*

518 Analyses of 122 spots from the three tonalite samples and xenocrysts from the diorite, yielded a  
519 range in Ti contents from 1.2 to 9.2 ppm (1.2 to 8.5 ppm for the xenocrysts), with a very similar  
520 mean (3.3 ppm for the tonalites, 4.0 ppm for the xenocrysts). These values yield temperatures  
521 (using ideal activities) from 577 to 786 °C. Uncertainties for Ti values between 1-2 ppm are  
522 between 20-30%, decreasing to below 10% for values >5 ppm, with a detection limit of ~0.5  
523 ppm. While the low-T end of the range likely reflects sub-solidus resetting, the high-T end is  
524 lower than but comparable to the zircon saturation temperatures estimated at between 800 and  
525 820 °C (depending on the model used, Fig. 14c).

526 *Zircons from diorites*

527 The Ti-in-zircon values of diorite autocrysts are less well-behaved. Zircons from  
528 sample 18DB01-4 have Ti contents between 1.4 and 17.7 ppm, which translates to temperatures  
529 between 613 and 895 °C (using  $a(\text{SiO}_2) = 1$ ,  $a(\text{TiO}_2) = 0.7$ ), or 614 and 842 °C (using activities  
530 from our model). Since our models also predict the onset of zircon crystallization at low  
531 temperatures (710 - 750 °C depending on the model chosen, Fig. 14c), this is a significant  
532 mismatch, and these “hot” zircons cannot be simply related to zircon saturation temperature  
533 estimates.

534 Similarly, for sample 17DB01-2, Ti ranges between 1.3 and 16.3 ppm (equivalent to a  
535 maximum T of 832 °C), with a mean of 7.9 ppm. Sample 18DB01-2 (with higher Zr = 102 ppm  
536 and hence a higher value of the zircon saturation temperature) has Ti contents between 1.5 and



537 23.3 ppm (equivalent to a maximum T of 915 °C), and a mean of 7.1 ppm. Thus, in all cases the  
538 maximum Ti-in-zircon temperatures are more than 100 °C above the estimated zircon saturation  
539 temperature, when the diorite still had ~40-55% melt fraction depending on the H<sub>2</sub>O content. In  
540 all cases, the calculated temperatures for the lowest Ti grains are up to 50 °C below the solidus.  
541 As our model relies on zircon saturation in melt, we cannot model subsolidus resetting of Ti  
542 composition (discussed in Fu *et al.*, 2008).

#### 543 *Modelling zircon crystallization*

544 While the tonalite zircons yield Ti-in-zircon temperatures that cover the expected range derived  
545 from the calculations, the diorite zircons do not. For these, the maximum Ti-in-zircon  
546 temperatures surpass substantially the modelled zircon saturation temperature in common with  
547 findings elsewhere (Barnes *et al.*, 2019, Claiborne *et al.*, 2006, Harrison *et al.*, 2007).

548 There are two ways of calculating the zircon saturation temperatures. One approach uses the  
549 whole-rock composition as an estimate of the magma composition. It assumes that zircon would  
550 crystallize from a liquid whose composition equates that of the rock, for which a high M value  
551 results in unrealistically high Zr solubility and low saturation temperatures (see Harrison *et al.*,  
552 2007). In this case, diorite sample 18DB01-4, with M=2.4, would yield a saturation temperature  
553 of 575 °C, which should preclude it from crystallizing zircon. This mismatch with reality is

554 because the approach does not include the evolution of the residual melt with crystallization,  
555 which would cause the Zr content to increase and the melt composition to evolve to lower M  
556 values, with lower Zr solubility.

557 The second approach, the one taken here, considers the evolving composition of the melt during  
558 crystallization and determines when zircon crystallizes from this residual liquid, whose  
559 composition departs from the bulk composition, becoming enriched in Zr and increasingly more  
560 felsic (lower M) (Harrison *et al.*, 2007, Lee & Bachmann, 2014). This approach leads to higher  
561 and more realistic zircon saturation temperatures than the first approach (Harrison *et al.*, 2007).  
562 Here, using this approach and including Zr uptake by other minerals such as Hbl, Bt and Pl, we  
563 found zircon saturation occurs just above 700 °C for the diorite models, some 100 °C lower than  
564 the maximum values derived from Ti-in-zircon, as seen in the previous subsection. This  
565 discrepancy implies that some other processes must be at play.

#### 566 *Significance of high-Ti zircons*

567 A population of zircons from the diorites show Ti contents > 7 ppm, corresponding to > ~730  
568 °C, higher than the zircon saturation temperature derived from our models. These same diorite  
569 zircons have high contents of U, Th, HREE that define apparently compatible trends (Figs. 9  
570 and 16). Several explanations, not necessarily mutually exclusive, could account for these  
571 observations:

572 a) High-T zircons are xenocrysts or antecrysts. This is unlikely because the high-T zircons have  
573 the same internal texture,  $\epsilon_{\text{Hf}(t)}$  and U-Pb ages as low-T grains.

574 b) Presence of inclusions or “non-formula” impurities in zircons. The diorite zircons do have  
575 inclusions and cavities and are also partly metamictic with quenched CL images. The high-Ti  
576 values, coupled with high Th and REE values, could be due to inclusions of Ti-rich phases, such  
577 as titanite or allanite, where the trends with Ti would represent mixing lines. We have excluded  
578 analyses with anomalous peaks or plateaus of trace elements in the count curves (section 9.2),  
579 and modelling results show that inclusions of titanite would cause a much more rapid increase in  
580 Ti contents compared to Nd (Fig. 16a). However, it is possible that metamictization and reaction  
581 with fluids and subsequent recrystallization (Geisler *et al.*, 2007) gave rise to micrometer-scale  
582 inclusions of assorted Ti-U-Th-REE rich minerals in the zircon matrix. Alternatively, self-  
583 irradiation damage gave rise to pore space that hosts “non-formula” impurities (Geisler *et al.*,  
584 2007). At present, either alternative is valid and we conclude that despite exclusion of  
585 anomalous analyses, the Ti contents of the remaining zircons may also have been affected,  
586 explaining the high-Ti contents and positive trend between Ti and U-Th-Yb (Fig. 9). If this is  
587 the case, the Ti-in-zircon values of the diorite zircons do not reflect temperature of  
588 crystallization (Fu *et al.*, 2008).

589 c) Loss of Zr during diorite crystallization (Barnes *et al.*, 2019). In this case, the original melt  
590 had higher Zr content than the bulk rock has now, because some of the high-Zr melt was  
591 extracted leaving behind a poorer cumulate. If the diorite melt had initially higher Zr than the  
592 final rock, it would have reached zircon saturation at higher temperatures than the ones

593 calculated in Fig. 14. The interstitial melt of a crystallizing dioritic magma becomes increasingly  
594 enriched in Zr until zircon saturation, at which point the melt starts to lose Zr due to zircon  
595 precipitation (Barnes *et al.*, 2019, Harrison *et al.*, 2007, Lee & Bachmann, 2014). If part of this  
596 Zr-rich interstitial melt is extracted, the remaining mush or magma will be impoverished in Zr,  
597 while retaining some of the early-formed high-T zircons. Any remaining interstitial melt  
598 continues to crystallize zircon as the magma continues to cool. Thus, despite relatively low final  
599 Zr content, this rock will have early-formed hot zircons that mark the true, high-saturation  
600 temperature of the original magma (see Barnes *et al.*, 2019). This alternative is problematic for  
601 the Dabu rocks because to reach zircon saturation at ~830-840 °C (the upper temperatures  
602 obtained by Ti-in-zircon thermometry for our samples), the dioritic melt would need to have had  
603 an unrealistically high Zr content of >300 ppm. Therefore, while this process may have  
604 contributed to decreasing the Zr content of the evolving magma, and therefore the inferred  
605 zircon saturation temperature, it is unlikely to be the main reason for the high Ti-values of some  
606 zircons.

607 On balance, it is likely that the trace element trends in Fig. 9 and the Ti-content of diorite  
608 zircons reflect zircon alteration during metamictization, where high contents of trace elements  
609 are hosted either in pore space in amorphous remnants inside the grains or in inclusions resulting  
610 from recrystallization of the amorphous, damaged zones (Geisler *et al.*, 2007). Consequently, the  
611 Ti content in the diorite zircons is not a reliable measure of crystallization temperature.

### 612 **Preservation of euhedral zircon xenocrysts**

613 Euhedral zircon xenocrysts from the tonalite preserved in two diorite samples (18DB01-4 and  
614 18BD01-2) show negligible dissolution. This is inferred from the similarity between CL images  
615 of xenocrysts and tonalite zircons: they are euhedral with well-developed oscillatory zoning,

616 lacking obvious truncation of the oscillatory zoning in the outer part of the zircons. It is possible  
617 that a thin rim may have been dissolved or grown during final crystallization of the diorite, but  
618 they have not been recognized. In this section, we explore how these euhedral xenocrysts may  
619 have been preserved during the melting of the tonalite and mixing with the diorite, two steps  
620 where they could have been resorbed.

621 We envisage three possible processes that would prevent significant zircon resorption during  
622 melting of tonalite: small melt fraction during anatexis, zircon grains protected as inclusions in  
623 biotite, or rapid melting and transfer to the diorite with little time for resorption. All alternatives  
624 remain open. Once transferred to the dioritic magma, zircon xenocrysts would be partly or  
625 completely resorbed if the diorite was undersaturated. The fact that they are well preserved, and  
626 that corroded oval zircons or zircon cores have not been found, can be interpreted in several  
627 ways (see discussion in Barnes *et al.*, 2019, Miller *et al.*, 2007):

628 1. A zircon-undersaturated diorite magma crystallized rapidly after receiving the  
629 xenocrysts preventing their dissolution. While we cannot entirely dismiss this possibility,  
630 we note that: the diorite is fine-grained but not aphanitic or glassy, and lacks chilled  
631 margins against the host rock; granitic magma mixed with the mafic magma, suggesting  
632 that there was enough time for interaction and widespread transfer of zircons; and the  
633 diorite magma produced zircon autocrysts up to 0.4 mm long with rational crystal faces  
634 after it became zircon-saturated at low T. Combined, these features suggest that if the  
635 diorite magma was undersaturated, there would have been enough time for the xenocrysts

636 to be partly consumed before the magma becoming saturated and crystallizing its own  
637 zircon autocrysts.

638 2. Zircons could have been transferred as inclusions in residual biotite from the  
639 tonalite in the granitic melt (e.g. Clemens, 2003). However, we found no pleochroic haloes  
640 in biotite in the diorite (Fig. 5) and biotite would have been unstable in the dioritic magma  
641 at  $T > 810$  °C (for the diorite with 3 wt.%  $H_2O$ ), or  $> 750$  °C (for 6 wt.%  $H_2O$ ) (Fig. 14a).

642 In this case, biotite would have reacted out and zircons exposed to the melt. Thus,  
643 armouring would have been possible only if biotite transfer occurred at relatively low  
644 temperatures, for which the diorite would have been a mush with  $< 40\%$  melt (Fig. 14b).  
645 While we cannot discount this possibility, we do not find support for it.

646 3. If we reject the results from Ti-in-zircon thermometry considering that it could  
647 have been affected by alteration, and consider instead that the zircon saturation  
648 temperatures in Fig. 14 approach the true value, then the Dabu diorite would have reached  
649 zircon saturation between 700 to 750 °C. At these conditions, the diorite would have been a  
650 crystalline mush with only between  $\sim 23\%$  and  $\sim 26\%$  interstitial melt. In this case, the  
651 extensive magma mixing observed within the dyke would require either pervasive flow of  
652 the granitic melt through the mush, or liquefaction of the mushy diorite possibly caused by  
653 the addition of melt derived from tonalite anatexis.

654 Bringing together the field evidence, the data and the considerations regarding zircon saturation  
655 temperature (point 3 above), we propose the following sequence of events (Fig. 17): the dykes  
656 were paths of H<sub>2</sub>O-rich dioritic magmas that released heat and H<sub>2</sub>O to the surroundings as the  
657 magma became a crystalline mush. This triggered water-fluxed melting of the tonalite that  
658 released zircon grains into an anatectic granitic melt. This melt back-veined and mixed with the  
659 diorite transferring tonalite zircons to the dioritic magma, where they remained stable (or nearly  
660 so), explaining their well-preserved euhedral shapes and internal zonation. Preservation of the  
661 xenocrysts could have been either through armouring, for which we find no evidence, or through  
662 transfer to a zircon-saturated dioritic medium. Even assuming large uncertainties in the Zr  
663 content of the original melt caused by melt gain or loss during crystallization, zircon saturation  
664 temperature would have been reached when the diorite was a crystalline mush. Therefore,  
665 zircons were likely transferred to a dioritic mush through mixing. How did this occur? Mushes  
666 are permeable solids, open to invasion of foreign magmas (Xu *et al.*, 2021) and prone to  
667 liquefaction (Weinberg *et al.*, 2021). The granitic magma may have exploited permeable porous  
668 pathways through the mush leading to hybridization and influx of zircon xenocrysts into the  
669 matrix of the mush. This same ingress of granitic magma may have caused liquefaction and  
670 remobilization of the mush favouring further mixing. Both these processes could give rise to the  
671 variety of mingling features in Fig. 2c,d, including the irregular, infolded felsic dykes commonly

672 with gradational contacts with the mafic rocks, and blocks of better-preserved diorites in a  
673 hybrid rock. A detailed textural investigation of the different steps in the hybridization process  
674 in Fig. 2, with particular focus on disequilibrium textures and mineral zonation, might better  
675 reveal the nature of these processes. Determining the existence of narrow, younger rims around  
676 the xenocrysts, and with that better visualizing the shape of the xenocrystic grains, might help  
677 support this interpretation.

## 678 CONCLUSIONS

679 The intrusion of the Dabu diorite dyke swarm at 46-47 Ma is part of the waning stages of the  
680 syn-collisional magmatic flare-up of the Gangdese belt. The outcrops in Dabu record how these  
681 dykes assimilated the 77-79 Ma host tonalite by remelting it and then mixing with the newly  
682 formed melt. The tonalite melted at low temperatures fluxed by water likely released with heat  
683 by the dykes. The transfer of tonalite zircons to and their preservation in the diorite dykes  
684 provides an opportunity to explore the conditions of magma hybridization and the limits of  
685 zircon-based thermometry. Given the importance of dykes as feeders of large magma bodies,  
686 and the high H<sub>2</sub>O contents and temperatures prevalent in active magmatic arcs, the Dabu dykes  
687 could represent a common process of hybridization in magmatic arcs, akin to the mixing-  
688 assimilation-storage-homogenization, MASH, hypothesis (Hildreth & Moorbath, 1988).

689 We found that the Ti-in-zircon temperature estimations for the tonalite matched well the range  
690 defined by zircon saturation temperature predicted by modelling of crystallization/melting of the  
691 tonalite. However, the same is not true for dioritic zircon autocrysts. These yield Ti-in-zircon  
692 temperatures ranging from below the solidus to >100 °C above the zircon saturation  
693 temperatures. This discrepancy could be related either to loss of Zr during diorite crystallization  
694 (Barnes *et al.*, 2019) or to alteration and recrystallization of the zircons (Geisler *et al.*, 2007),  
695 indicated by quenched CL and high Ti contents, as well as U, Th, Ca, Fe, Y, REE (or low



696 LREE-I; Fig. 8). Either way, the results show how even through exclusion of zircons with  
697 obvious indicators of alteration, they may still have unreliable Ti values, defining unexpected  
698 trends against other trace elements (Fig. 16).

699 Interestingly, but not surprisingly, the tonalite with ~140 ppm Zr has a zircon saturation  
700 temperature close to 100 °C higher than the diorite with half the amount of Zr, indicating yet  
701 again that this temperature does not constrain the temperature of magma formation. However,  
702 for the Dabu rocks, zircon saturation temperature is useful in constraining the crystallinity of the  
703 diorite intrusion at the time of hybridization. This is because a striking feature of these rocks is  
704 that the zircon xenocrysts from the tonalite record little resorption, requiring that the xenocrysts  
705 be either armoured in biotite during mixing, or that they be exposed to a low-temperature  
706 granitic melt first, and then transferred to a zircon-saturated diorite. The absence of pleochroic  
707 haloes in biotite in the diorite and the instability of biotite in hot dioritic magmas suggest that  
708 armouring is unlikely. The low-temperature zircon saturation of ~715 °C ensures that the diorite  
709 would have been a high crystallinity mush with only ~25 wt.% melt at the time of zircon  
710 saturation. Even if the Zr content were doubled or trebled, zircon saturation in the diorite would  
711 still have occurred in a mush. Thus, we conclude that hybridization occurred in a zircon  
712 saturated mush through melt leak-off from invading granitic veins into the pore-space of the  
713 mush, possibly accompanied by liquefaction (Weinberg *et al.*, 2021). We argue that pore-  
714 invasion combined with the liquefaction of mushes is a powerful mixing process. Because of its  
715 stealthy nature, this process of magma mixing in dykes could be important during the build-up  
716 of arcs feeding large magma reservoirs with hybrid magmas.

717 The Dabu dyke swarm represents one end-member of zircon behavior during hybridization  
718 where xenocrysts are preserved with minimal resorption. This behavior helped us constrain the  
719 nature and conditions of zircon transfer and magma hybridization. However, the general rarity  
720 of zircon xenocrysts in magmatic rocks of the Gangdese arc (e.g. Zhu *et al.*, 2015) suggests that

721 complete zircon resorption could be common, leaving few tools to recognize the remelting of  
722 older arc rocks and magma hybridization. This is especially true when the arc has a narrow  
723 range of radioactive isotope ratios. Thus, assimilation through remelting of older arc rocks,  
724 followed by hybridization and homogenization (MASH, Hildreth & Moorbath, 1988) could be  
725 widespread with little evidence preserved. In such cases, disentangling magma evolution and the  
726 nature of magma hybridization require detailed field documentation accompanied by  
727 investigation of fine chemical and isotopic zonation of a range of accessories and rock-forming  
728 minerals (e.g. Barnes *et al.*, 2021, Chambers *et al.*, 2020).

## 729 **FUNDING**

730 This research was financially co-supported by the National Natural Science Foundation of China  
731 (42121002 and 91755207), the Second Tibetan Plateau Scientific Expedition and Research  
732 Program (STEP) (2019QZKK0702), and the 111 project (B18048).

## 733 **SUPPLEMENTARY DATA**

734 Supplementary data are available at Journal of Petrology online.

## 735 **Data Availability**

736 The data underlying this article are available in the article and in its online supplementary  
737 material.

## 738 **ACKNOWLEDGEMENTS**

739 We thank Vali Memeti, Calvin Miller and Bill Collins for careful and insightful reviews that  
740 much improved the original manuscript.

## 741 **REFERENCES**

742 Andersen, T. (2002). Correction of common lead in U–Pb analyses that do not report 204Pb.  
743 *Chemical Geology* **192**, 59-79.

- 744 Barnes, C. G., Werts, K., Memeti, V. & Ardill, K. (2019). Most Granitoid Rocks are Cumulates:  
745 Deductions from Hornblende Compositions and Zircon Saturation. *Journal of Petrology* **60**,  
746 2227-2240.
- 747 Barnes, C. G., Werts, K., Memeti, V., Paterson, S. R. & Bremer, R. (2021). A tale of five enclaves:  
748 Mineral perspectives on origins of mafic enclaves in the Tuolumne Intrusive Complex.  
749 *Geosphere* **17**, 352-374.
- 750 Bell, E. A., Boehnke, P. & Harrison, T. M. (2016). Recovering the primary geochemistry of Jack  
751 Hills zircons through quantitative estimates of chemical alteration. *Geochimica et*  
752 *Cosmochimica Acta* **191**, 187-202.
- 753 Blichert-Toft, J. (2008). The Hf isotopic composition of zircon reference material 91500.  
754 *Chemical Geology* **253**, 252-257.
- 755 Boehnke, P., Watson, E. B., Trail, D., Harrison, T. M. & Schmitt, A. K. (2013). Zircon saturation  
756 re-revisited. *Chemical Geology* **351**, 324-334.
- 757 Bouvier, A., Vervoort, J. D. & Patchett, P. J. (2008). The Lu–Hf and Sm–Nd isotopic composition  
758 of CHUR: Constraints from unequilibrated chondrites and implications for the bulk composition  
759 of terrestrial planets. *Earth and Planetary Science Letters* **273**, 48-57.
- 760 Bruand, E., Fowler, M., Storey, C., Laurent, O., Antoine, C., Guitreau, M., Heilimo, E. & Nebel,  
761 O. (2020). Accessory mineral constraints on crustal evolution: elemental fingerprints for magma  
762 discrimination. *Geochemical Perspectives Letters* **13**, 7-12.
- 763 Chambers, M., Memeti, V., Eddy, M. P. & Schoene, B. (2020). Half a million years of magmatic  
764 history recorded in a K-feldspar megacryst of the Tuolumne Intrusive Complex, California,  
765 USA. *Geology* **48**, 400-404.
- 766 Chu, M.-F., Chung, S.-L., O'Reilly, S. Y., Pearson, N. J., Wu, F.-Y., Li, X.-H., Liu, D., Ji, J., Chu,  
767 C.-H. & Lee, H.-Y. (2011). India's hidden inputs to Tibetan orogeny revealed by Hf isotopes of  
768 Transhimalayan zircons and host rocks. *Earth and Planetary Science Letters* **307**, 479-486.
- 769 Claiborne, L. L., Miller, C. F., Gualda, G. A. R., Carley, T. L., Covey, A. K., Wooden, J. L. &  
770 Fleming, M. A. (2018). Zircon as Magma Monitor. *Microstructural Geochronology*, 1-33.
- 771 Claiborne, L. L., Miller, C. F., Walker, B. A., Wooden, J. L., Mazdab, F. K. & Bea, F. (2006).  
772 Tracking magmatic processes through Zr/Hf ratios in rocks and Hf and Ti zoning in zircons: An  
773 example from the Spirit Mountain batholith, Nevada. *Mineralogical Magazine* **70**, 517-543.
- 774 Claiborne, L. L., Miller, C. F. & Wooden, J. L. (2010). Trace element composition of igneous  
775 zircon: a thermal and compositional record of the accumulation and evolution of a large silicic  
776 batholith, Spirit Mountain, Nevada. *Contributions to Mineralogy and Petrology* **160**, 511-531.
- 777 Clemens, J. D. (2003). S-type granitic magmas—petrogenetic issues, models and evidence. *Earth-*  
778 *Science Reviews* **61**, 1-18.
- 779 Collins, W. J., Huang, H.-Q. & Jiang, X. (2016). Water-fluxed crustal melting produces  
780 Cordilleran batholiths. *Geology* **44**, 143-146.
- 781 Collins, W. J., Murphy, J. B., Johnson, T. E. & Huang, H.-Q. (2020). Critical role of water in the  
782 formation of continental crust. *Nature Geoscience* **13**, 331-338.
- 783 Connolly, J. A. D. (2005). Computation of phase equilibria by linear programming: A tool for  
784 geodynamic modeling and its application to subduction zone decarbonation. *Earth and*  
785 *Planetary Science Letters* **236**, 524-541.
- 786 Connolly, J. A. D. & Petrini, K. (2002). An automated strategy for calculation of phase diagram  
787 sections and retrieval of rock properties as a function of physical conditions. *Journal of*  
788 *Metamorphic Geology* **20**, 697-708.

- 789 Ferry, J. M. & Watson, E. B. (2007). New thermodynamic models and revised calibrations for the  
790 Ti-in-zircon and Zr-in-rutile thermometers. *Contributions to Mineralogy and Petrology* **154**,  
791 429-437.
- 792 Frost, B. R., Barnes, C. G., Collins, W. J., Arculus, R. J., Ellis, D. J. & Frost, C. D. (2001). A  
793 geochemical classification for granitic rocks. *Journal of Petrology* **42**, 2033-2048.
- 794 Fu, B., Page, F. Z., Cavosie, A. J., Fournelle, J., Kita, N. T., Lackey, J. S., Wilde, S. A. & Valley,  
795 J. W. (2008). Ti-in-zircon thermometry: applications and limitations. *Contributions to*  
796 *Mineralogy and Petrology* **156**, 197-215.
- 797 Gagnevin, D., Daly, J. S. & Kronz, A. (2010). Zircon texture and chemical composition as a guide  
798 to magmatic processes and mixing in a granitic environment and coeval volcanic system.  
799 *Contributions to Mineralogy and Petrology* **159**, 579-596.
- 800 Geisler, T., Schaltegger, U. & Tomaschek, F. (2007). Re-equilibration of zircon in aqueous fluids  
801 and melts. *Elements* **3**, 43-50.
- 802 Griffin, W. L., Pearson, N. J., Belousova, E., Jackson, S. E., van Achterbergh, E., O'Reilly, S. Y.  
803 & Shee, S. R. (2000). The Hf isotope composition of cratonic mantle: LAM-MC-ICPMS  
804 analysis of zircon megacrysts in kimberlites. *Geochimica et Cosmochimica Acta* **64**, 133-147.
- 805 Griffin, W. L., Wang, X., Jackson, S. E., Pearson, N. J., O'Reilly, S. Y., Xu, X. & Zhou, X. (2002).  
806 Zircon chemistry and magma mixing, SE China: In-situ analysis of Hf isotopes, Tonglu and  
807 Pingtan igneous complexes. *Lithos* **61**, 237-269.
- 808 Harrison, T. M., Watson, E. B. & Aikman, A. B. (2007). Temperature spectra of zircon  
809 crystallization in plutonic rocks. *Geology* **35**, 635-638.
- 810 Hildreth, W. & Moorbath, S. (1988). Crustal contributions to arc magmatism in the Andes of  
811 Central Chile. *Contributions to Mineralogy and Petrology* **98**, 455-489.
- 812 Holland, T. J. B., Green, E. C. R. & Powell, R. (2018). Melting of Peridotites through to Granites:  
813 A Simple Thermodynamic Model in the System KNCFMASHTOCr. *Journal of Petrology* **59**,  
814 881-900.
- 815 Hoskin, P. W. O. (2005). Trace-element composition of hydrothermal zircon and the alteration of  
816 Hadean zircon from the Jack Hills, Australia. *Geochimica et Cosmochimica Acta* **69**, 637-648.
- 817 Hoskin, P. W. O. & Schaltegger, U. (2003). The Composition of Zircon and Igneous and  
818 Metamorphic Petrogenesis. *Reviews in Mineralogy and Geochemistry* **53**, 27-62.
- 819 Jagoutz, O. & Klein, B. (2018). On the importance of crystallization-differentiation for the  
820 generation of SiO<sub>2</sub>-rich melts and the compositional build-up of arc (and  
821 continental) crust. *American Journal of Science* **318**, 29-63.
- 822 Ji, W.-Q., Wu, F.-Y., Chung, S.-L., Li, J.-X. & Liu, C.-Z. (2009). Zircon U–Pb geochronology and  
823 Hf isotopic constraints on petrogenesis of the Gangdese batholith, southern Tibet. *Chemical*  
824 *Geology* **262**, 229-245.
- 825 Kapp, P. & DeCelles, P. G. (2019). Mesozoic–Cenozoic geological evolution of the Himalayan–  
826 Tibetan orogen and working tectonic hypotheses. *American Journal of Science* **319**, 159-254.
- 827 Kemp, A. I. S., Hawkesworth, C. J., Foster, G. L., Paterson, B. A., Woodhead, J. D., Hergt, J. M.,  
828 Gray, C. M. & Whitehouse, M. J. (2007). Magmatic and Crustal Differentiation History of  
829 Granitic Rocks from Hf–O Isotopes in Zircon. *Science* **315**, 980-983.
- 830 Kirkland, C. L., Yakymchuk, C., Olierook, H. K. H., Hartnady, M. I. H., Gardiner, N. J., Moyen,  
831 J.-F., Hugh Smithies, R., Szilas, K. & Johnson, T. E. (2021). Theoretical versus empirical  
832 secular change in zircon composition. *Earth and Planetary Science Letters* **554**, 116660.
- 833 Laurent, O. (2012). Les changements géodynamiques à la transition Archéen-Protérozoïque : étude  
834 des granitoïdes de la marge Nord du craton du Kaapvaal (Afrique du Sud). PhD thesis  
835 Université Blaise Pascal, Clermont-Ferrand.

- 836 Lee, C.-T. A. & Bachmann, O. (2014). How important is the role of crystal fractionation in making  
837 intermediate magmas? Insights from Zr and P systematics. *Earth and Planetary Science Letters*  
838 **393**, 266-274.
- 839 Liu, Y., Hu, Z., Gao, S., Günther, D., Xu, J., Gao, C. & Chen, H. (2008). In situ analysis of major  
840 and trace elements of anhydrous minerals by LA-ICP-MS without applying an internal standard.  
841 *Chemical Geology* **257**, 34-43.
- 842 Liu, Y., Hu, Z., Zong, K., Gao, C., Gao, S., Xu, J. & Chen, H. (2010). Reappraisal and  
843 refinement of zircon U-Pb isotope and trace element analyses by LA-ICP-MS. *Chinese Science*  
844 *Bulletin* **55**, 1535-1546.
- 845 Ludwig, K. R. (2003). *User's manual for Isoplot 3.00: a geochronological toolkit for Microsoft*  
846 *Excel*. Berkeley.
- 847 Ma, L., Wang, Q., Li, Z.-X., Wyman, D. A., Jiang, Z.-Q., Yang, J.-H., Gou, G.-N. & Guo, H.-F.  
848 (2013). Early Late Cretaceous (ca. 93Ma) norites and hornblendites in the Milin area, eastern  
849 Gangdese: Lithosphere–asthenosphere interaction during slab roll-back and an insight into early  
850 Late Cretaceous (ca. 100–80Ma) magmatic “flare-up” in southern Lhasa (Tibet). *Lithos* **172-**  
851 **173**, 17-30.
- 852 Miller, C. F., McDowell, S. M. & Mapes, R. W. (2003). Hot and cold granites? Implications of  
853 zircon saturation temperatures and preservation of inheritance. *Geology* **31**, 529-532.
- 854 Miller, J. S., Matzel, J. E. P., Miller, C. F., Burgess, S. D. & Miller, R. B. (2007). Zircon growth  
855 and recycling during the assembly of large, composite arc plutons. *Journal of Volcanology and*  
856 *Geothermal Research* **167**, 282-299.
- 857 Morel, M. L. A., Nebel, O., Nebel-Jacobsen, Y. J., Miller, J. S. & Vroon, P. Z. (2008). Hafnium  
858 isotope characterization of the GJ-1 zircon reference material by solution and laser-ablation  
859 MC-ICPMS. *Chemical Geology* **255**, 231-235.
- 860 Moyen, J.-F., Janoušek, V., Laurent, O., Bachmann, O., Jacob, J.-B., Farina, F., Fiannacca, P. &  
861 Villaros, A. (2021). Crustal melting vs. fractionation of basaltic magmas: Part 1, The bipolar  
862 disorder of granite petrogenetic models. *Lithos*, 106291.
- 863 Müntener, O. & Ulmer, P. (2018). Arc crust formation and differentiation constrained by  
864 experimental petrology. *American Journal of Science* **318**, 64-89.
- 865 Paton, C., Hellstrom, J., Paul, B., Woodhead, J. & Hergt, J. (2011). Iolite: Freeware for the  
866 visualisation and processing of mass spectrometric data. *Journal of Analytical Atomic*  
867 *Spectrometry* **26**, 2508-2518.
- 868 Reubi, O. & Blundy, J. (2009). A dearth of intermediate melts at subduction zone volcanoes and  
869 the petrogenesis of arc andesites. *Nature* **461**, 1269-1273.
- 870 Rubatto, D. & Hermann, J. (2007). Experimental zircon/melt and zircon/garnet trace element  
871 partitioning and implications for the geochronology of crustal rocks. *Chemical Geology* **241**, 38-  
872 61.
- 873 Schiller, D. & Finger, F. (2019). Application of Ti-in-zircon thermometry to granite studies:  
874 problems and possible solutions. *Contributions to Mineralogy and Petrology* **174**, 51.
- 875 Shand, S. J. (1943). *Eruptive Rocks: Their Genesis, Composition, Classification, and Their*  
876 *Relation to Ore-Deposits with a Chapter on Meteorite*. New York: John Wiley & Sons.
- 877 Siégel, C., Bryan, S. E., Allen, C. M. & Gust, D. A. (2018). Use and abuse of zircon-based  
878 thermometers: A critical review and a recommended approach to identify antecrystic zircons.  
879 *Earth-Science Reviews* **176**, 87-116.
- 880 Sláma, J., Košler, J., Condon, D. J., Crowley, J. L., Gerdes, A., Hanchar, J. M., Horstwood, M. S.  
881 A., Morris, G. A., Nasdala, L., Norberg, N., Schaltegger, U., Schoene, B., Tubrett, M. N. &  
882 Whitehouse, M. J. (2008). Plešovice zircon — A new natural reference material for U–Pb and  
883 Hf isotopic microanalysis. *Chemical Geology* **249**, 1-35.

- 884 Söderlund, U., Patchett, P. J., Vervoort, J. D. & Isachsen, C. E. (2004). The  $^{176}\text{Lu}$  decay constant  
885 determined by Lu–Hf and U–Pb isotope systematics of Precambrian mafic intrusions. *Earth and*  
886 *Planetary Science Letters* **219**, 311-324.
- 887 Sun, S.-s. & McDonough, W. F. (1989). Chemical and isotopic systematics of oceanic basalts:  
888 implications for mantle composition and processes. *Geological Society, London, Special*  
889 *Publications* **42**, 313-345.
- 890 Symington, N. J., Weinberg, R. F., Hasalová, P., Wolfram, L. C., Raveggi, M. & Armstrong, R. A.  
891 (2014). Multiple intrusions and remelting-remobilization events in a magmatic arc: The St. Peter  
892 Suite, South Australia. *Bulletin of the Geological Society of America* **126**, 1200-1218.
- 893 Troch, J., Ellis, B. S., Schmitt, A. K., Bouvier, A.-S. & Bachmann, O. (2018). The dark side of  
894 zircon: textural, age, oxygen isotopic and trace element evidence of fluid saturation in the  
895 subvolcanic reservoir of the Island Park-Mount Jackson Rhyolite, Yellowstone (USA).  
896 *Contributions to Mineralogy and Petrology* **173**, 54.
- 897 Wang, R., Richards, J. P., Hou, Z.-q., An, F. & Creaser, R. A. (2015). Zircon U–Pb age and Sr–  
898 Nd–Hf–O isotope geochemistry of the Paleocene–Eocene igneous rocks in western Gangdese:  
899 Evidence for the timing of Neo-Tethyan slab breakoff. *Lithos* **224-225**, 179-194.
- 900 Wang, R., Weinberg, R. F., Collins, W. J., Richards, J. P. & Zhu, D.-c. (2018). Origin of  
901 postcollisional magmas and formation of porphyry Cu deposits in southern Tibet. *Earth-Science*  
902 *Reviews* **181**, 122-143.
- 903 Watson, E. B. & Harrison, T. M. (1983). Zircon saturation revisited: temperature and composition  
904 effects in a variety of crustal magma types. *Earth and Planetary Science Letters* **64**, 295-304.
- 905 Watson, E. B., Wark, D. A. & Thomas, J. B. (2006). Crystallization thermometers for zircon and  
906 rutile. *Contributions to Mineralogy and Petrology* **151**, 413.
- 907 Weinberg, R. F. & Dunlap, W. J. (2000a). Growth and deformation of the Ladakh batholith,  
908 northwest Himalayas: Implications for timing of continental collision and origin of calc-alkaline  
909 batholiths. *Journal of Geology* **108**, 303-320.
- 910 Weinberg, R. F. & Dunlap, W. J. (2000b). Growth and Deformation of the Ladakh Batholith,  
911 Northwest Himalayas: Implications for Timing of Continental Collision and Origin of  
912 Calc-Alkaline Batholiths. *Journal of Geology* **108**, 303-320.
- 913 Weinberg, R. F., Vernon, R. & Schmelling, H. (2021). Granitic mushes: their role in magma  
914 mixing and assimilation of solids with special focus on enclaves. *Earth-Science Reviews* **220**,  
915 103665.
- 916 White, L. T., Ahmad, T., Ireland, T. R., Lister, G. S. & Forster, M. A. (2011). Deconvolving  
917 episodic age spectra from zircons of the Ladakh Batholith, northwest Indian Himalaya.  
918 *Chemical Geology* **289**, 179-196.
- 919 Xu, W., Zhu, D.-C., Wang, Q., Weinberg, R. F., Wang, R., Li, S.-M., Zhang, L.-L. & Zhao, Z.-D.  
920 (2021). Cumulate mush hybridization by melt invasion: Evidence from compositionally-diverse  
921 amphiboles in ultramafic-mafic arc cumulates within the eastern Gangdese Batholith, southern  
922 Tibet. *Journal of Petrology* **61**, ega073.
- 923 Yin, A. & Harrison, T. M. (2000). Geologic evolution of the Himalayan-Tibetan orogen. *Annual*  
924 *Review of Earth and Planetary Sciences*, 211-280.
- 925 Zhang, L.-L., Zhu, D.-C., Wang, Q., Zhao, Z.-D., Liu, D. & Xie, J.-C. (2019). Late Cretaceous  
926 volcanic rocks in the Sangri area, southern Lhasa Terrane, Tibet: Evidence for oceanic ridge  
927 subduction. *Lithos* **326-327**, 144-157.
- 928 Zhang, Z., Ding, H., Palin, R. M., Dong, X., Tian, Z. & Chen, Y. (2020). The lower crust of the  
929 Gangdese magmatic arc, southern Tibet, implication for the growth of continental crust.  
930 *Gondwana Research* **77**, 136-146.

- 931 Zhang, Z., Zhao, G., Santosh, M., Wang, J., Dong, X. & Shen, K. (2010). Late Cretaceous  
932 charnockite with adakitic affinities from the Gangdese batholith, southeastern Tibet: Evidence  
933 for Neo-Tethyan mid-ocean ridge subduction? *Gondwana Research* **17**, 615-631.
- 934 Zhu, D.-C., Wang, Q., Chung, S.-L., Cawood, P. A. & Zhao, Z.-D. (2019). Gangdese magmatism  
935 in southern Tibet and India–Asia convergence since 120 Ma. *Geological Society, London,*  
936 *Special Publications* **483**, 583-604.
- 937 Zhu, D.-C., Wang, Q., Weinberg, R. F., Cawood, P. A., Chung, S.-L., Zheng, Y.-F., Zhao, Z.,  
938 Hou, Z.-Q. & Mo, X.-X. (2022). Interplay between oceanic subduction and continental collision  
939 in building continental crust. *Nature Communications* **13**, 7141.
- 940 Zhu, D.-C., Wang, Q., Zhao, Z.-D., Chung, S.-L., Cawood, P. A., Niu, Y., Liu, S.-A., Wu, F.-Y. &  
941 Mo, X.-X. (2015). Magmatic record of India-Asia collision. *Scientific Reports* **5**, 14289.
- 942 Zhu, D.-C., Zhao, Z.-D., Niu, Y., Mo, X.-X., Chung, S.-L., Hou, Z.-Q., Wang, L.-Q. & Wu, F.-Y.  
943 (2011). The Lhasa Terrane: Record of a microcontinent and its histories of drift and growth.  
944 *Earth and Planetary Science Letters* **301**, 241-255.
- 945

946 **Figure Captions**

947 Fig. 1. a) Geological map of the Gangdese Batholith linking to the Ladakh Batholith in the west.  
 948 Small rectangle in the east shows the location of (b). Inset shows the location of (a). b)  
 949 Geological map of the area surrounding the village of Dabu and the dykes investigated here.  
 950 BNSZ refers to the Bangong-Nujiang Suture Zone, SNMZ to the Shiquanhe–Nam Tso Mélange  
 951 Zone, LMF to Luobadui–Milashan Fault, IYZSZ to the Indus–Yarlung Tsangpo Suture Zone,  
 952 and MBT refers to the Main Boundary Thrust.

953 Fig. 2. Field relationships. a) Diorite dykes cutting through tonalite close to Dabu village. All  
 954 samples and photographs are from this location. Small black ellipse on lower left indicates a  
 955 small van for scale. Rectangle on right-hand side marks the position of (b). b) Tip of dykes with  
 956 variable width and orientation. Vertical scale is ~3m. (c) irregular boundary between dyke and  
 957 tonalite with back-veining of a finer granitic rock. d) Irregularities at the contact at cm-scale. e)  
 958 and f) Heterogeneous diorite with irregular veins with sharp to diffuse margins linked to  
 959 irregular patches with gradational contact with the diorite. These are interpreted to record the  
 960 nature of mingling and mixing of between granitic and dioritic magmas.

961 Fig. 3. Major element features of the studied samples (Frost *et al.*, 2001). a) FeO/(FeO+MgO) vs  
 962 SiO<sub>2</sub> showing the boundary between ferroan and magnesian plutonic rocks; b) SiO<sub>2</sub>–MALI  
 963 (wt.%) binary diagram (MALI = Modified alkali-lime index, Na<sub>2</sub>O+K<sub>2</sub>O–CaO) from Frost *et al.*  
 964 (2001); (c) ASI vs. A/NK diagram [atomic Al/(Ca+Na+K) vs. Al/(Na+K)] (Shand, 1943). Tonalites  
 965 and diorites are magnesian, calc-alkalic and metaluminous to weakly peraluminous.

966 Fig. 4. MORB-normalized (Sun & McDonough, 1989) trace element patterns for the studied  
 967 samples.

968 Fig. 5. Photomicrographs of diorite samples. a) Sample 18DB01-2 showing euhedral to  
 969 subhedral biotite in brown tones and hornblende in green tones. Notice apatite needles in  
 970 plagioclase dominated areas (transparent) (ppl); b) sample 8DB01-2 showing biotite in an  
 971 equant matrix of twinned plagioclase. Note labelled epidote inclusion in biotite (xpl); c) sample  
 972 17DB01-2 (ppl); d) sample 18DB01-4 showing anhedral hornblende and subhedral biotite  
 973 surrounding aggregates of plagioclase (transparent) (ppl). Apatite and epidote grains are  
 974 indicated. Note absence of pleochroic haloes in biotite in all photomicrographs.

975 Fig. 6. Zircon CL images. Diorite samples 17DB01-2 (a) and 18DB01-2 (b). Zircons have  
 976 roughly rectangular shapes with two parallel rational faces and two irregular sides. They are  
 977 generally dark, but some are grey or bright, with either no zoning, irregular zoning or wide



978 bands. The two samples have contrasting zircon sizes. c) Tonalite sample 18DB01-3 showing  
979 representative grains similar to the other two tonalite samples. Zircons are euhedral, bright with  
980 well-developed, continuous oscillatory zoning. Some rare grains show a quenched region  
981 overprinting the early-formed zoning (left-side of bottom grain). d) Diorite sample 18DB01-4  
982 with two distinct zircon morphological groups: a small group of euhedral zircons labelled  
983 xenocrysts, similar to those from the tonalite in (c), and a larger group similar to those from the  
984 diorites in (a) and (b). The xenocrysts have ages that coincide with those of the tonalite samples.  
985 Green, red and black dashed circles indicate position of analytical spot and colour indicates  
986 origin of the zircon: diorite, tonalite and xenocryst in diorite, respectively. Numbers indicate U-  
987 Pb age obtained. The scale in (a) applies to all images.

988 Fig. 7. a) REE plot normalized to chondrite (Sun & McDonough, 1989). Zircons from the  
989 tonalitic host define similar patterns to the xenocrysts in the diorite sample 18DB01-4, both  
990 dated at between 70 and 80 Ma (see Fig. 11d). Diorite zircon autocrysts have higher values than  
991 the tonalite zircons and show a wide variation in LREE values (six orders of magnitude for La)  
992 reflecting alteration effects (e.g. Bell *et al.*, 2016). b) Yb/Dy vs Eu/Eu\* showing trace element  
993 similarity between the xenocryst zircons in diorite and tonalite autocrysts.

994 Fig. 8. Zircon trace element versus the Light Rare Earth Element Index [ $LREE-I = (Dy/Nd +$   
995  $Dy/Sm)$ ] (a proxy for zircon alteration Bell *et al.*, 2016) and U content. Diorite zircon analyses  
996 are divided into two groups based on CL: types 1-2 clean grey sections of grains and types 3-4  
997 regions dominated by metamictization and CL quenching; see Supplementary Data Electronic  
998 Appendix 2). There is considerable overlap between the two groups but types 3-4 have  
999 systematically lower LREE-1 and higher contents of all trace elements. In (a) and (b) Fe and Ti  
1000 define negative trends with LREE-1 (in these figures, types 3-4 symbols were placed in front of  
1001 types 1-2 for better visualization of the link between zircons deemed altered and LREE-I values.  
1002 Types 3-4 zircon analyses concentrate, as expected, in the lower end of LREE-1, indicative of  
1003 alteration, but reach values of 100, considerably higher than the cutoff value of 30 for alteration  
1004 of Bell *et al.* (2016). Up to 100, types 3-4 overlap with types 1-2, and these can have very high  
1005 contents of Ti. In (c) to (h), Fe, Ca, Th, Y reach values close to 10,000 ppm or 1 wt.%, defining  
1006 positive trends with U, which reaches up to 9000 ppm. Titanium also defines a positive trend  
1007 with U, with numerous analyses above 30 ppm, some reaching a few 100 ppm. The trend  
1008 defined by Hf and Ti in diorite zircons are the opposite to those found for granitic rocks by  
1009 Claiborne *et al.* (2010) shown by the grey fields, and similar to the high-U zircons in Fig. 6 in  
1010 Troch *et al.* (2018). In (c) to (h), types 3-4 zircon symbols were placed behind types 1-2. For

1011 tonalite zircons, the trends are similar to those in Claiborne et al. (2010). Tonalite zircons and  
1012 xenocrysts in diorite sample 18DB01-4 are not differentiated and overlap in the plots. All plots  
1013 are log-log scale.

1014 Fig. 9. (a-d) Binary plots of typically incompatible elements versus Ti in zircon. For tonalite  
1015 samples Hf behaves incompatibly defining negative, but all other elements define a curved  
1016 shape changing from a positive (compatible) to a negative (incompatible) trend as Ti increases.  
1017 This is not the case for the diorite sample for which U, Th, and Yb, define only positive or  
1018 compatible trends with Ti, and only Hf defines a negative (incompatible) trend. The compatible  
1019 trends are surprising and contrast with the incompatible trends found by Claiborne et al (2010)  
1020 indicated by grey fields. Ti-values higher than 40 ppm were not plotted as they correspond to  
1021 unrealistically high T and therefore probably correspond to altered zircons. Grey empty symbols  
1022 indicate analyses with anomalous peaks or plateaus of Fe and Ca, key indicators of  
1023 metamictization and zircon re-equilibration (see section 9.2 for discussion). All plots are log-log  
1024 scale and symbols are as in legend for Fig. 8.

1025 Fig. 10. Concordia diagrams for zircon analyses from diorite samples. a-c) Diorite dyke  
1026 samples 17DB01-2, 18DB01-2 and 18DB01-4 with ages centred around 46 to 47 Ma. Samples  
1027 18DB01-2 and 18DB01-4 also contained 70-80 Ma xenocrysts shown in Fig. 11. d) Comparison  
1028 between ages of zircon analyses from diorite sample 18DB01-4 as a function of CL type shows  
1029 no systematic shift between CL types 1-2, and the quenched CL types 3-4 despite the  
1030 anomalously high values of Th+U and other trace elements in the latter (Fig. 8). All ellipses in  
1031 (a-c) and bars in (d) mark the  $2\sigma$  confidence level. A number of analyses have been excluded: 2  
1032 of 74 analyses for 17DB01-2 (1 with large error, 1 with fluctuating age signals), 18 out of 75 for  
1033 18DB01-2 (16 discordant and 2 outliers), 25 out of 111 for 18DB01-4 (23 discordant, 1 outlier  
1034 and 1 with large error). A small number of outlier dates were removed from the calculation of  
1035 the mean age by Isoplot: 2 out of 72 for sample 17DB01-2, 2 out of 57 for sample 18DB01-2, 4  
1036 out of 86 for sample 18DB01-4. In (d), analyses in light grey at the high-end of values, have  
1037 been dates removed from the calculation of the mean age.

1038 Fig. 11. Concordia diagrams for zircon analyses from tonalite samples and xenocrysts in diorite  
1039 samples. a-c) Tonalite samples 17DB01-1, 18DB01-1, 18DB01-3 showing ages centred between  
1040 77 and 79 Ma and lacking older xenocrysts. d) and e) Xenocrysts from diorite dyke sample  
1041 18DB01-4 and 18DB01-2. The spread of dates in (d) and (e) imply that the mean ages are not  
1042 meaningful with  $MSWD > 10$ . All ellipses mark the  $2\sigma$  confidence level. A small number of  
1043 analyses have been excluded from the diagrams: 1 of 18 analyses for sample 17DB01-1 ( $>10\%$

1044 discordant), 5 of 68 for 18DB01-1 (2 discordant and 3 outlier), and 3 of 19 for 18DB01-4 (2  
1045 with very large errors and 1 outlier). A small number of outliers were removed from the  
1046 calculation of the mean age by Isoplot: 4 out of 63 for sample 18DB01-1, and 2 out of 18 for  
1047 sample 18DB01-3.

1048 Fig. 12.  $^{206}\text{Pb}/^{238}\text{U}$  ages for zircons from diorites show no systematic trend with Th+U content.  
1049 Symbols as in legend for Fig. 8 where empty symbols are types 3-4.

1050 Fig. 13.  $\epsilon_{\text{Hf}(t)}$  values for all six samples plotted against zircon U-Pb age. The ~77-79 Ma tonalite  
1051 zircons have  $\epsilon_{\text{Hf}(t)}$  centred around  $+9 \pm 1$ , whereas the ~46-47 Ma diorite analyses are more  
1052 spread between +6 and +11. N=344 analyses, with 78 from tonalite zircons and 266 from  
1053 diorite.

1054 Fig. 14. Model of crystallization for a diorite melt with 73 ppm Zr and a tonalite melt with 144  
1055 ppm Zr. H<sub>2</sub>O contents for the diorite of 3 wt.% H<sub>2</sub>O (left column), and 6 wt.% H<sub>2</sub>O (middle  
1056 column) are shown. Tonalite melt contains 2 wt.% H<sub>2</sub>O. Low H<sub>2</sub>O content was assumed in order  
1057 to investigate its remelting by H<sub>2</sub>O derived from the diorite intrusion. a) Minerals and melt/H<sub>2</sub>O  
1058 proportions. Diorite solidus T ( $T_{\text{sol}}$ ) is 677 °C, and 650 °C for the tonalite. The two diorite  
1059 models show nearly 70 °C difference water saturation T. Sphene, spinel and ilmenite form in  
1060 diorite and tonalite not shown because of low proportions. b) Melt fraction. For all three cases  
1061 the last ~20% crystallizes within 10 °C of the solidus. c) Zr content in melt. Values increase  
1062 until the curve intersects the zircon saturation curves calculated using M-values in (d) and  
1063 calibrations in Boehnke et al. (2013) and Watson and Harrison (1983). Zircon saturation for the  
1064 diorites is reached at 714 and 711 °C, for 3 and 6 wt.% H<sub>2</sub>O, respectively, where ~23% melt (for  
1065 3% H<sub>2</sub>O) or ~ 26% melt (for 6% H<sub>2</sub>O) remain. Tonalite reaches ~ 20% melt at ~650 °C solidus,  
1066 where ~ 90% of the zircons are stable. d) M-value of residual melt used to determine the zircon  
1067 saturation curve in (c). M-value for diorites steadily decrease to reach a value of 1.4 close to the  
1068 solidus. For the tonalite M first decreases from a value of 1.45 at the liquidus (not shown) and  
1069 then increases to ~1.4 at the solidus, due to stabilization of Bt and Qtz. e)  $a(\text{SiO}_2)$  and  $a(\text{TiO}_2)$ . f)  
1070 Ti-in-zircon calculated using curves in (e) (solid lines) or assuming a fixed value of  $a(\text{SiO}_2)=1$   
1071 and  $a(\text{TiO}_2)=0.7$  (dashed lines; similar to Claiborne et al. (2010)). The differences between the  
1072 two curves are small. Calculations use Ferry and Watson (2007). g) Zr content in melt, non-  
1073 zircon phases and zircon as a function of temperature (note different scale in x-axis). Zircons are  
1074 saturated close to the solidus for diorite. Diorite composition is similar to the basalt modelled by

1075 Lee and Bachmann (2014) (their Fig. 2b), but despite higher Zr in our starting composition, melt  
1076 never reaches the > 300 ppm Zr in their model, peaking instead at ~ 150 ppm, due to significant  
1077 intake of Zr in non-zircon minerals excluded in their model.

1078 Fig. 15. Comparison of signal outputs from zircon analyses for sample 18DB01-4: a) spot 1-04  
1079 in a type 1 zircon, and b) spot 2-41 in a type 2 zircon. Data from (b) was excluded from  
1080 consideration because of anomalous plateaus of Fe, Ca, Ti, and a sudden drop in Th, U counts.

1081 Fig. 16. Zircon chemistry modelling. a) Modelled zircon Th vs Ti composition for the diorite  
1082 and tonalite (thick black lines) compared with data for zircons from diorite dykes, xenocrystic  
1083 zircons in diorite and tonalite host rock zircons; b) same for Nd vs Ti. Analysed zircon grains  
1084 are colour coded according to “reliability”: if the zircon analysis has anomalous Fe or Ca signal  
1085 it is deemed unreliable, if it has anomalous peaks or plateaus of Y, Th, Ti or HREE it is deemed  
1086 dubious, otherwise it is classified as magmatic. Models are calculated as discussed in the text  
1087 and uses Boehnke et al.’s (2013) model for saturation, but the results are very similar using  
1088 Watson & Harrison (1983). For comparison (a) shows the approximate slope of the trend (thick  
1089 grey arrow) defined by the data for granitic rocks in Claiborne et al. (2006), which is similar to  
1090 the modelled slope for the tonalite (thick dashed line). The yellow band in (b) defines the field  
1091 generated by mixing a zircon composition with 3 ppm Ti and 1 ppm Nd, with titanite with  
1092 24.4 % Ti and between 1000 and 10000 ppm Nd (Bruand *et al.*, 2020). The band indicates that  
1093 mixing with titanite is unlikely to explain the trend because it causes a stronger enrichment in Ti  
1094 compared to Nd.

1095 Fig. 17. Assimilation of host rock through anatexis, back-veining and mixing with zircon  
1096 transfer. a) Original dioritic magma intrusion at temperatures above zircon saturation. As  
1097 magma flows and cools, it heats-up the surrounding and releases H<sub>2</sub>O. b) The tonalite melts at  
1098 relatively low temperatures lacking anhydrous peritectic minerals. Granitic dykelets derived  
1099 from tonalite anatexis back-veins the diorite that is now a cool zircon-saturated mush. The mush  
1100 deforms in a ductile fashion and granitic melt flow through the pore space of the mush (inset)  
1101 transferring tonalite zircons and hybridizing the diorite. Zircon xenocrysts are preserved in the  
1102 zircon-saturated diorite. Size of zircons is exaggerated.

**Table 1. Major element composition of the tonalite and diorite samples.**

No.	Label	Lithology	[SiO <sub>2</sub> ]	[TiO <sub>2</sub> ]	[Al <sub>2</sub> O <sub>3</sub> ]	[TFe <sub>2</sub> O <sub>3</sub> ]	[MnO]	[MgO]	[CaO]	[Na <sub>2</sub> O]	[K <sub>2</sub> O]
1	17DB01-2	diorite	57.76	0.69	17.98	7.04	0.14	3.66	6.65	3.98	1.85
2	18DB01-2	diorite	58.45	0.49	18.86	6.40	0.09	2.66	6.95	4.54	1.20
3	18DB01-4	diorite	54.06	0.73	18.29	8.67	0.17	4.68	7.60	3.83	1.72
4	17DB01-1	tonalite	69.91	0.24	16.24	2.30	0.07	0.58	2.91	4.37	3.28
5	18DB01-1	tonalite	68.42	0.26	16.85	2.56	0.07	0.64	2.92	4.35	3.81
6	18DB01-3	tonalite	68.96	0.29	16.96	2.80	0.05	0.74	3.43	4.56	2.08
	average tonalite		69.10	0.26	16.68	2.55	0.06	0.65	3.08	4.43	3.06

[P <sub>2</sub> O <sub>5</sub> ]	Mg#	A/CNK	K <sub>2</sub> O/Na <sub>2</sub> O	Zr
0.25	51	0.87	0.46	73.2
0.36	45	0.88	0.26	102
0.26	52	0.83	0.45	74.1
0.10	33	1.01	0.75	132
0.12	33	1.01	0.88	134
0.14	35	1.06	0.46	163
0.12	34	1.03	0.69	143

*A complete list of trace elements and repeat analyses are listed in Supplementary Data*

*Electronic Appendix 4. Zr contents in the repeat vary typically by 2 to 10 ppm, except for sample 17DB01-1 for which the repeat yielded 114 ppm instead of 132 ppm. The results are normalized to anhydrous values (LOI-free). Values in the Supplementary Data Electronic Appendix 4 are not normalized and include the LOI values that vary from 0.2 to 0.7% for the tonalites and 0.4 to 0.9% for the diorites. Tonalite average corresponds to the composition used in the model calculations. Mg# = [MgO/(MgO+FeO) x 100], A/CNK = molar ratio Al<sub>2</sub>O<sub>3</sub>/ (CaO+Na<sub>2</sub>O+K<sub>2</sub>O).*

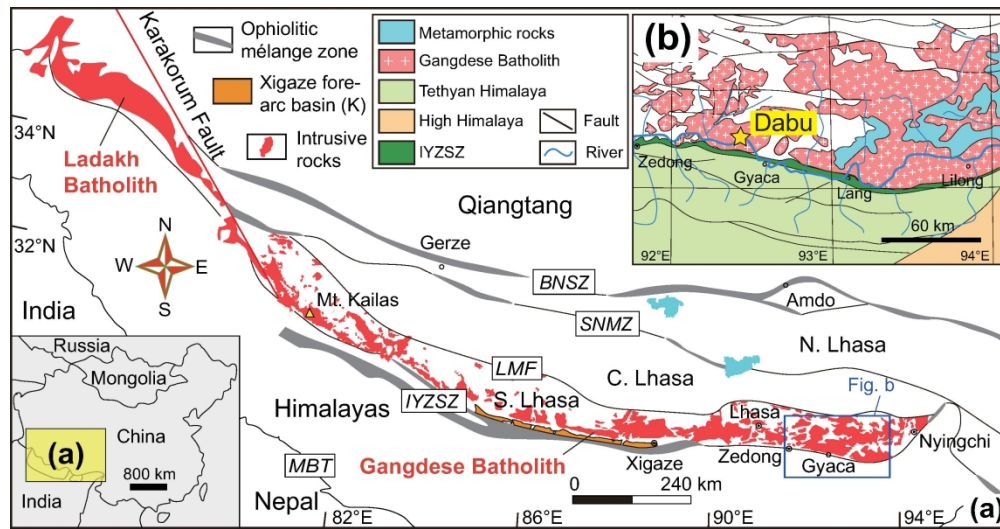


Fig. 1. a) Geological map of the Gangdese Batholith linking to the Ladakh Batholith in the west. Small rectangle in the east shows the location of (b). Inset shows the location of (a). b) Geological map of the area surrounding the village of Dabu and the dykes investigated here. BNSZ refers to the Bangong-Nujiang Suture Zone, SNMZ to the Shiquanhe–Nam Tso Mélange Zone, LMF to Luobadui-Milashan Fault, IYZSZ to the Indus-Yarlung Tsangpo Suture Zone, and MBT refers to the Main Boundary Thrust.

131x68mm (600 x 600 DPI)

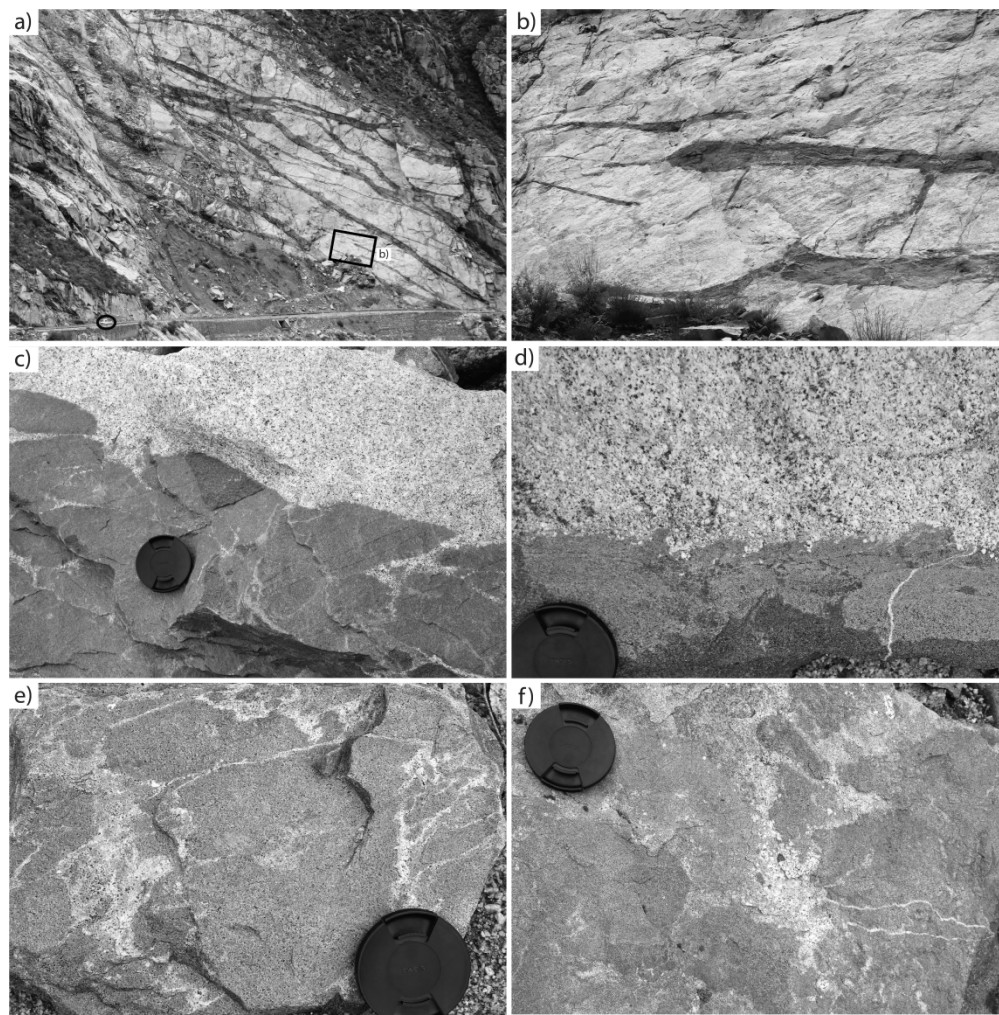


Fig. 2. Field relationships. a) Diorite dykes cutting through tonalite close to Dabu village. All samples and photographs are from this location. Small black ellipse on lower left indicates a small van for scale. Rectangle on right-hand side marks the position of (b). b) Tip of dykes with variable width and orientation. Vertical scale is  $\sim 3\text{m}$ . (c) irregular boundary between dyke and tonalite with back-veining of a finer granitic rock. d) Irregularities at the contact at cm-scale. e) and f) Heterogeneous diorite with irregular veins with sharp to diffuse margins linked to irregular patches with gradational contact with the diorite. These are interpreted to record the nature of mingling and mixing of between granitic and dioritic magmas.

402x407mm (300 x 300 DPI)

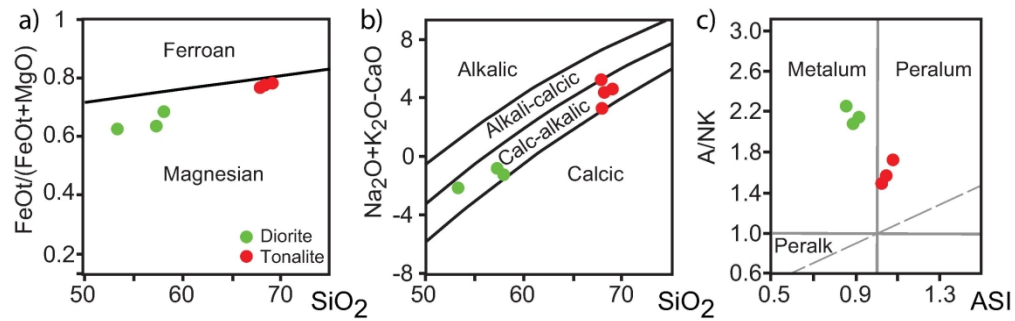


Fig. 3. Major element features of the studied samples (Frost et al., 2001). a) FeO/(FeO+MgO) vs SiO<sub>2</sub> showing the boundary between ferroan and magnesian plutonic rocks; b) SiO<sub>2</sub>-MALI (wt.%) binary diagram (MALI = Modified alkali-lime index, Na<sub>2</sub>O+K<sub>2</sub>O-CaO) from Frost et al. (2001); (c) ASI vs. A/NK diagram [atomic Al/Ca+Na+K vs. Al/(Na+K)] (Shand, 1943). Tonalites and diorites are magnesian, calc-alkalic and metaluminous to weakly peraluminous.

136x43mm (600 x 600 DPI)



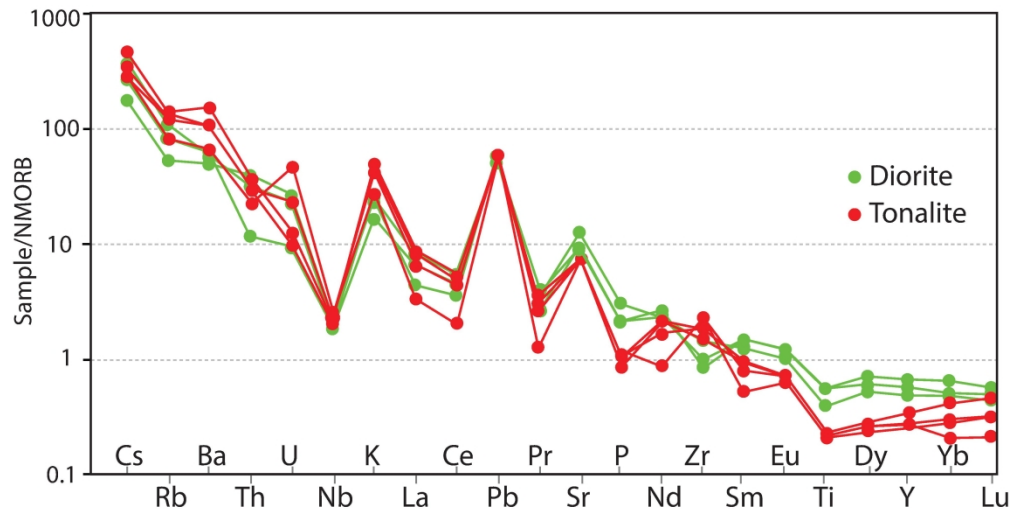


Fig. 4. MORB-normalized (Sun & McDonough, 1989) trace element patterns for the studied samples.

167x85mm (600 x 600 DPI)

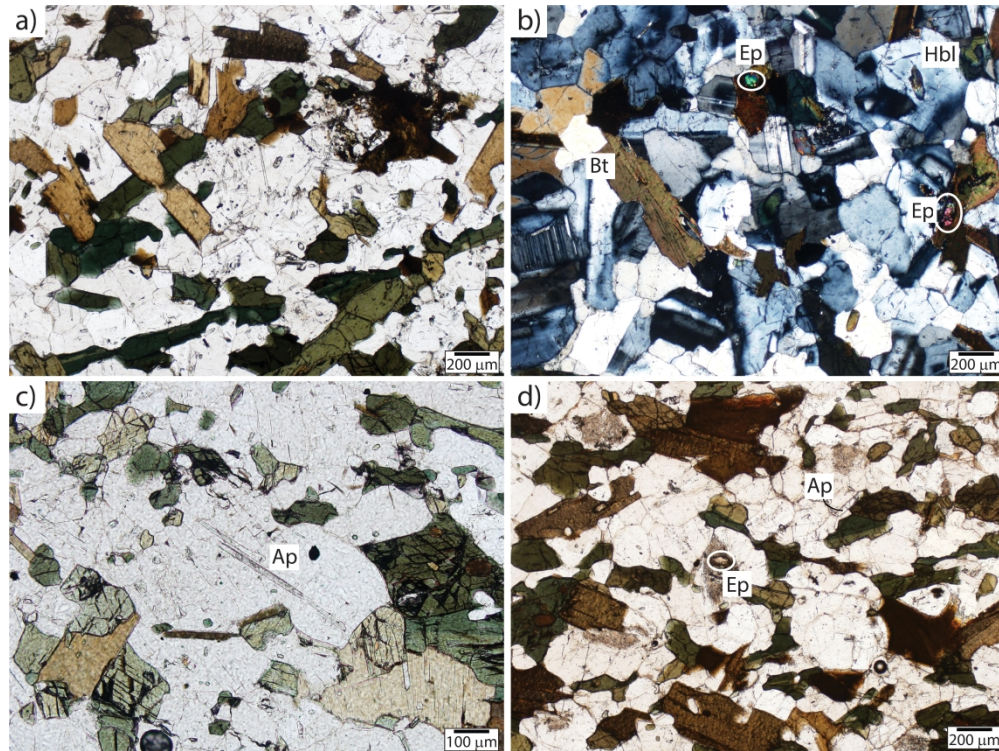


Fig. 5. Photomicrographs of diorite samples. a) Sample 18DB01-2 showing euhedral to subhedral biotite in brown tones and hornblende in green tones. Notice apatite needles in plagioclase dominated areas (transparent) (ppl); b) sample 8DB01-2 showing biotite in an equant matrix of twinned plagioclase. Note labelled epidote inclusion in biotite (xpl); c) sample 17DB01-2 (ppl); d) sample 18DB01-4 showing anhedral hornblende and subhedral biotite surrounding aggregates of plagioclase (transparent) (ppl). Apatite and epidote grains are indicated. Note absence of pleochroic haloes in biotite in all photomicrographs.

323x241mm (600 x 600 DPI)

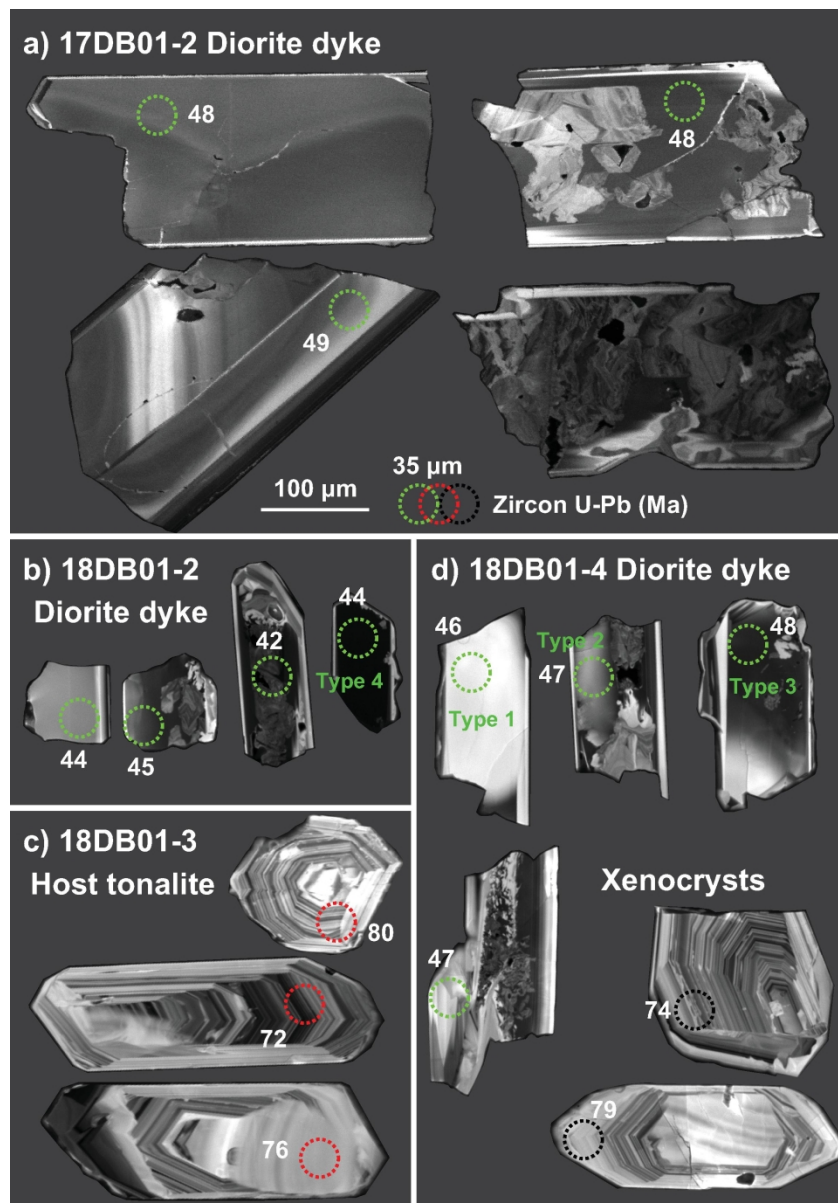


Fig. 6. Zircon CL images. Diorite samples 17DB01-2 (a) and 18DB01-2 (b). Zircons have roughly rectangular shapes with two parallel rational faces and two irregular sides. They are generally dark, but some are grey or bright, with either no zoning, irregular zoning or wide bands. The two samples have contrasting zircon sizes. c) Tonalite sample 18DB01-3 showing representative grains similar to the other two tonalite samples. Zircons are euhedral, bright with well-developed, continuous oscillatory zoning. Some rare grains show a quenched region overprinting the early-formed zoning (left-side of bottom grain). d) Diorite sample 18DB01-4 with two distinct zircon morphological groups: a small group of euhedral zircons labelled xenocrysts, similar to those from the tonalite in (c), and a larger group similar to those from the diorites in (a) and (b). The xenocrysts have ages that coincide with those of the tonalite samples. Green, red and black dashed circles indicate position of analytical spot and colour indicates origin of the zircon: diorite, tonalite and xenocryst in diorite, respectively. Numbers indicate U-Pb age obtained. The scale in (a) applies to all images.

96x138mm (600 x 600 DPI)



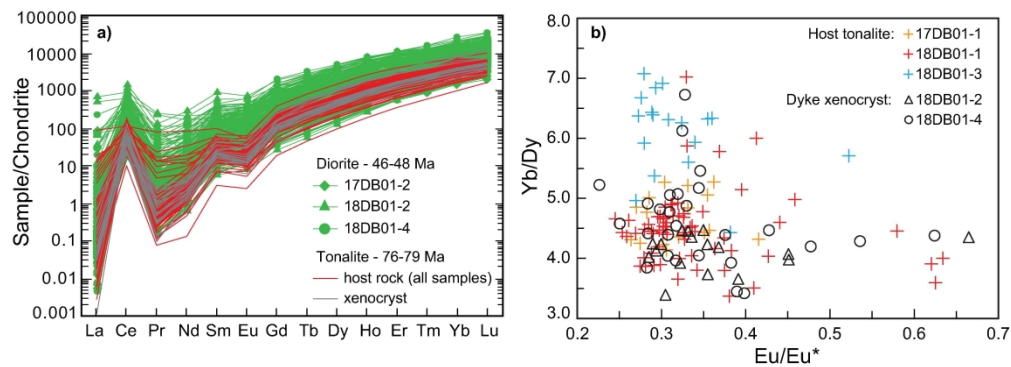


Fig. 7. a) REE plot normalized to chondrite (Sun & McDonough, 1989). Zircons from the tonalitic host define similar patterns to the xenocrysts in the diorite sample 18DB01-4, both dated at between 70 and 80 Ma (see Fig. 11d). Diorite zircon autocrysts have higher values than the tonalite zircons and show a wide variation in LREE values (six orders of magnitude for La) reflecting alteration effects (e.g. Bell et al., 2016). b) Yb/Dy vs Eu/Eu\* showing trace element similarity between the xenocryst zircons in diorite and tonalite autocrysts.

166x60mm (600 x 600 DPI)

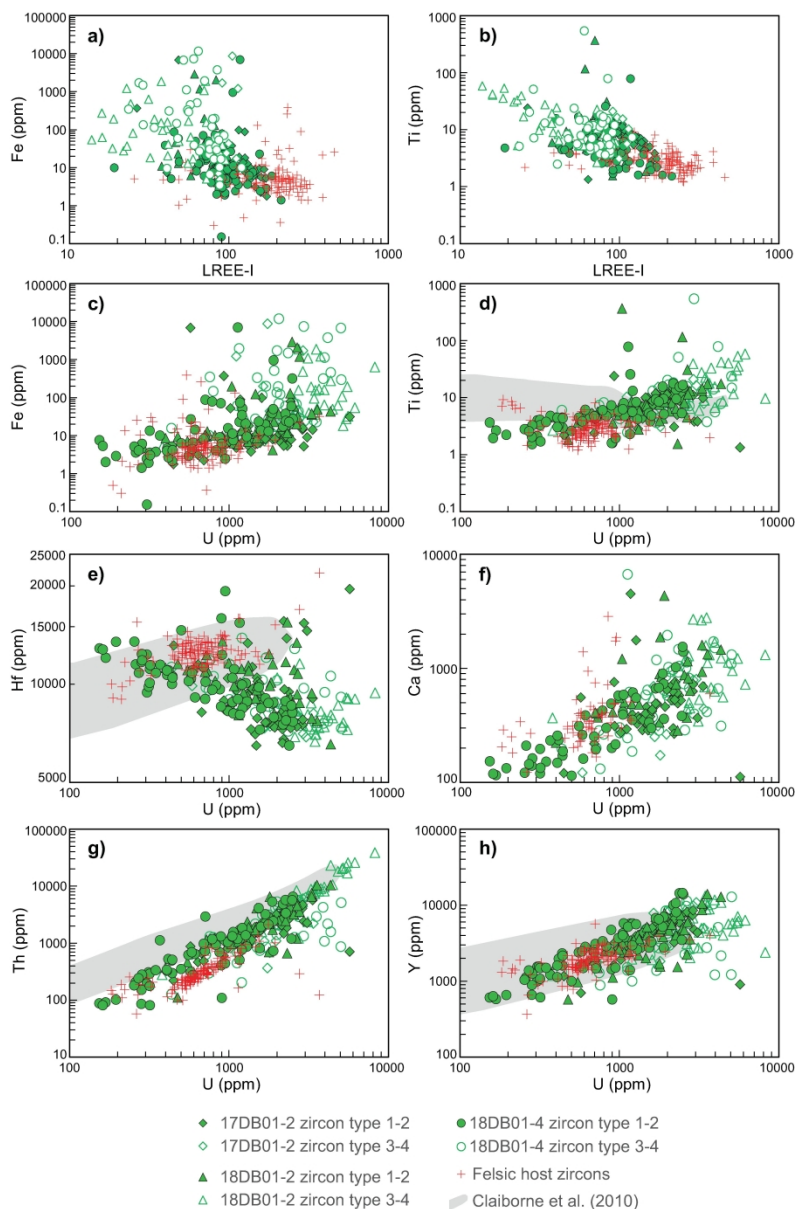


Fig. 8. Zircon trace element versus the Light Rare Earth Element Index [ $LREE-I = (Dy/Nd + Dy/Sm)$ ] (a proxy for zircon alteration Bell et al., 2016) and U content. Diorite zircon analyses are divided into two groups based on CL: types 1-2 clean grey sections of grains and types 3-4 regions dominated by metamictization and CL quenching; see Supplementary Data Electronic Appendix 2). There is considerable overlap between the two groups but types 3-4 have systematically lower LREE-1 and higher contents of all trace elements. In (a) and (b) Fe and Ti define negative trends with LREE-1 (in these figures, types 3-4 symbols were placed in front of types 1-2 for better visualization of the link between zircons deemed altered and LREE-1 values). Types 3-4 zircon analyses concentrate, as expected, in the lower end of LREE-1, indicative of alteration, but reach values of 100, considerably higher than the cutoff value of 30 for alteration of Bell et al. (2016). Up to 100, types 3-4 overlap with types 1-2, and these can have very high contents of Ti. In (c) to (h), Fe, Ca, Th, Y reach values close to 10,000 ppm or 1 wt.%, defining positive trends with U, which reaches up to 9000 ppm. Titanium also defines a positive trend with U, with numerous analyses above 30 ppm, some reaching a few 100 ppm. The trend defined by Hf and Ti in diorite zircons are the opposite to those found for granitic rocks by Claiborne et al. (2010) shown by the grey fields, and

similar to the high-U zircons in Fig. 6 in Troch et al. (2018). In (c) to (h), types 3-4 zircon symbols were placed behind types 1-2. For tonalite zircons, the trends are similar to those in Claiborne et al. (2010). Tonalite zircons and xenocrysts in diorite sample 18DB01-4 are not differentiated and overlap in the plots. All plots are log-log scale.

172x263mm (600 x 600 DPI)



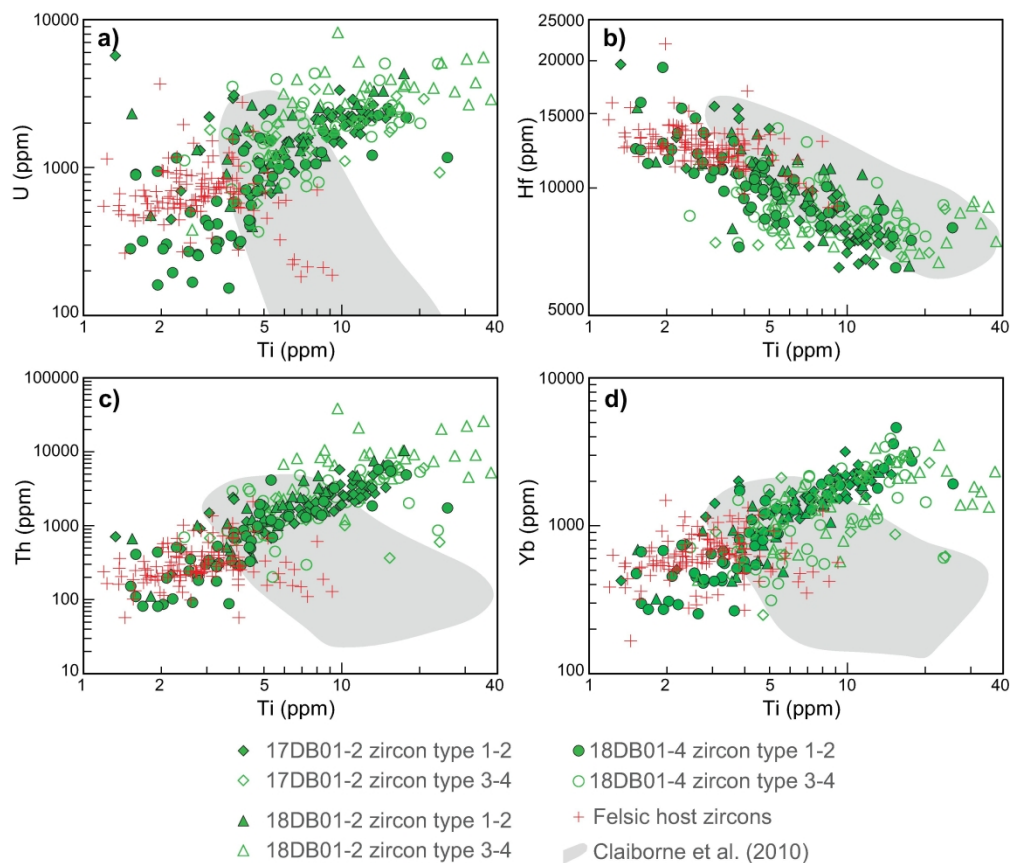


Fig. 9. (a-d) Binary plots of typically incompatible elements versus Ti in zircon. For tonalite samples Hf behaves incompatibly defining negative, but all other elements define a curved shape changing from a positive (compatible) to a negative (incompatible) trend as Ti increases. This is not the case for the diorite sample for which U, Th, and Yb, define only positive or compatible trends with Ti, and only Hf defines a negative (incompatible) trend. The compatible trends are surprising and contrast with the incompatible trends found by Claiborne et al (2010) indicated by grey fields. Ti-values higher than 40 ppm were not plotted as they correspond to unrealistically high T and therefore probably correspond to altered zircons. Grey empty symbols indicate analyses with anomalous peaks or plateaus of Fe and Ca, key indicators of metamictization and zircon re-equilibration (see section 9.2 for discussion). All plots are log-log scale and symbols are as in legend for Fig. 8.

169x144mm (600 x 600 DPI)



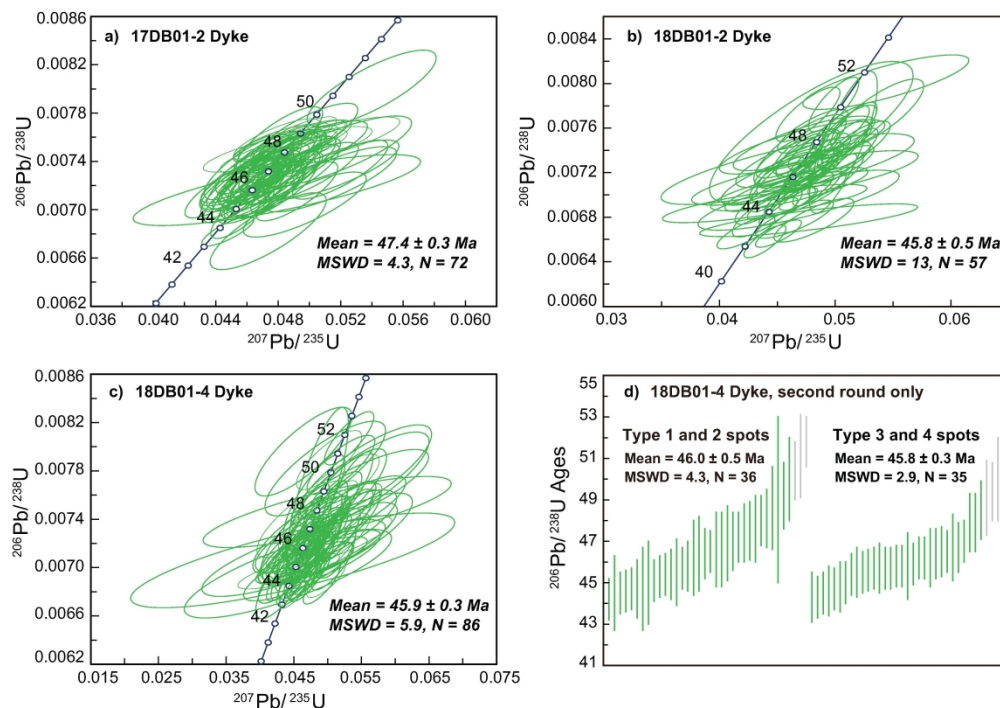


Fig. 10. Concordia diagrams for zircon analyses from diorite samples. a-c) Diorite dyke samples 17DB01-2, 18DB01-2 and 18DB01-4 with ages centred around 46 to 47 Ma. Samples 18DB01-2 and 18DB01-4 also contained 70-80 Ma xenocrysts shown in Fig. 11. d) Comparison between ages of zircon analyses from diorite sample 18DB01-4 as a function of CL type shows no systematic shift between CL types 1-2, and the quenched CL types 3-4 despite the anomalously high values of Th+U and other trace elements in the latter (Fig. 8). All ellipses in (a-c) and bars in (d) mark the  $2\sigma$  confidence level. A number of analyses have been excluded: 2 of 74 analyses for 17DB01-2 (1 with large error, 1 with fluctuating age signals), 18 out of 75 for 18DB01-2 (16 discordant and 2 outliers), 25 out of 111 for 18DB01-4 (23 discordant, 1 outlier and 1 with large error). A small number of outlier dates were removed from the calculation of the mean age by Isoplot: 2 out of 72 for sample 17DB01-2, 2 out of 57 for sample 18DB01-2, 4 out of 86 for sample 18DB01-4. In (d), analyses in light grey at the high-end of values, have been dates removed from the calculation of the mean age.

172x123mm (600 x 600 DPI)

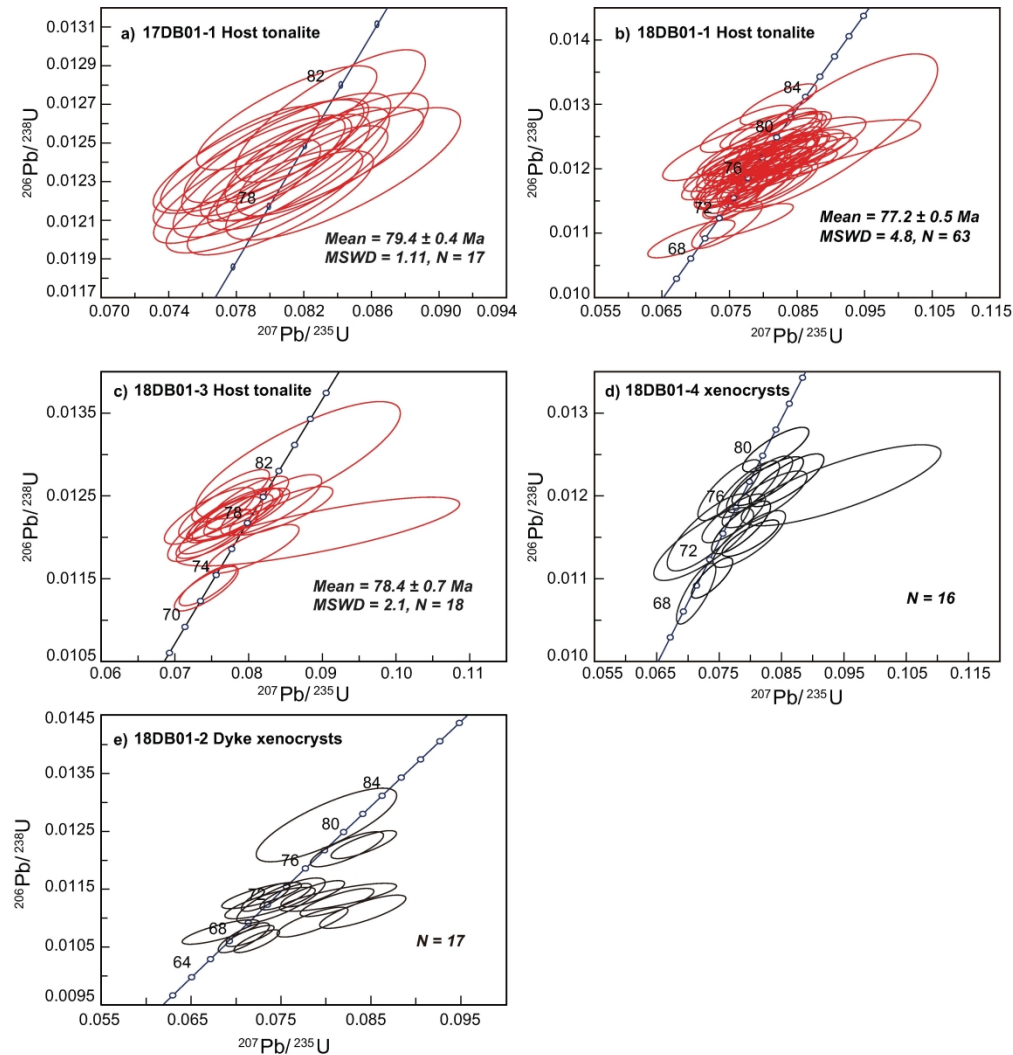


Fig. 11. Concordia diagrams for zircon analyses from tonalite samples and xenocrysts in diorite samples. a-c) Tonalite samples 17DB01-1, 18DB01-1, 18DB01-3 showing ages centred between 77 and 79 Ma and lacking older xenocrysts. d) and e) Xenocrysts from diorite dyke sample 18DB01-4 and 18DB01-2. The spread of dates in (d) and (e) imply that the mean ages are not meaningful with  $MSWD > 10$ . All ellipses mark the  $2\sigma$  confidence level. A small number of analyses have been excluded from the diagrams: 1 of 18 analyses for sample 17DB01-1 ( $>10\%$  discordant), 5 of 68 for 18DB01-1 (2 discordant and 3 outlier), and 3 of 19 for 18DB01-4 (2 with very large errors and 1 outlier). A small number of outliers were removed from the calculation of the mean age by Isoplot: 4 out of 63 for sample 18DB01-1, and 2 out of 18 for sample 18DB01-3.

172x181mm (600 x 600 DPI)

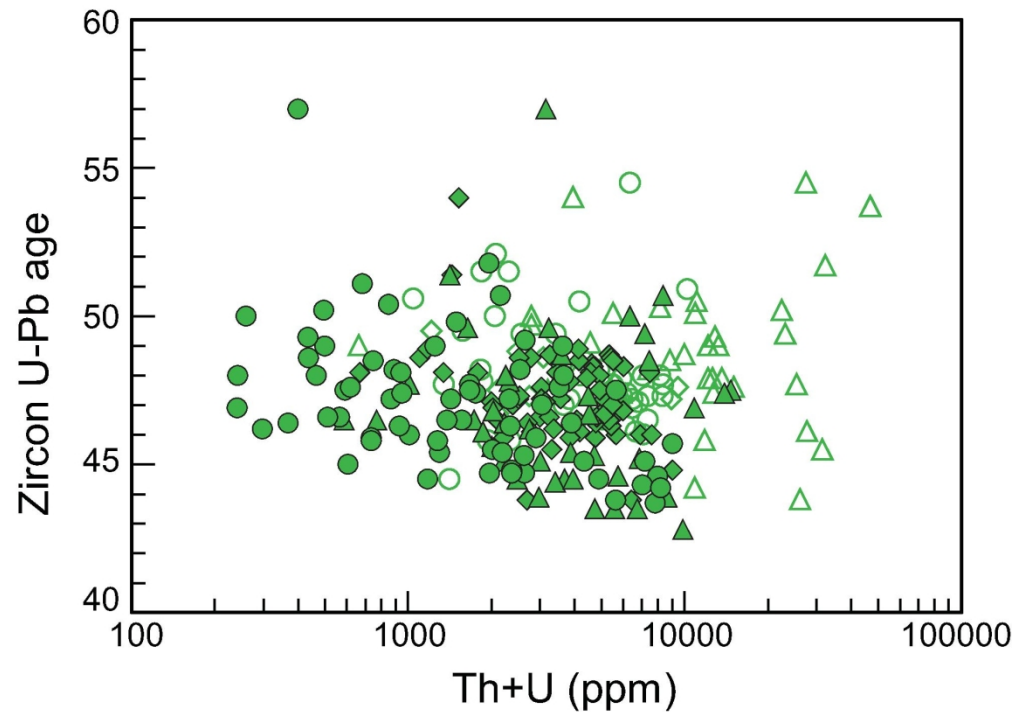


Fig. 12.  $^{206}\text{Pb}/^{238}\text{U}$  ages for zircons from diorites show no systematic trend with Th+U content. Symbols as in legend for Fig. 8 where empty symbols are types 3-4.

84x59mm (600 x 600 DPI)

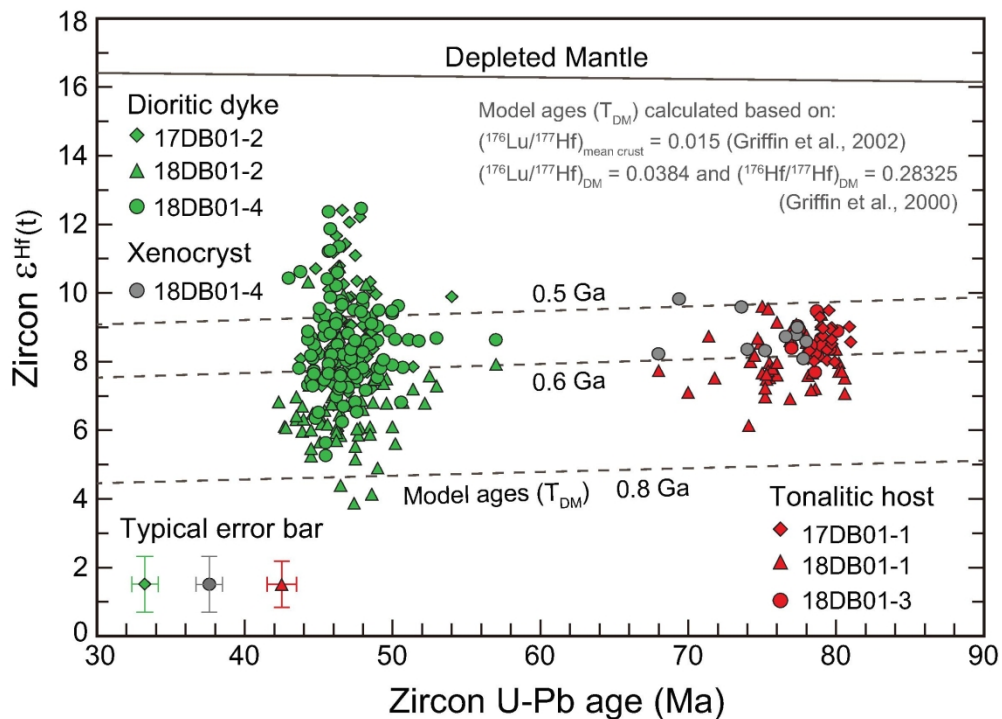


Fig. 13.  $\epsilon_{\text{Hf}}(t)$  values for all six samples plotted against zircon U-Pb age. The ~77-79 Ma tonalite zircons have  $\epsilon_{\text{Hf}}(t)$  centred around  $+9 \pm 1$ , whereas the ~46-47 Ma diorite analyses are more spread between  $+6$  and  $+11$ .  $N=344$  analyses, with 78 from tonalite zircons and 266 from diorite.

100x72mm (600 x 600 DPI)

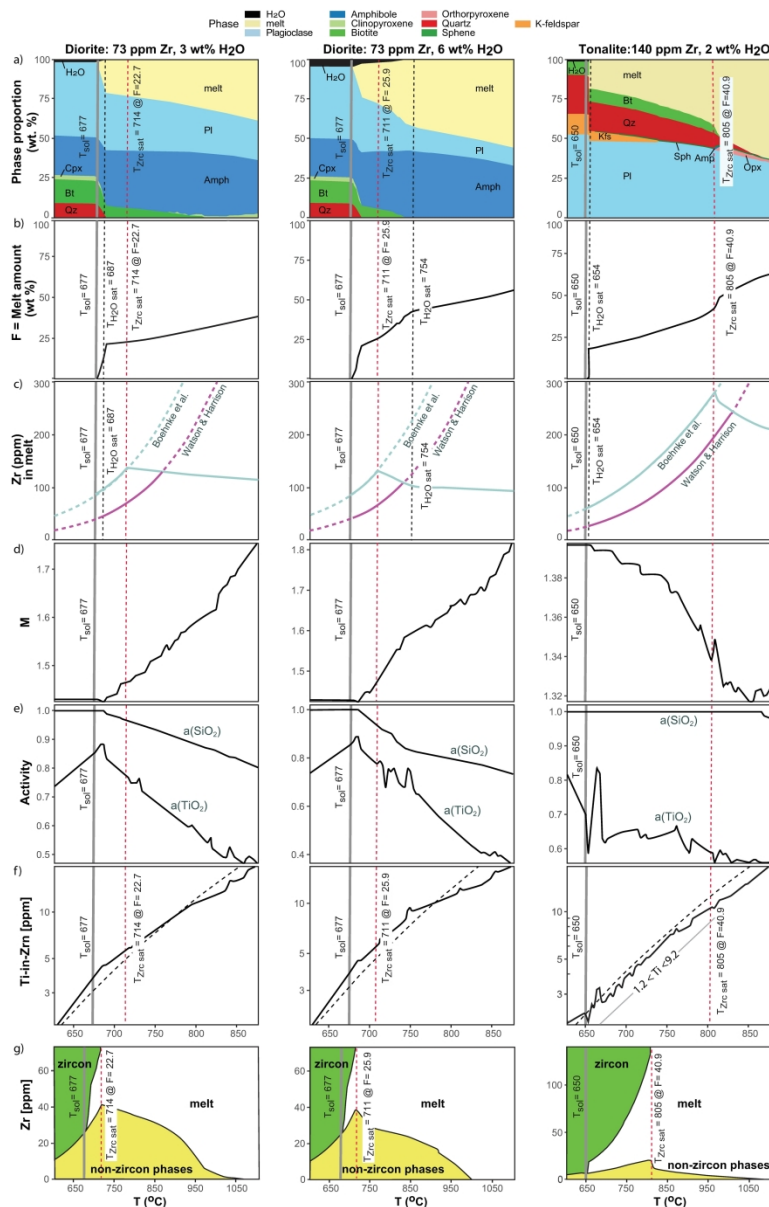


Fig. 14. Model of crystallization for a diorite melt with 73 ppm Zr and a tonalite melt with 144 ppm Zr. H<sub>2</sub>O contents for the diorite of 3 wt.% H<sub>2</sub>O (left column), and 6 wt.% H<sub>2</sub>O (middle column) are shown. Tonalite melt contains 2 wt.% H<sub>2</sub>O. Low H<sub>2</sub>O content was assumed in order to investigate its remelting by H<sub>2</sub>O derived from the diorite intrusion. a) Minerals and melt/H<sub>2</sub>O proportions. Diorite solidus T (T<sub>sol</sub>) is 677 oC, and 650 oC for the tonalite. The two diorite models show nearly 70 oC difference water saturation T. Sphene, spinel and ilmenite form in diorite and tonalite not shown because of low proportions. b) Melt fraction. For all three cases the last ~20% crystallizes within 10 oC of the solidus. c) Zr content in melt. Values increase until the curve intersects the zircon saturation curves calculated using M-values in (d) and calibrations in Boehnke et al. (2013) and Watson and Harrison (1983). Zircon saturation for the diorites is reached at 714 and 711 oC, for 3 and 6 wt.% H<sub>2</sub>O, respectively, where ~23% melt (for 3% H<sub>2</sub>O) or ~ 26% melt (for 6% H<sub>2</sub>O) remain. Tonalite reaches ~ 20% melt at ~650 oC solidus, where ~ 90% of the zircons are stable. d) M-value of residual melt used to determine the zircon saturation curve in (c). M-value for diorites steadily decrease to reach a value of 1.4 close to the solidus. For the tonalite M first decreases from a value of 1.45 at the liquidus (not shown) and then increases to ~1.4 at the solidus, due to stabilization of

Bt and Qtz. e)  $a(\text{SiO}_2)$  and  $a(\text{TiO}_2)$ . f) Ti-in-zircon calculated using curves in (e) (solid lines) or assuming a fixed value of  $a(\text{SiO}_2)=1$  and  $a(\text{TiO}_2)=0.7$  (dashed lines; similar to Claiborne et al. (2010)). The differences between the two curves are small. Calculations use Ferry and Watson (2007). g) Zr content in melt, non-zircon phases and zircon as a function of temperature (note different scale in x-axis). Zircons are saturated close to the solidus for diorite. Diorite composition is similar to the basalt modelled by Lee and Bachmann (2014) (their Fig. 2b), but despite higher Zr in our starting composition, melt never reaches the  $> 300$  ppm Zr in their model, peaking instead at  $\sim 150$  ppm, due to significant intake of Zr in non-zircon minerals excluded in their model.

277x436mm (300 x 300 DPI)

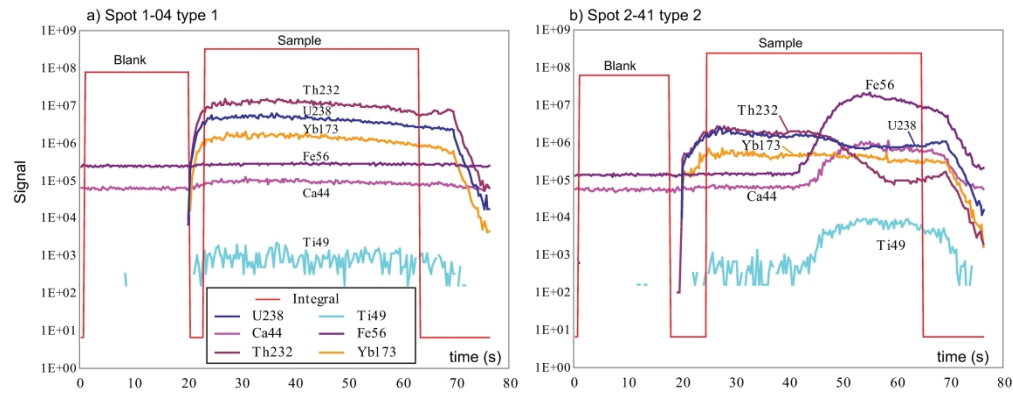


Fig. 15. Comparison of signal outputs from zircon analyses for sample 18DB01-4: a) spot 1-04 in a type 1 zircon, and b) spot 2-41 in a type 2 zircon. Data from (b) was excluded from consideration because of anomalous plateaus of Fe, Ca, Ti, and a sudden drop in Th, U counts.

274x105mm (600 x 600 DPI)

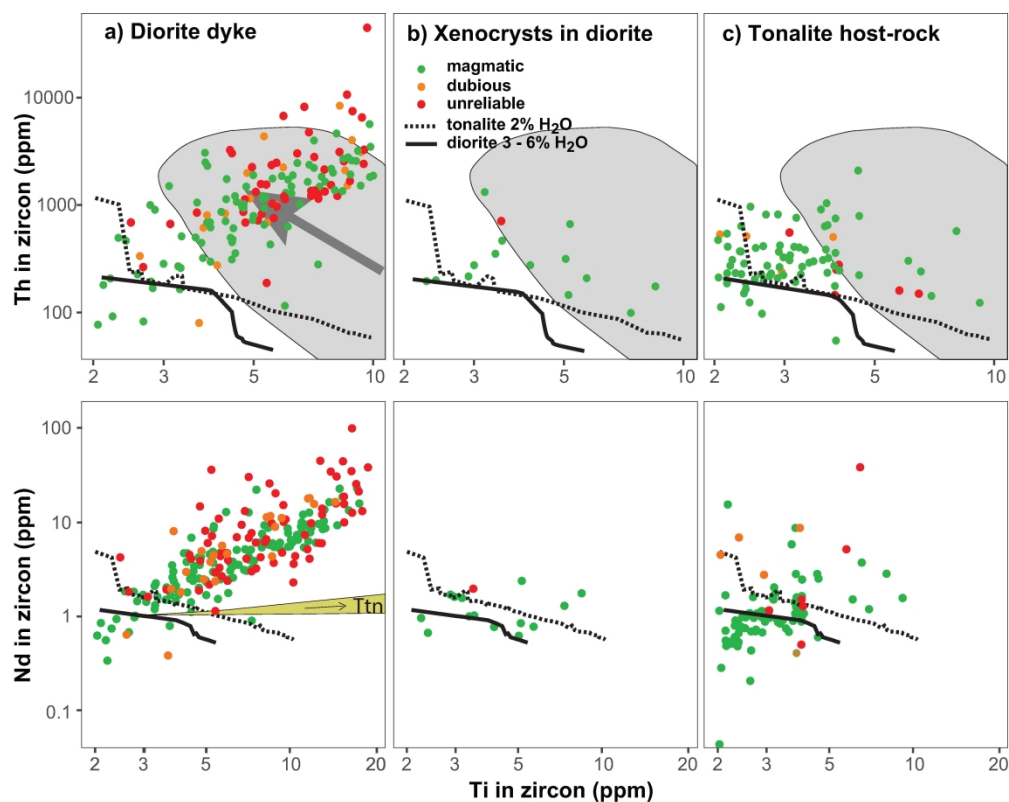


Fig. 16. Zircon chemistry modelling. a) Modelled zircon Th vs Ti composition for the diorite and tonalite (thick black lines) compared with data for zircons from diorite dykes, xenocrystic zircons in diorite and tonalite host rock zircons; b) same for Nd vs Ti. Analysed zircon grains are colour coded according to “reliability”: if the zircon analysis has anomalous Fe or Ca signal it is deemed unreliable, if it has anomalous peaks or plateaus of Y, Th, Ti or HREE it is deemed dubious, otherwise it is classified as magmatic. Models are calculated as discussed in the text and uses Boehnke et al.’s (2013) model for saturation, but the results are very similar using Watson & Harrison (1983). For comparison (a) shows the approximate slope of the trend (thick grey arrow) defined by the data for granitic rocks in Claiborne et al. (2006), which is similar to the modelled slope for the tonalite (thick dashed line). The yellow band in (b) defines the field generated by mixing a zircon composition with 3 ppm Ti and 1 ppm Nd, with titanite with 24.4 % Ti and between 1000 and 10000 ppm Nd (Bruand et al., 2020). The band indicates that mixing with titanite is unlikely to explain the trend because it causes a stronger enrichment in Ti compared to Nd.

190x151mm (600 x 600 DPI)



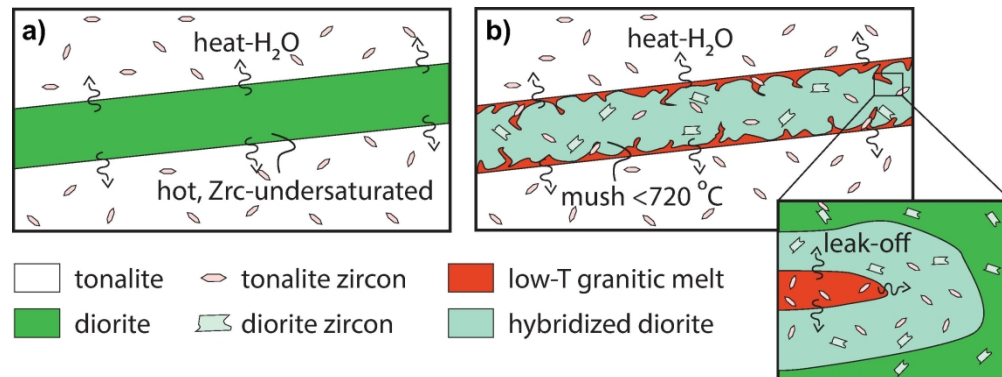


Fig. 17. Assimilation of host rock through anatexis, back-veining and mixing with zircon transfer. a) Original dioritic magma intrusion at temperatures above zircon saturation. As magma flows and cools, it heats-up the surrounding and releases H<sub>2</sub>O. b) The tonalite melts at relatively low temperatures lacking anhydrous peritectic minerals. Granitic dykelets derived from tonalite anatexis back-veins the diorite that is now a cool zircon-saturated mush. The mush deforms in a ductile fashion and granitic melt flow through the pore space of the mush (inset) transferring tonalite zircons and hybridizing the diorite. Zircon xenocrysts are preserved in the zircon-saturated diorite. Size of zircons is exaggerated.

126x47mm (600 x 600 DPI)